INVESTIGATION OF PHOTOCHEMISTRY AT HIGH LATITUDES: COMPARISON OF MODEL PREDICTIONS TO MEASUREMENTS OF SHORT LIVED SPECIES

A Thesis
Presented to
The Academic Faculty

by

Steven Jeffrey Sjostedt

In Partial Fulfillment
of the Requirements for the Degree
Doctor of Philosophy in the
School of Earth and Atmospheric Sciences

Georgia Institute of Technology
December 2006

INVESTIGATION OF PHOTOCHEMISTRY AT HIGH LATITUDES: COMPARISON OF MODEL PREDICTIONS TO MEASUREMENTS OF SHORT LIVED SPECIES

Approved by:

Dr. Greg Huey, Advisor
School of Earth and Atmospheric Science
Georgia Institute of Technology

Dr. Robert Whetten
School of Chemistry and Biochemistry
Georgia Institute of Technology

Dr. Paul Wine
School of Chemistry and Biochemistry
Georgia Institute of Technology

Dr. Rodney Weber
School of Earth and Atmospheric Science
Georgia Institute of Technology

Dr. David Tan
School of Earth and Atmospheric Science
Georgia Institute of Technology

Date Approved: September 26, 2006

ACKNOWLEDGEMENTS

I would like thank my advisor, Greg Huey, for his time, guidance, and provocative comments. His knowledge of atmospheric chemistry and instrumentation has proven to be valuable resources that were readily available to me. Early on I realized that I was working for the right advisor and over the last five years I have come to consider him a mentor and a friend.

I am grateful for the assistance that I have received from the other members of the CIMS group during my time here at Georgia Tech. In particular I am indebted to David Tanner who has freely shared the wealth of information about the CIMS that he has accrued over the years. Both in the lab and in the field Dave has patiently explained the finer points of instrument operation and data acquisition. I will miss working with him. I would also like to thank the members of the CIMS research group during my time here at Georgia Tech. In particular I would like to thank Robert Stickel, Saewung Kim, Jeff Peischl, Oscar Vargas, and Darlene Slusher for their assistance and input.

I owe a debt of gratitude to Gao Chen for his insights into photochemical processes. Gao also provided a sounding board for the development of the 0-D steady state model as well as a point of reference for the results.

Many thanks go out to my committee members, Paul Wine, Rodney Weber, Dave Tan, and Rob Whetten, for their comments which have strengthened this thesis. I would also like to thank my collaborators in the field, Jack Dibb, Barry Lefer, Manuel Hutterli, whose data was instrumental in the analysis of the measurements obtained in the field. I would also like to thank my classmates who have provided insight and support during my

time here at Georgia Tech. Finally, I would like to thank my family for their support over the last five years as I pursued my degree.

TABLE OF CONTENTS

LIST OF TABLES

LIST OF FIGURES

SUMMARY

Recent field campaigns have measured enhanced levels of NO_x ($NO+NO_2$) and HO_x precursors (i.e., H_2O_2, CH_2O, and HONO) that can not be accounted for by gas phase chemistry alone. Snowpack emission is now considered a source of these species. Therefore, the photochemistry in the polar boundary layer is now believed to be much more complex than initially thought.

Field campaigns to Summit, Greenland in the summer of 2003 and the spring of 2004 have obtained the first measurements of peroxy (HO_2+RO_2) and hydroxyl (OH) radicals in the Artic boundary layer. Measurements were collected with a chemical ionization mass spectrometer (CIMS). Median noon time observed concentrations for HO_2+RO_2 ranged from $4.1x10^8$ molecules cm^{-3} (summer) to $6.0x10^7$ molecules cm^{-3} (early spring). Median noon time observed concentrations for OH ranged from $8.4x10^6$ molecules cm^{-3} (summer) to $4.1x10^5$ molecules cm^{-3} (early spring).

A highly constrained (ie., O_3, H_2O, CH_4, CO, *j*-values, NO, H_2O_2,CH_2O, and HONO) 0-D steady-state model was employed in order to test current understanding of photochemistry. Peroxy measurements were in excellent agreement with model predictions for both spring and summer. Hydroxyl measurements were in good agreement with spring model predictions but were a factor of two greater than summer model predictions. The possible role of halogens is explored. The role of snowpack emission is also addressed in a HO_x budget performed on the spring campaign.

Measurements of nitric acid (HNO_3) and pernitric acid (HO_2NO_2) were obtained with the CIMS during the Antarctic Tropospheric Chemistry Investigation (ANTCI).

Median values for HNO_3 and HO_2NO_2 were 74 pptv (mean = 90 pptv) and 41 pptv (mean = 40 pptv) respectively. The linkage between HO_x and NO_x chemistry is examined through partitioning of reactive nitrogen between HNO_3 and HO_2NO_2. The possible impact of reactive nitrogen partitioning on nitrate ions (NO_3^-) at coring sites is also investigated.

CHAPTER 1

INTRODUCTION

1.1 Motivation and Overview

Photochemistry is at the core of many atmospheric processes. Oxidation of biogenic and anthropogenic emissions [*Prinn,* 2003*; Thompson,* 1992*; Chameides and Davis,* 1982], formation of new aerosols [*Korhonen et al.,* 1999*; Weber et al.,* 1995*; Lushinikov and Sutugin,* 1976] and growth of existing aerosols [*Kulmala et al.,* 2004*; Ansari and Pandis,* 1999*; Seinfeld and Ramabhadran,* 1975] are all dependent on photochemistry. HO_x ($HO_x = OH + HO_2$) chemistry [*Chameides and Davis,* 1982] and NO_x ($NO_x = NO + NO_2$) [*Crutzen et al.,* 1978] chemistry both play pivotal roles within photochemical processes. The advent of highly sensitive instrumentation with fast time responses has allowed scientists to test their understanding of photochemical processes [*Heard and Pilling,* 2003*;Ryerson et al.,* 2000*; Eisele and Bradshaw,* 1993*; Fehsenfeld et al.,* 1987] Often the data obtained have provided as many new questions as answers.

Until recently the HO_x chemistry of the polar boundary layer has remained largely unexplored. Conventional wisdom dictated that there would be little activity in the high latitudes due to their remote location, low dew points, and limited solar radiation. However, investigations of other phenomena such as artic haze [*Shaw and Wendler,* 1972] and ozone depletion [*Barrie et al.,* 1988] also provided data that suggested that the photochemistry of high latitudes was more active and complex than initially thought.

Polar regions have also come under closer scrutiny as climate change has come into the public consciousness. Ice core records that hold the paleoclimate record have

been obtained in this environment [*Hammer et al.,* 1997*; Mayewski and Bender,* 1995]. An understanding of the chemical processes in the atmosphere and the air-ice interactions are necessary for a thorough interpretation of past atmospheric composition. High latitudes are also expected to be the region most affected by changes in the current climate [*Stoll,* 2006*; Walsh,* 1991].

This thesis focuses on the role that HO_x and NO_x chemistry plays in the polar boundary layer. The introductory chapter presents an overview of the chemical processes that are occurring at high latitudes and a brief outline of the field campaigns that have sought to measure and interpret those processes. Also a summary of the data is presented and the main topics addressed by this thesis are outlined.

1.2 Chemistry of the polar boundary layer

Initially the chemistry of the polar boundary layer was expected to be fairly inactive. Low dew points coupled with high solar zenith angles (reduced insolation) were expected to diminish oxidizing capacity at high latitudes. This original assumption had to be reevaluated when larger than expected concentrations of NO_x and HO_x precursors (i.e., nitrous acid, formaldehyde, and hydrogen peroxide) were observed.

1.2.1 HO_x Chemistry

By the early 1970s the scientific community had recognized that the hydroxyl radical (OH) held a pivotal role in the atmosphere [*Levy,* 1971]. The rate at which many of the trace gases were oxidized and subsequently removed were dependent on the concentration of OH. The hydroxyl radical is often referred to as the "scrubber" of the

atmosphere. Primary production of OH is initiated by photolysis of ozone by UV light ($\lambda < 340$ nm) that produces electronically excited atomic oxygen atom $O(^1D)$ which can react with water to initiate a radical chain.

1. $O_3 + h\nu \rightarrow O(^1D) + O_2$

2. $O(^1D) + H_2O \rightarrow 2OH$

The hydroxyl radical will then react with most of the reduced species in the atmosphere in an efficient manner. In many cases reaction with OH determines how long a chemical species remains in the atmosphere, or more succinctly it determines that species lifetime. Analogously the lifetime of OH (τ_{OH}) is extremely short ~1 second, due to the reactive nature of the hydroxyl radical, and is dependent on the concentrations of other trace gases. In the remote troposphere oxidation of carbon monoxide plays the most significant role in determining the lifetime of OH.

3. $OH + CO + M \rightarrow HOCO + M$

3a. $HOCO + O_2 \rightarrow HO_2 + CO_2$

3.1 $OH + CO + M \rightarrow H + CO_2 + M$

3.1a $H + O_2 \rightarrow HO_2$

Since CO_2 is fully oxidized it will not react with OH. Although reaction 3 consumes the hydroxyl radical, reaction 3a produces hydroperoxy radical (HO_2). HO_2 is a less reactive reservoir of OH, and collectively the two are referred to as HO_x. Therefore, the largest loss term for OH is considered a null cycle for the HO_x, HO_2 can react with other species such as nitric oxide (see below) and ozone to regenerate the hydroxyl radical. In an environment devoid of odd nitrogen species ozone can cycle both HO_x species thus propagating the radical chain.

4. $HO_2 + O_3 \rightarrow OH + 2O_2$

5. $OH + O_3 \rightarrow HO_2 + O_2$

Reactions 4 and 5 also result in a net loss of two ozone molecules. This cycle will continue until the radicals react with themselves to terminate the chain.

6. $HO_2 + HO_2 \rightarrow H_2O_2 + O_2$

7. $OH + HO_2 \rightarrow H_2O + O_2$

8. $OH + OH \rightarrow H_2O_2$

1.2.2 NO_x chemistry

The reactive nitrogen species nitric oxide (NO) and nitrogen dioxide (NO_2), collectively known as NO_x, are intimately connected with the HO_x family. The presence of NO can change a remote environment from one of ozone destruction (Reactions 4-5) to an environment of ozone production.

9. $HO_2 + NO \rightarrow OH + NO_2$

10. $NO_2 + h\nu \rightarrow NO + O(^3P)$

11. $O(^3P) + O_2 \rightarrow O_3$

Reaction 9 also increases the oxidizing capacity of the atmosphere by cycling HO_2 to OH [*Eisele et al.,* 1997*: Hack et al.,* 1980].

The presence of NO_x also provides two more termination steps for the HO_x cycle by the formation of nitric acid (HNO_3) and pernitric acid (HNO_4). OH can also react with NO to form nitrous acid (HONO). However, HONO has an extremely short photolytic lifetime (~10 min) and is considered a reservoir rather than a sink.

12 $OH + NO_2 + M \rightarrow HNO_3 + M$

13 $HO_2 + NO_2 + M \rightarrow HO_2NO_2 + M$

14. $OH + NO + M \rightarrow HONO + M$

Nitric acid can photolyze to regenerate OH, but this process is very slow. OH can also react with HNO_3 to provide a sink for HO_x; however, the rate for this reaction is of a similar timescale as photolysis. The lifetime of HNO_3 with respect to reactions 15 and 16 is a week or more. Deposition of HNO_3 to a surface is often orders of magnitude faster and will determine the lifetime of HNO_3 in polar environments. In the polar boundary layer formation of nitric acid is regarded as a sink for HO_x and NO_x.

15. $HNO_3 + h\nu \rightarrow OH + NO_2$

16. $OH + HNO_3 \rightarrow H_2O + NO_3$

17. HNO_3(Deposition) $\rightarrow$ Removal

By comparison pernitric acid has a photolytic lifetime of approximately one day. The lifetime of HO_2NO_2 with respect to oxidation (Reaction 20) by the hydroxyl radical is of similar magnitude to the pernitric lifetime due to photolysis (Reactions 18-19). Photolysis will regenerate HO_x and NO_x while oxidation will result in a HO_x loss.

18. $HO_2NO_2 + h\nu \rightarrow HO_2 + NO_2$

19. $HO_2NO_2 + h\nu \rightarrow OH + NO_3$

20. $OH + HO_2NO_2 \rightarrow NO_2 + O_2 + H_2O$

However, the lifetime of HNO_4 is highly dependent on temperature as it can thermally decompose (reaction 21). The photolytic and oxidative lifetime is overwhelmed by thermal decomposition at warmer temperatures.

21. $HO_2NO_2 + M \rightarrow HO_2 + NO_2 + M$

When the temperature drops to ~245K the rate of thermal decomposition (Reaction 21) becomes similar in magnitude to photolytic and oxidative losses (Reactions 18-20). In the lower temperature regime encountered in the polar boundary layer, deposition of pernitric acid may become a loss for both HO_x and NO_x.

22. HNO_4(Deposition) → Removal

Not only are formation of nitric acid and deposition of pernitric acid HO_x losses but they also determine the lifetime of NO_x (τ_{NOx}) at high latitudes.

$$\tau_{NO_x} = \frac{\frac{[NO]}{[NO_2]} + 1}{k_{12}[OH] + k_{13}[HO_2]\left(\frac{k_{22}}{j_{18} + j_{19} + k_{20}[OH] + k_{21} + k_{22}}\right)}$$

Regardless of the temperature regime, oxidation of pernitric acid by OH (Reaction 20) is also a HO_x loss. The magnitude of this loss term is also highly dependent on temperature.

1.2.3 Methane Oxidation

Methane is ubiquitous through the global troposphere since the lifetime of methane is approximately 8-10 years [*Watson et al.*, 1992]. Oxidation of methane can influence HO_x concentrations in the remote polar boundary layer. Oxidation of methane (Reaction 23) and one of its end products, carbon monoxide (Reaction 3), are the two largest loss terms for OH in this environment. Oxidation of methane will also generate HO_x radicals through reactions of intermediate products such as the methyl peroxy radical (CH_3O_2), formaldehyde (CH_2O), and methyl hydrogen peroxide (CH_3OOH).

Methane oxidation can be a net source or sink. This is dependent on the NO_x concentration.

23. $OH + CH_4 \rightarrow CH_3 + H_2O$

23a. $CH_3 + O_2 \rightarrow CH_3O_2$

24. $CH_3O_2 + NO \rightarrow CH_3O + NO_2$

24a. $CH_3O + O_2 \rightarrow CH_2O + HO_2$

25. $CH_3O_2 + HO_2 \rightarrow CH_3OOH + O_2$

26. $CH_3O_2 + CH_3O_2 \rightarrow 2CH_3O + O_2$

26a. $2(CH_3O + O_2) \rightarrow 2HO_2 + 2CH_2O$

27. $CH_3O_2 + CH_3O_2 \rightarrow CH_2O + CH_3OH + O_2$

28. $CH_3OOH + h\nu \rightarrow CH_3O + OH$

29. $OH + CH_3OOH \rightarrow CH_3O_2 + H_2O$

30. $OH + CH_3OOH \rightarrow OH + CH_2O + H_2O$

Whether methane oxidation is a HO_x source or sink is determined by the difference between the production terms $P(HO_x)_{methane}$ and the loss terms $L(HO_x)_{methane}$.

$$P(HO_x)_{methane} = k_{24}[CH_3O_2][NO] + 2k_{26}[CH_3O_2]^2 + 2j_{28}[CH_3OOH]$$
$$L(HO_x)_{methane} = k_{23}[OH][CH_4] + k_{25}[CH_3O_2][HO_2] + k_{29}[CH_3OOH][OH]$$

If NO_x concentrations are high then reaction 24 will dominate, and the oxidation of methane will generate formaldehyde and conserve both HO_x and NO_x. Methane oxidation will be a net HO_x source. As NO_x concentrations diminish the branching ratio begins to favor reaction 25, and methyl hydrogen peroxide (CH_3OOH) is formed. In this low NO_x scenario the oxidation of methane becomes a net HO_x sink. However, it should be noted that at the lowest NO_x levels the self reactions of the methyl peroxy radical

(Reactions 26-27) and photolysis of methyl hydrogen peroxide will still generate HO_x radicals.

1.2.4 HO_x precursors

The preceding reactions demonstrate that formaldehyde is generated from methane oxidation. Hydrogen peroxide and nitrous acid are also generated by self reactions of HO_x radicals (Reactions 6 and 8) and the reaction of OH with NO (Reaction 14). In the natural system these species are considered reservoirs. The photolysis or oxidation of each must be considered.

In the case of formaldehyde the largest photolysis rate (Reaction 31) does not create HO_x. However, the slower of the two photolysis rates (Reactions 32-a-b) is a HO_x source generating two HO_2 radicals. Oxidation of formaldehyde (Reaction 33) also does not impact the total HO_x concentration. It simply converts OH to HO_2.

31. $CH_2O + h\nu \rightarrow H_2 + CO$

32. $CH_2O + h\nu \rightarrow H + HCO$

32a. $H + O_2 \rightarrow HO_2$

32b. $HCO + O_2 \rightarrow HO_2 + CO$

33. $OH + CH_2O \rightarrow HCO + H_2O$

Hydrogen peroxide and nitrous acid also undergo similar photolysis and oxidation reactions. Photolysis of hydrogen peroxide leads to the production of two OH radicals. Oxidation of hydrogen peroxide cycles OH back to HO_2.

34. $H_2O_2 + h\nu \rightarrow 2OH$

35. $OH + H_2O_2 \rightarrow HO_2 + H_2O$

Nitrous acid concentrations are expected to be very low as it absorbs light in the visible region. Therefore HONO photolyzes quite rapidly ($j_{HONO} \approx 1x10^{-3}$ s^{-1}) and will regenerate both OH and NO. HONO can also be oxidized by the hydroxyl radical, but the rate is not particularly fast. Therefore, oxidation of nitrous acid is not expected to significantly impact the HO_x budget.

36. $HONO + h\nu \rightarrow OH + NO$

37. $OH + HONO \rightarrow H_2O + NO_2$

All three of the HO_x precursor species have been measured during previous high latitude field campaigns (see below). The concentrations of each have been observed at values that were higher, sometimes orders of magnitude higher, than originally predicted. It is these observations of HO_x precursors that have helped to spur interest in HO_x chemistry in this environment.

1.3 Field Campaigns

1.3.1 HO_x field campaigns in remote locations

Although the importance of the hydroxyl radical to photochemistry had been determined in the early 1970s it took another two decades for suitable HO_x measurement techniques to come on line (see Chapter 2). Since 1991 various field campaigns have been organized to measure the oxidizing capacity of the atmosphere in a variety of environments [*Bloss et al.,* 2003*; George et al.,* 1999*; Holland et al.,* 1998]. The most remote campaigns such as the Mauna Loa Photochemistry Experiment (MLOPEX-2), and the Pacific Exploratory Missions (PEM Tropics A and PEM Tropics B) focused on regions influenced by tropical marine air [*Tanner and Eisele,* 1995; *Eisele et al.,* 1996;

Mauldin et al., 1999; *Chen et al.,* 2001; *Olsen et al.,* 2001; *Mauldin et al.,* 2001; *Eisele et al.,* 2001; *Wang et al.,* 2001]. Maritime locations were chosen for two reasons. First they were far from anthropogenic and biogenic sources located on the continents. For example, average NO levels for PEM Tropics A and PEM Tropics B were 3 pptv and 1 pptv respectively [*Bradshaw et al.,* 1999:2000]. Second, they were in regions of high primary production due to abundant water vapor and low solar zenith angles (Reactions 1-2). During the PEM-Tropics B campaign boundary layer (<2km) OH and HO_2 mean concentrations ranged from 3-6x10^6 molecules cm^{-3} and 3-5x10^8 molecules cm^{-3} respectively [*Tan et al.,* 2001].

The chemistry in the remote boundary layer was expected to be relatively uncomplicated and thus a good place to check measurements with model predictions. Modeled (M) to observed (O) ratios for OH (M/O = 0.86) and HO_2 (M/O = 1.12) were in excellent agreement and photolysis of ozone (Reactions 1-2) was recognized as a major source of HO_x in the boundary layer [*Tan et al.,* 2001]. The dominant HO_x sinks in the marine environment were radical self reactions (Reactions 6-7) and formation of peroxides with other non-HO_2 peroxy radicals (Reactions 25 and 38). Peroxy radicals are defined as HO_2 +RO_2 where RO_2 = CH_3O_2, $C_2H_5O_2$, $CH_3(CO)O_2$, etc.

38. $RO_2 + HO_2 \rightarrow ROOH + O_2$

High latitude sites were also removed from anthropogenic sources; however, they were not as thoroughly investigated for HO_x since the oxidizing capacity was expected to be diminished. One notable exception was the Sulfur Chemistry in the Antarctic Troposphere Experiment (SCATE) mission at Palmer station on the Antarctic Peninsula. Since the focus of the campaign was sulfur chemistry, the suite of HO_x precursor

measurements was limited. There were no measurements of HONO, H_2O_2, or CH_2O to constrain model predictions. However, there were measurements of O_3, water vapor and NO. As was the case with other remote sites, NO was quite low (1-5 pptv) at Palmer Station [*Jefferson et al.,* 1998]. The measured OH number densities (mean = $1x10^5$ molecules cm^{-3}) were indeed much lower than the values observed in the tropics [*Jefferson et al.,* 1998]. Photolysis of ozone was again calculated to be the dominant source, and oxidation of carbon monoxide (Reaction 3) and methane (Reaction 23) were determined to be responsible for the majority of OH loss. There were no HO_2 observations during SCATE to calculate a full HO_x budget.

Field campaigns have explored HO_x chemistry in the upper troposphere and lower stratosphere. Measurements of HO_x and many precursors during STRAT (Stratospheric Tracers for Atmospheric Transport), SUCCESS (Subsonic Aircraft: Contrail and Cloud Effects Spectral Study), and SONEX (Subsonic Assesment: Ozone and Nitrogen Oxide Experiment) provide values in an environment that is similar to those found in high latitudes [*Wennberg et al.,* 1998; *Brune et al.,* 1998*;*1999]. Although these campaigns were often flown over continental land masses concentrations of most chemical species were lower than in the continental boundary layer. Temperatures encountered at higher altitudes (220K-250K) were more representative of those found at high latitudes.

Budget analysis of all three campaigns indicated photolysis of ozone was unable to explain the observed HO_x concentrations (*Jaegle et al.,* 2001). Therefore enhanced production from elevated acetone found at high altitudes and peroxides brought up from convection were added to the photochemical model to determine the HO_x production rate, $P(HO_x)$. Jaegle suggests that the variance of observed HO_x can be determined by HO_x

production rate and NO_x concentration. The photochemical model is divided into three regimes based on NO_x mixing ratios. In the NO_x limited regime (NO_x <100pptv) self reactions of HO_x radicals (Reactions 6-8) and reactions with other peroxy radicals (Reaction 38) are the major loss pathways. Reaction of OH with pernitric acid (Reaction 20) also became significant in this regime as NO_x concentrations increased. In the transition regime (100 pptv < NO_x < 300 pptv) OH + HNO_4 was the dominant HO_x loss term with formation of nitric acid (Reaction 12) assuming a larger role as NO_x increased. At the highest NO_x mixing ratios, the NO_x saturation regime, formation of nitric acid became the dominant HO_x loss term. The attenuation of HNO_4 production and increase in HNO_3 is a function of conversion of HO_2 to OH by high NO mixing ratios (Reaction 9). However, at the highest NO_x levels the observed HO_x concentrations still were much higher (up to a factor of 5) than model predictions [*Faloona et al.,* 2000]. Furthermore, there were no measurements of pernitric acid available to confirm this hypothesis.

1.3.2 High latitude field campaigns

During the mid 1980s tropospheric photochemistry in high latitudes was generating interest for reasons other than HO_x chemistry. Ozone depletion events (ODE) observed in the Canadian high arctic were attributed to concomitant increases in bromine oxide during the spring [*Platt and Honninger,* 2003; *Honninger and Platt,* 2002; *Impey et al.,* 1999; *Barrie and Platt,* 1997; *Impey et al.,* 1995; *Hausmann and Platt,* 1995; *Barrie et al.,* 1988].

39. $Br_2 + h\nu \rightarrow 2Br$

40. $Br + O_3 \rightarrow BrO + O_2$

41. $BrO + BrO \rightarrow Br_2 + O_2$

Cycling of HO_2 to OH by BrO also plays a significant role in determining the oxidizing capacity of the polar boundary layer.

42. $HO_2 + BrO \rightarrow HOBr + O_2$

43. $HOBr + h\nu \rightarrow OH + Br$

However, this has only been recently investigated and was not considered during the early campaigns.

There were other indications from early arctic missions that HO_x chemistry might be more complex than originally suggested. In 1992 the Polar Sunrise Experiment at Alert, Nunavut, Canada included reactive nitrogen in the suite of measured species. Among the findings was an inordinately large amount of nitrous acid (HONO = 5-70 pptv) in the polar troposphere [*Li*, 1994]. Gas phase photochemistry could not explain the amount of HONO observed, and it was hypothesized that emission from the snowpack was the source of the HONO enhancement. This implied that OH levels would be much higher than expected due to photolysis of HONO.

Figure 1.1 Map of Alert, Nunavut, Canada

Interest in photochemistry was also increasing at other arctic locations. The paleoclimate records from the Greenland ice core project (GRIP) and the Greenland ice sheet project (GISP) were obtained during the early 1990s at Summit, Greenland [*Dibb et al.,* 1997]. In order to interpret the emerging records an understanding of the chemical processes that occurred from Air-Snow transfer was required. A small campaign to measure stable isotpes was initiated at Summit camp in Greenland in 1989 [*Dibb*, 1990]. The subsequent campaign in 1993 at Summit introduced gas phase measurements of H_2O_2, CH_2O and O_3 [*Bales et al.,* 1995]. By the end of the drilling period in 1994, the suite of measurements at Summit was expanded to include HNO_3 [*Dibb et al.,* 1998, *Munger et al.,* 1999].

Figure 1.2 Map of Summit, Greenland

1.3.3 Measurements of NO_x and HONO

Early measurements of nitrous acid, formaldehyde and hydrogen peroxide suggested that the oxidizing capacity of the high latitude troposphere might be much higher than primary production of ozone would suggest. However, it was a series of

elevated NO_x measurements that were instrumental in generating the current interest in photochemistry at high latitudes. The primary sources of NO_x are anthropogenic, automobiles in particular, and lightning, both of which are in short supply at high latitudes. Furthermore, the lifetime of NO_x is ~1 day so transport of NO_x from mid latitude sources was expected to be negligible. During the Polar Sunrise Experiment at Alert *Ridley et al.* [2000] observed elevated levels of NO_x (10-50 pptv) suggesting the presence of an unaccounted for source. Although Alert is a coastal site, like Palmer, it was surrounded by ice for the entire measurement period. This led to speculation that snowpack maybe the significant source of NO_x. NO_x measurements were repeated at Summit later that year by *Honrath et al.* [1999] and similarly enhanced levels were found on the Greenland ice cap. Finally, in the austral summer of 1998 the highest NO mixing ratios (median=225ppt) found at high latitudes were observed during the ISCAT field campaign at the South Pole [*Davis et al.*, 2001].

Figure 1.3 Map of Antarctica

To test the hypothesis that the snowpack was a NO_x source a series of experiments were conducted in the field and the laboratory. Snow samples from Summit [*Honrath et al.,* 2000a], the Upper Peninsula of Michigan [*Honrath et al.,* 2000b] and Antarctica [*Jones et al.,* 2001] demonstrated that exposure to sunlight led to production of NO_x. It had already been established that photolysis of nitrate ions in aqueous solution produces NO and NO_2 radicals [*Mack and Bolton*, 1999]. By extension it was suggested that nitrate ions found in the quasi-liquid layer that forms on the snow surface were the source of the ambient NO_x enhancement. *Dubowski et al.,* [2001] investigated this process by irradiating spray-frozen aqueous nitrate solutions with 302 nm light. The irradiation of nitrate ions in solution not only produced NO_x but also nitrous acid. Therefore photolysis of nitrate in the quasi-liquid layer is now believed to contribute to the HONO enhancement [*Zhou et al.,* 2003] observed at high latitudes. Experiments with a snowpile illuminated by a Xe arc lamp demonstrated that gas phase HONO concentrations did indeed increase with irradiation [*Beine et al.,* 2002a].

As a result the investigation of HONO intensified at high latitudes in later campaigns. In the summer of 2000 at Summit both ambient and interstitial HONO [*Dibb et al.,* 2002] were measured. Midday ambient concentration were often 10 pptv or higher and concentrations within the firn would reach over 100 pptv. A positive flux of HONO of 4.6×10^{11} molecules m^{-2} s^{-1} out of the snowpack was also measured during this campaign [*Honrath et al.,* 2002]. A diurnal profile in the observations provides further evidence that HONO is produced by illumination of the snowpack. HONO measurements were also collected during the Alert2000 campaign. Measured HONO values ranged from 4-10 pptv depending on the time of day (highest values occurred around local

noon). HONO measurements were also obtained at the South Pole during the ISCAT 2000 field campaign. Much like the previous NO_x measurements during the ISCAT 1998 field mission HONO levels were the highest observed (mean = 30 pptv) at a high latitude site.

1.3.4 Measurements of Peroxides and Oxygenated Carbon Species

The first measurements of peroxides were obtained at Summit during 1990 where hydrogen peroxide reached levels as high as 3.5 ppbv [*Sigg et al.,* 1992]. Starting in 1996 hydrogen peroxide has an almost continuous record of measurement at Summit [*Anklin and Bales,* 1997; *Hutterli et al.,* 2001; *Jacobi et al.,* 2002]. Mean concentrations ranged from 0.78 to 1.8 ppbv during these campaigns. Gas phase photochemistry alone could not explain the concentrations observed at Summit. *Hutterli et al.,* [2001] suggest that the snowpack could be either a source or a sink for H_2O_2. The flux of H_2O_2 out of (or into) the snowpack was dependent on temperature. A positive net flux of $5x10^{13}$ molecules m^{-2} s^{-1} was calculated for 12 days during the 1996 Summit field mission.

By comparison measurements of hydrogen peroxide at Alert are limited. The only peroxide values in the literature for Alert were obtained during the Polar Sunrise Experiment in 1992 [*de Serves*, 1994]. These initial measurements did not speciate between H_2O_2 and organic peroxides but rather measured the sum. During the dark period total peroxide concentration averaged 40 pptv. Peroxide concentrations ranged between 100-400 pptv in the later sunlit period of the experiment.

The measurement record is not as long in Antarctica, but a recent suite of measurements now provides enhanced spatial and temporal coverage over the continent.

Starting in the 1997/8 overwintering season hydrogen peroxides were obtained at the Neumayer station in Queen Maude Land on the Antarctic coast. The median value for the polar night was 0.054 ppbv and increased to 0.200 ppbv during the sunlit season [*Riedel et al.,* 2000]. The ISCAT 2000 mean H_2O_2 concentration collected at the Amundsen-Scott station was 0.278 ppbv [*Hutterli et al.,* 2004]. The measurements for the ISCAT field campaign were collected during the month of December. A three-year record of hydrogen peroxide measurements between the two sites, collected during the austral summers, was also obtained during the US International Trans-Antarctic Scientific Expedition. Median concentrations over the expedition were 0.321 ppbv in 2000, 0.650 ppbv in 2001, and 0.330 ppbv in 2002 [*Frey et al.,* 2005]. Measurements of methyl hydrogen peroxide (MHP) were brought on line for the last two years of the campaign. Median concentrations of MHP were 0.317 ppbv in 2001 and 0.304 ppbv in 2002 [*Frey et al.,* 2005].

Formaldehyde measurements have also played a prominent role in the recent high latitude field campaigns. In 1996 *Hutterli et al.* [1999] observed median formaldehyde concentrations of 230 pptv at Summit. Later, back to back Summit campaigns displayed significant interannual variability where the 1999 campaign had a mean mixing ratio of 74 pptv and the 2000 campaign had a mean mixing ratio of 120 pptv. As with HONO and H_2O_2 gas phase photochemistry was unable account for all of the measured CH_2O at Summit. Therefore, an average flux of $8x10^{11}$ molecules m^{-2} s^{-1} from the snowpack was calculated during the 2000 field campaign to account for difference [*Jacobi et al.,* 2002].

Formaldehyde was initially measured at Alert during the Polar Sunrise Experiment 1992 campaign and its concentration ranged between 30-600 pptv during the

sunlit period [*de Serves*, 1992]. Later at Alert the listed range of CH_2O was from 53-690 ppt during the 1998 campaign and was strongly anticorrelated with ozone [*Sumner et al.,* 2002]. The measurement was repeated during the Alert 2000 where two other oxygenated carbon species, acetaldehyde and acetone, were measured along with CH_2O. The average formaldehyde, acetaldehyde, and acetone concentrations for the 2000 campaign were 166 pptv, 53 pptv, and 385 pptv respectively [*Grannas et al.,* 2002]. All three oxygenated carbon species can be considered photolytic sources for HO_x production.

44. $CH_3CHO + h\nu \rightarrow CH_3 + HCO$

45. $CH_3(CO)CH_3 + h\nu \rightarrow CH_3(CO) + CH_3$

45a. $CH_3(CO) + O_2 \rightarrow CH_3(CO)O_2$

46. $CH_3(CO)O_2 + NO_2 \rightarrow CH_3(CO)OONO_2$

47. $CH_3(CO)O_2 + NO \rightarrow CH_3 + CO_2 + NO_2$

48. $CH_3(CO)O_2 + HO_2 \rightarrow CH_3(CO)OOH + O_2$

Acetaldehyde and acetone were also indicators of halogen chemistry [*Grannas et al.,* 2002]. Modeling of this data will be addressed later in this chapter.

Formaldehyde measurements in Antarctica display a large range between interior and coastal sites. During the ISCAT 2000 campaign the mean CH_2O concentration was 103 pptv at the South Pole [*Hutterli et al.,* 2004] in good agreement with arctic sites. By comparison seasonal measurements at Neumayer display the highest averaged mixing ratios at a high latitude site. For the 1997-8 campaign at Neumayer the polar night mean value was 150 pptv, and during the summer the mean concentration was 360 pptv [*Riedel et al.,* 1999]. For the months of October and November the mean mixing ratios of CH_2O

are 456 pptv and 479 pptv. To accommodate such elevated concentrations a flux of $2x10^{13}$ molecules m^{-2} s^{-1} was calculated to come from the snowpack [*Riedel et al.,* 2005].

1.3.5 Hydroxyl and Peroxy Radical Measurements

Direct measurements of OH and peroxy radicals have been limited in high latitudes. The TOPSE airborne campaign measured both species over series of seven deployments covering the Canadian Arctic. The majority of the OH data were below $3x10^{6}$molecules/cm^{3}; however, it should be noted that the reported data were obtained at higher altitudes [*Mauldin et al.,* 2003]. The measurement of peroxy radicals offers greater spatial coverage. The measurements were binned into low and high latitude categories where 60N was the dividing line. At altitudes below 3km the peroxy number densities were 1-1.5x10^{8}molecules/cm^{3} for the flight leg 5 in early April [*Cantrell et al.,* 2003]. The peroxy number density increased to 2-3x10^{8}molecules/cm^{3} during the last deployment (flight 7) in mid May. Even with this extended coverage the lowest measurements (in altitude) of peroxy radicals were taken at 0.5 km. Thus the measurements were above the polar boundary layer and removed from snow sources.

OH was also measured during the ISCAT 1998 and ISCAT 2000 field missions. The observed midday OH number densities ranged between 2-4x10^{6} molecules cm^{-3} during ISCAT 1998 mission. A mean concentration of 2.5x10^{6} molecules cm^{-3} was observed during the ISCAT 2000 mission. From a very limited data set a median peroxy number density of 7x10^{7}molecules/cm^{3} was observed for the ANTCI 2003 field campaign.

Table 1.1 Summary of field campaigns at Summit, Greenland

2000			
Species	Technique	Concentration	Reference
NO	Chemiluminescence	16.0 pptv (mean)	*Yang et al.*, 2002
NO_2	Chemiluminescence	15.2 pptv(mean)	*Yang et al.*, 2002
HONO	Mist Chamber/Ion Chromatograph	12.7 pptv	*Yang et al.*, 2002
HNO_3	Mist Chamber/Ion Chromatograph	0-100 pptv	*Honrath et al.*, 2002
H_2O_2	Fluorescence Spectroscopy	720 pptv (mean)	*Yang et al.*, 2002
CH_2O	Fluorescence Spectroscopy	120 pptv (mean)	*Yang et al.*, 2002
O_3	Ultraviolet Absorbance	51.3 ppbv (mean)	*Yang et al.*, 2002
CO	Gas Chromatography/ Flame Ionization	110 ppbv (mean)	*Yang et al.*, 2002
CH_4	Gas Chromatography/ Flame Ionization	1.8 ppmv (mean)	*Yang et al.*, 2002
1999			
NO	Chemiluminescence	24.7 pptv (mean)	*Yang et al.*, 2002
NO_2	Chemiluminescence	32.7 pptv(mean)	*Yang et al.*, 2002
HONO	Mist Chamber/Ion Chromatograph	7.2 pptv	*Yang et al.*, 2002
HNO_3	Mist Chamber/Ion Chromatograph	0-100 pptv	*Honrath et al.*, 2002
H_2O_2	Fluorescence Spectroscopy	1780 pptv (mean)	*Yang et al.*, 2002
CH_2O	Fluorescence Spectroscopy	74 pptv (mean)	*Yang et al.*, 2002
O_3	Ultraviolet Absorbance	40.5 ppbv (mean)	*Yang et al.*, 2002
CO	Gas Chromatography/ Flame Ionization	90 ppbv (mean)	*Yang et al.*, 2002
CH_4	Gas Chromatography/ Flame Ionization	1.8 ppmv (mean)	*Yang et al.*, 2002
Early Campaigns (1990-1998)			
NO_x	Chemiluminescence	1998 = 0-30 pptv	*Honrath et al.* 1999
H_2O_2	Fluorescence Spectroscopy	1996 =0.2-4.5 ppbv	*Hutterli et al.*, 2001
CH_2O	Fluorescence Spectroscopy	1996 = 230 pptv (mean)	*Hutterli et al.*, 1999
HNO_3	Mist Chamber-Ion Chromatograph	1995 = 0-7 nmol/m^3	*Dibb et al.*, 1998
H_2O_2	Fluorescence Spectroscopy	1993 = 0.1-2.5 ppbv	*Bales et al.*, 1995
H_2O_2	Fluorescence Spectroscopy	1990 = 0.3-3.5 ppbv	*Sigg et al.*, 1992

Table 1.2 Summary of field campaigns at Alert, Nunavut, Canada

ALERT2000			
Species	Technique	Concentration	Reference
NO	Chemiluminescence	4.0 pptv (mean)	*Beine et al.*, 2002
NO_2	Chemiluminescence	10.6 pptv (mean)	*Beine et al.*, 2002
HONO	High Performance Liquid Chromatography	0-30 pptv	*Zhou et al.*, 2001
CH_2O	Fluorometric Analyzer	35-370 pptv	*Sumner et al.*, 2002
CH_3CHO	Gas Chromatography/Mass Spectrometry/Flame	26-552 pptv	*Boudries et al.*, 2002
$CH_3(CO)CH_3$	Ionization	18-1470 pptv	
O_3	Ultraviolet Absorbance	0-45 ppbv	*Bottenheim et al.*, 2002
BrO	Differential Optical Absorbance Spectroscopy	0-30 pptv	*Honninger and Platt*, 2002
Br_2	Chemical Ionization	2-27 pptv	*Spicer et al.*, 2002
BrCl	Mass Spectrometry	2-35 pptv	
Solar Radiation	Spectral Radiometer		*Simpson et al.*, 2002
CO	GC/MS/FID	180-200 ppbv	*Sumner et al.*, 2002
CH_4	GC/MS/FID	1.8 ppmv (mean)	*Sumner et al.*, 2002
NMHC	GC/MS/FID		*Bottenheim et al.*, 2002
Polar Sunrise Experiment 1998			
NO	Chemiluminescence	0-20 pptv	*Ridley et al.*, 2000
NO_2	Chemiluminescence	0=30 pptv	*Ridley et al.*, 2000
CH_2O	Fluorometric Analyzer	52-690 pptv	*Sumner and Shepson*, 1999
O_3	Ultraviolet Absorbance	0-51 ppbv	*Sumner and Shepson.*, 1999
Br	Gas Chromatography/	$1.4x10^7$molec cm^{-3}	*Boudries et al.*,
Cl	Mass Spectrometry	$7.5x10^4$molec cm^{-3}	2000
Early Campaigns (1990-1998)			
BrO_x	Photoactive Halogen	1997 = 4-15 pptv	*Impey et al.* 1999
HOBr	Detector/GC	1997 = 25-260 pptv	
HONO	Denuder/ Ion Chromatograph	1992 = 0-65 ppbv	*Li*, 1994
NMHC	GC/FID		*Jobson et al.*, 1999
BrO	Differential Optical Absorbance Spectroscopy	1992 = 4-17 pptv	*Hausmann and Platt*, 1994
H_2O_2+ROOH	Fluorometric Analyzer	1992 = 40-400 pptv	*deServes*, 1994
CH_2O	Fluorometric Analyzer	1992 = 30-700 pptv	*deServes*, 1994
O_3	Ultraviolet Absorbance	1992 = 0-45 ppbv	*Anlauf et al.*, 1994

Table 1.3 Summary of field campaigns in Antarctica

Species	Technique	Concentration	Reference
ISCAT 2000 (South Pole)			
OH	Chemical Ionization	$2.5e^6$ molec cm^{-3}(mean)	*Mauldin et al.*, 2004
HO_2+RO_2	Mass Spectrometer	$7.0e^7$ molec cm^{-3}(mean)	
NO	Chemiluminescence	85 pptv (median)	*Davis et al.*, 2004
HONO	Mist Chamber/Ion	33 pptv (median)	*Dibb et al.*, 2004
HNO_3	Chromatograph	35 pptv (median)	
HNO_3	Chemical Ionization	22 pptv (mean)	*Huey et al.*, 2004
HNO_4	Mass Spectrometer	25 pptv (mean)	*Slusher et al.*, 2002
H_2O_2	Fluorescence Spectroscopy	278 pptv (mean)	*Hutterli et al.*, 2004
CH_2O	Fluorescence Spectroscopy	103 pptv (mean)	*Hutterli et al.*, 2002
Solar Radiation	Scanning Actinic Flux Spectroradiometer		*Lefer* unpublished results
O_3	Ultraviolet Absorbance	20-40 ppbv	CMDL
CO	Gas Chromatography	38 ppbv (mean)	CMDL
CH_4	Gas Chromatography	1.7 ppmv (mean)	CMDL
ISCAT 1998 (South Pole)			
OH	CIMS	$2.0e^6$ molec cm^{-3}(mean)	*Mauldin et al.*, 2001
NO	Chemiluminescence	225 pptv (median)	*Davis et al.*, 2001
Solar Radiation	Scanning Actinic Flux Spectroradiometer		*Lefer et al.*, 2001
O_3	Ultraviolet Absorbance	18-40 ppbv	*Crawford et al.*, 2001
CO	Gas Chromatography	40 ppbv (mean)	CMDL
CH_4	Gas Chromatography/	1.7 ppmv (mean)	CMDL
International Trans Antarctic Scientific Expedition (2000-2002)			
CH_3OOH	Fluorescence Spectroscopy	2001 = 317 pptv (mean) 2002 = 304 pptv (mean)	*Frey et al.*, 2005
H_2O_2	Fluorescence Spectroscopy	2000 = 321 pptv (mean) 2001 = 650 pptv (mean) 2003 = 330 pptv (mean)	*Frey et al.*, 2005
Other Campaigns (1994-1999) N- Neumayer P= Palmer			
CH_2O (N)	Fluorescence Spectroscopy	1999 = 98-479 pptv	*Riedel et al.*, 2005
CH_3OOH (N)	Fluorescence Spectroscopy	1999 = 62-233 pptv	*Riedel et al.*, 2005
H_2O_2 (N)	Fluorescence Spectroscopy	1999 = 35-298 pptv	*Riedel et al.*, 2005
NO (N)	Chemiluminescence	1999 = 1-7 pptv	*Weller et al.*, 2002
HNO_3 (N)	Chemiluminescence	1999 = 1-20 pptv	*Weller et al.*, 2002
NO (N)	Chemiluminescence	1997 = 3 pptv (mean)	*Jones et al.*, 1999
HNO_3 (N)	Chemiluminescence	1997 = 5 pptv (mean)	*Jones et al.*, 1999
OH (P)	CIMS	1994 = $1.1e^5$ molec cm^{-3} (mean)	*Jefferson et al.*, 1998
NO (P)	Chemiluminescence	1994 = 2-4 pptv	*Jefferson et al.*, 1998

1.4 Model Predictions and Budgets

In order to evaluate the chemistry controlling the oxidizing capacity of the polar boundary layer there have been several attempts to derive a HO_x budget at high latitude measurement sites. The predictions generally have been constrained to the data collected during their respective field campaigns. This has led to a wide range of predicted HO_x values and predicted sources and sinks.

1.4.1 Model Results from Polar Sunrise Experiment 1992

The earliest calculations by *Li et al.* [1994] predicted OH number densities of $3x10^5$molecules cm^{-3}. Production of OH is derived from photolysis of ozone, formaldehyde and nitrous acid. HONO measurements obtained during the Polar Sunrise Experiment in 1992 were among the highest recorded at Alert, up to 65 pptv, and were predicted to be the dominant OH source. Photolysis of HONO was predicted to be an order of magnitude larger than photolysis of formaldehyde and two orders of magnitude larger than photolysis of ozone. Even with the enormous nitrous acid source the predicted hydroxyl concentration was an order of magnitude lower than later observed concentrations during the TOPSE field campaign and at the South Pole. The fact that the cycling of peroxy radicals (Reactions 9 and 24-24a) was omitted from this model helps to explain the low OH predictions.

1.4.2 Model Results from ALERT 2000

A HO_x budget was derived for the ALERT 2000 campaign [*Grannas et al.*, 2002] using a series of 1-D time dependent models based on the chemical mechanism described

in *Michalowski et al.* (2000). The first model (model A) used a standard gas phase model constrained to measured values of HO_x precursors (*j*-values, O_3, H_2O, CH_2O), and calculated fluxes of NO and HONO from the snowpack. The fluxes were proportional to incoming solar radiation. The second model (model B) has reactions for bromine and chlorine in addition to the mechanism used in model A. The reasoning for this is two fold. First, it allows the model to replicate the ozone depletion events that are occasionally observed at Alert. Second, the presence of acetaldehyde (CH_3CHO) and acetone ($CH_3(CO)CH_3$) infers that halogens are reacting with volatile organic compounds (VOCs) to provide additional sources for peroxy and hydroxyl radicals.

49. $Cl + CH_3CH_2CH_3 \rightarrow CH_3CHCH_3 + HCl$

49a $CH_3CHCH_3 + 2O_2 \rightarrow HO_2 + CH_3(CO_2)CH_3$

50. $CH_3(CO_2)CH_3 + NO \rightarrow CH_3(CO)CH_3 + NO_2$

51. $Cl + CH_3CH_2CH_3 \rightarrow CH_3CH_2CH_2 + HCl$

51a. $CH_3CH_2CH_2 + O_2 \rightarrow CH_3CH_2CH_2O_2$

52. $CH_3CH_2CH_2O_2 + NO \rightarrow CH_3CH_2CH_2O + NO_2$

52a. $CH_3CH_2CH_2O + O_2 \rightarrow HO_2 + CH_3CH_2CHO$

53. $Br + CH_3CH_2CHO \rightarrow CH_3CH_2CO + HBr$

53a $CH_3CH_2CO + O_2 \rightarrow CH_3CH_2(CO)O_2$

54. $CH_3CH_2(CO)O_2 + NO \rightarrow CH_3CH_2 + CO_2 + NO_2$

54a. $CH_3CH_2 + O_2 \rightarrow CH_3CH_2O_2$

55. $CH_3CH_2O_2 + NO \rightarrow CH_3CH_2O + NO_2$

56. $CH_3CH_2O + O_2 \rightarrow HO_2 + CH_3CHO$

HO_x budgets were determined for both model A and model B. The production of HO_x was dominated by photolysis of HONO (64%) and CH_2O (25%) in model A. The remainder of HO_x production was attributed to photolysis of HOBr, ozone, and reaction of hydrocarbons with chlorine. In model B assumed concentrations for halogen radicals ([Br] = $1.5x10^7$molecules cm^{-3}, [Cl] = $7x10^4$molecules cm^{-3}), similar to the values calculated by *Boudries et al.* [2000], were included. The largest HO_x sources for model B were photolysis of HOBr (33%) and HONO (32%) followed by photolysis of CH_2O (19%) and Cl + hydrocarbons (13%). There were two other points of interest in the Grannas budget. Photolysis of hydrogen peroxide was not included in the HO_x budget and photolysis of O_3 is calculated to be responsible for <2% of OH production in both models.

1.4.3 Model predictions from Summit 1999 and 2000

The concentrations of both hydroxyl and peroxy radicals were modeled for the 1999 and 2000 Summit field campaigns by *Yang et al.* [2002]. The 0-D steady state model employed a 21 reaction mechanism that was constrained to measurements of a similar suite of HO_x precursors as *Grannas et al.* [2002]. However, there were several important differences worth noting between the models. First, the Yang model was constrained to measured values of hydrogen peroxide. Second, the Yang model was also constrained to measurements of HONO and NO rather than employing fluxes. Finally, halogen chemistry was not considered at Summit.

In order to calculate the peroxy radical calculations Yang employs a conversion ratio α where $\alpha = [HO_2]/[PO_2]$ and $[PO_2]$ = all peroxy radicals. Three mean noontime

concentrations are listed for $\alpha = 0.5$, $\alpha = 0.7$, $\alpha = 0.9$ for each field campaign. OH values are listed as number densities (molecules/cm^3), and peroxy values are listed in parts per trillion (ppt).

Table 1.4 Predicted median radical concentrations at Summit for 1999 and 2000

	1999			2000		
Species	$\alpha = 0.5$	$\alpha = 0.7$	$\alpha = 0.9$	$\alpha = 0.5$	$\alpha = 0.7$	$\alpha = 0.9$
OH	4.0×10^6	5.0×10^6	6.0×10^6	6.8×10^6	$8.4 s10^6$	9.9×10^6
HO_2	19	24	29	25	31	27
PO_2	38	34	32	50	44	41

Yang et al. [2002] concluded that HO_x production from precursors such as HONO, H_2O_2, and CH_2O would be of greater magnitude than primary production from ozone photolysis. In the summer 1999 field campaign they predicted that photolysis of formaldehyde would be a stronger HO_x source than photolysis of ozone. Yang also predicted that during the 2000 field campaign HONO and ozone photolysis sources of HO_x would be of similar magnitude. In both years photolysis of ozone is predicted to be responsible for less than 35% of the total HO_x budget.

1.4.4 Model Predictions for ISCAT 2000

Hydroxyl and peroxy radical concentrations were modeled as part of the ISCAT 2000 field campaign [*Chen et al.*, 2001, 2004]. The ISCAT 2000 modeling studies have the added benefit of measurements of both species to compare with model predictions. The time dependent model employs an explicit HO_x-NO_x-CH_4 mechanism with 71 reactions. The Chen model is constrained by pernitric acid and j-values in addition to the same suite of species as the Yang model. Furthermore, the peroxy radicals were directly calculated rather than determined by an assumed ratio. To compare model predictions

with measured data a series of three model runs were conducted. The first run was unconstrained by measurements of H_2O_2, CH_2O, and HONO; the second was constrained to H_2O_2 and CH_2O, and the third was constrained to all three. The best agreement, by far, with measured concentrations was achieved by the second run. Since the HONO measurement is non-specific for HONO, it measures nitrite ions (NO_2^-) in the aqueous phase, HONO was not considered in the budget calculations.

To determine the HO_x budget the snow sources of hydrogen peroxide and formaldehyde were included. The snow source was calculated from the difference from OH from the first run (standard model) and the second run which was constrained to observed values.

$$\Delta[OH]_{snow} \approx \left(\frac{\Delta[OH]}{\Delta[H_2O_2]}\right)\left([H_2O_2]_{obs} - [H_2O_2]_{std}\right)$$

$$\Delta[HO_2]_{snow} \approx \left(\frac{\Delta[HO_2]}{\Delta[H_2O_2]}\right)\left([H_2O_2]_{obs} - [H_2O_2]_{std}\right)$$

$$\Delta[OH]_{snow} \approx \left(\frac{\Delta[OH]}{\Delta[CH_2O]}\right)\left([CH_2O]_{obs} - [CH_2O]_{std}\right)$$

$$\Delta[HO_2]_{snwo} \approx \left(\frac{\Delta[HO_2]}{\Delta[CH_2O]}\right)\left([CH_2O]_{obs} - [CH_2O]_{std}\right)$$

From this analysis 46% of the HO_x budget was attributed to precursors coming from the snowpack (CH_2O = 32% and H_2O_2 = 14%) The remaining budget was split evenly between photolysis of ozone and oxidation of methane.

1.5 Summary

Recent field campaigns at high latitudes have demonstrated that HO_x chemistry is far more complex than initially thought. It is now known that emissions of NO_x and HO_x precursors from the snowpack influence the oxidizing potential in these environments. Although measurements of NO_x and HO_x precursors have been obtained over a wide spatial and temporal range in high latitudes, measurements of HO_x radicals are sparse. The TOPSE field campaign provided measurements of both HO_2 and OH in the Arctic; however, these measurements were obtained above the polar boundary layer. The data obtained were in an environment where snowpack emissions had little impact. Measurements of OH in the polar boundary layer have been collected at the Palmer and Amundsen-Scott stations in Antarctica. Measurements of HO_2 were non existent for SCATE and the ISCAT 1998 mission and were quite limited during the ISCAT 2000 field campaign. Pernitric acid has also been recognized as an important sink for both HO_x and NO_x chemistry in cold environments. Although pernitric acid has been invoked in HO_x budgets for high altitudes and latitudes measurements of HO_2NO_2 are limited to the ISCAT 2000 field campaign.

1.6 Foci of Thesis

In order to test our understanding of photochemistry in the polar boundary layer measurements of HO_x radicals were obtained at Summit Greenland during the summer of 2003 and the spring of 2004 with a Chemical Ionization Mass Spectrometer. By measuring HO_x in spring and summer the data covered a wide range of conditions (i.e incoming solar radiation, temperature, and meteorology) at a location where paleoclimate

records were obtained. The HO_x data will be compared to 0-D steady state photochemical model constrained to a full suite of HO_x precursors and NO_x. HO_x budgets will be derived to determine the impact of photochemistry and snowpack emissions on the oxidizing capacity at Summit. The possible role of halogen chemistry at Summit will also be explored.

The chemical linkage between NO_x and HO_x chemistry through formation of pernitric acid has been suggested in earlier high altitude field campaigns and confirmed by measurement during ISCAT 2000. The ANTCI 2003 field campaign at the Amundsen-Scott station provided another occasion to investigate the role of pernitric acid with respect to HO_x and NO_x chemistry. The South Pole is an optimal place for HO_2NO_2 measurements since it is located in an environment that is cold enough that thermal decomposition does not dominate the pernitric lifetime and experiences a wide range NO_x mixing ratios. The HO_2NO_2 obtained during ANTCI 2003 provides an opportunity to test our understanding of HO_x chemistry in a high NO_x environment without HO_2 measurements and a chance to determine the thermal decomposition rate of pernitric acid

1.7 References

Anklin, M., and R. C. Bales (1997), Recent increase in H2O2 concentration at Summit, Greenland, *Journal of Geophysical Research-Atmospheres*, *102*, 19099-19104.

Ansari, A. S., and S. N. Pandis (1999), Prediction of multicomponent inorganic atmospheric aerosol behavior, *Atmospheric Environment*, *33*, 745-757.

Bales, R. C., J. R. Mcconnell, M. V. Losleben, M. H. Conklin, K. Fuhrer, A. Neftel, J. E. Dibb, J. D. W. Kahl, and C. R. Stearns (1995), Diel Variations of H_2O_2 in Greenland - a Discussion of the Cause and Effect Relationship, *Journal of Geophysical Research-Atmospheres*, *100*, 18661-18668.

Barrie, L., and U. Platt (1997), Arctic tropospheric chemistry: an overview, *Tellus Series B-Chemical and Physical Meteorology*, *49*, 450-454.

Barrie, L. A., J. W. Bottenheim, R. C. Schnell, P. J. Crutzen, and R. A. Rasmussen (1988), Ozone Destruction and Photochemical-Reactions at Polar Sunrise in the Lower Arctic Atmosphere, *Nature*, *334*, 138-141.

Beine, H. J., F. Domine, W. Simpson, R. E. Honrath, R. Sparapani, X. L. Zhou, and M. King (2002a), Snow-pile and chamber experiments during the Polar Sunrise Experiment 'Alert 2000': exploration of nitrogen chemistry, *Atmospheric Environment*, *36*, 2707-2719.

Beine, H. J., R. E. Honrath, F. Domine, W. R. Simpson, and J. D. Fuentes (2002b), NO_x during background and ozone depletion periods at Alert: Fluxes above the snow surface, *Journal of Geophysical Research-Atmospheres*, *107*, -.

Bloss, W. J., T. J. Gravestock, D. E. Heard, T. Ingham, G. P. Johnson, and J. D. Lee (2003), Application of a compact all solid-state laser system to the in situ detection of atmospheric OH, HO_2, NO and IO by laser-induced fluorescence, *Journal of Environmental Monitoring*, *5*, 21-28.

Bradshaw, J., D. Davis, J. Crawford, G. Chen, R. Shetter, M. Muller, G. Gregory, G. Sachse, D. Blake, B. Heikes, H. Singh, J. Mastromarino, and S. Sandholm (1999), Photofragmentation two-photon laser-induced fluorescence detection of NO_2 and NO: Comparison of measurements with model results based on airborne observations during PEM-Tropics A, *Geophysical Research Letters*, *26*, 471-474.

Bradshaw, J., D. Davis, G. Grodzinsky, S. Smyth, R. Newell, S. Sandholm, and S. Liu (2000), Observed distributions of nitrogen oxides in the remote free troposphere from the NASA global tropospheric experiment programs, *Reviews of Geophysics*, *38*, 61-116.

Brune, W. H., I. C. Faloona, D. Tan, A. J. Weinheimer, T. Campos, B. A. Ridley, S. A. Vay, J. E. Collins, G. W. Sachse, L. Jaegle, and D. J. Jacob (1998), Airborne in-situ OH and HO_2 observations in the cloud-free troposphere and lower stratosphere during SUCCESS, *Geophysical Research Letters*, *25*, 1701-1704.

Brune, W. H., D. Tan, I. F. Faloona, L. Jaegle, D. J. Jacob, B. G. Heikes, J. Snow, Y. Kondo, R. Shetter, G. W. Sachse, B. Anderson, G. L. Gregory, S. Vay, H. B. Singh, D. D. Davis, J. H. Crawford, and D. R. Blake (1999), OH and HO_2 chemistry in the North Atlantic free troposphere, *Geophysical Research Letters*, *26*, 3077-3080.

Cantrell, C. A., G. D. Edwards, S. Stephens, L. Mauldin, E. Kosciuch, M. Zondlo, and F. Eisele (2003), Peroxy radical observations using chemical ionization mass spectrometry during TOPSE, *Journal of Geophysical Research-Atmospheres*, *108*, -.

Chameides, W. L., and D. D. Davis (1982), Chemistry in the Troposphere, *Chemical & Engineering News*, *60*, 38-52.

Chen, G., D. Davis, J. Crawford, B. Heikes, D. O'Sullivan, M. Lee, F. Eisele, L. Mauldin, D. Tanner, J. Collins, J. Barrick, B. Anderson, D. Blake, J. Bradshaw, S. Sandholm, M. Carroll, G. Albercook, and A. Clarke (2001), An assessment of HOx chemistry in the tropical Pacific boundary layer: Comparison of model simulations with observations recorded during PEM tropics A, *Journal of Atmospheric Chemistry*, *38*, 317-344.

Crutzen, P., W. Chameides, B. Huebert, A. Lazrus, W. Heaps, D. Philen, and D. D. Davis (1978), Remote Tropospheric NO and NO_2 Levels as Estimated from Simple NO_x Photochemistry and Insitu Measurements of HNO_3 and OH, *Transactions-American Geophysical Union*, *59*, 1080-1080.

Davis, D., J. B. Nowak, G. Chen, M. Buhr, R. Arimoto, A. Hogan, F. Eisele, L. Mauldin, D. Tanner, R. Shetter, B. Lefer, and P. McMurry (2001), Unexpected high levels of NO observed at South Pole, *Geophysical Research Letters*, *28*, 3625-3628.

Deserves, C. (1994), Gas-Phase Formaldehyde and Peroxide Measurements in the Arctic Atmosphere, *Journal of Geophysical Research-Atmospheres*, *99*, 25391-25398.

Dibb, J. E., M. Arsenault, M. C. Peterson, and R. E. Honrath (2002), Fast nitrogen oxide photochemistry in Summit, Greenland snow, *Atmospheric Environment*, *36*, 2501-2511.

Dibb, J. E., and J. L. Jaffrezo (1997), Air-snow exchange investigations at Summit, Greenland: An overview, *Journal of Geophysical Research-Oceans*, *102*, 26795-26807.

Dibb, J. E., P. A. Mayewski, C. S. Buck, and S. M. Drummey (1990), Beta-Radiation from Snow, *Nature*, *345*, 25-25.

Dibb, J. E., R. W. Talbot, J. W. Munger, D. J. Jacob, and S. M. Fan (1998), Air-snow exchange of HNO_3 and NO_y at Summit, Greenland, *Journal of Geophysical Research-Atmospheres*, *103*, 3475-3486.

Dibb, J. E., and S. I. Whitlow (1996), Recent climate anomalies and their impact on snow chemistry at South Pole, 1987-1994, *Geophysical Research Letters*, *23*, 1115-1118.

Dubowski, Y., A. J. Colussi, and M. R. Hoffmann (2001), Nitrogen dioxide release in the 302 nm band photolysis of spray-frozen aqueous nitrate solutions. Atmospheric implications, *Journal of Physical Chemistry A*, *105*, 4928-4932.

Eisele, F. L., and J. D. Bradshaw (1993), The Elusive Hydroxyl Radical Measuring OH in the Atmosphere, *Analytical Chemistry*, *65*, A927-.

Eisele, F. L., R. L. Mauldin, D. J. Tanner, C. Cantrell, E. Kosciuch, J. B. Nowak, B. Brune, I. Faloona, D. Tan, D. D. Davis, L. Wang, and G. Chen (2001), Relationship between OH measurements on two different NASA aircraft during PEM Tropics B, *Journal of Geophysical Research-Atmospheres*, *106*, 32683-32689.

Eisele, F. L., G. H. Mount, D. Tanner, A. Jefferson, R. Shetter, J. W. Harder, and E. J. Williams (1997), Understanding the production and interconversion of the hydroxyl radical during the Tropospheric OH Photochemistry Experiment, *Journal of Geophysical Research-Atmospheres*, *102*, 6457-6465.

Eisele, F. L., D. J. Tanner, C. A. Cantrell, and J. G. Calvert (1996), Measurements and steady state calculations of OH concentrations at Mauna Loa observatory, *Journal of Geophysical Research-Atmospheres*, *101*, 14665-14679.

Faloona, I., D. Tan, W. H. Brune, L. Jaegle, D. J. Jacob, Y. Kondo, M. Koike, R. Chatfield, R. Pueschel, G. Ferry, G. Sachse, S. Vay, B. Anderson, J. Hannon, and H. Fuelberg (2000), Observations of HO_x and its relationship with NO_x in the upper troposphere during SONEX, *Journal of Geophysical Research-Atmospheres*, *105*, 3771-3783.

Fehsenfeld, F. C., R. R. Dickerson, G. Hubler, W. T. Luke, L. J. Nunnermacker, E. J. Williams, J. M. Roberts, J. G. Calvert, C. M. Curran, A. C. Delany, C. S. Eubank, D. W. Fahey, A. Fried, B. W. Gandrud, A. O. Langford, P. C. Murphy, R. B. Norton, K. E. Pickering, and B. A. Ridley (1987), A Ground-Based Intercomparison of NO, NO_x, and NO_y Measurement Techniques, *Journal of Geophysical Research-Atmospheres*, *92*, 14710-14722.

Frey, M. M., R. W. Stewart, J. R. McConnell, and R. C. Bales (2005), Atmospheric hydroperoxides in West Antarctica: Links to stratospheric ozone and atmospheric oxidation capacity, *Journal of Geophysical Research-Atmospheres*, *110*, -.

George, L. A., T. M. Hard, and R. J. O'Brien (1999), Measurement of free radicals OH and HO2 in Los Angeles smog, *Journal of Geophysical Research-Atmospheres*, *104*, 11643-11655.

Grannas, A. M., P. B. Shepson, C. Guimbaud, A. L. Sumner, M. Albert, W. Simpson, F. Domine, H. Boudries, J. Bottenheim, H. J. Beine, R. Honrath, and X. L. Zhou (2002), A study of photochemical and physical processes affecting carbonyl compounds in the Arctic atmospheric boundary layer, *Atmospheric Environment*, *36*, 2733-2742.

Hack, W., A. W. Preuss, F. Temps, H. G. Wagner, and K. Hoyermann (1980), Direct Determination of the Rate-Constant of the Reaction $NO+HO_2 \rightarrow NO_2+OH$ with the Lmr, *International Journal of Chemical Kinetics*, *12*, 851-860.

Hammer, C., P. A. Mayewski, D. Peel, and M. Stuiver (1997), Untitled - Preface, *Journal of Geophysical Research-Oceans*, *102*, 26315-26316.

Hausmann, M., and U. Platt (1994), Spectroscopic Measurement of Bromine Oxide and Ozone in the High Arctic during Polar Sunrise Experiment 1992, *Journal of Geophysical Research-Atmospheres*, *99*, 25399-25413.

Heard, D. E., and M. J. Pilling (2003), Measurement of OH and HO_2 in the troposphere, *Chemical Reviews*, *103*, 5163-5198.

Holland, F., U. Aschmutat, M. Hessling, A. Hofzumahaus, and D. H. Ehhalt (1998), Highly time resolved measurements of OH during POPCORN using laser-induced fluorescence spectroscopy, *Journal of Atmospheric Chemistry*, *31*, 205-225.

Honninger, G., and U. Platt (2002), Observations of BrO and its vertical distribution during surface ozone depletion at Alert, *Atmospheric Environment*, *36*, 2481-2489.

Honrath, R. E., S. Guo, M. C. Peterson, M. P. Dziobak, J. E. Dibb, and M. A. Arsenault (2000a), Photochemical production of gas phase NO_x from ice crystal NO_3^-, *Journal of Geophysical Research-Atmospheres*, *105*, 24183-24190.

Honrath, R. E., Y. Lu, M. C. Peterson, J. E. Dibb, M. A. Arsenault, N. J. Cullen, and K. Steffen (2002), Vertical fluxes of NO_x, HONO, and HNO_3 above the snowpack at Summit, Greenland, *Atmospheric Environment*, *36*, 2629-2640.

Honrath, R. E., M. C. Peterson, M. P. Dziobak, J. E. Dibb, M. A. Arsenault, and S. A. Green (2000b), Release of NOx from sunlight-irradiated midlatitude snow, *Geophysical Research Letters*, *27*, 2237-2240.

Honrath, R. E., M. C. Peterson, S. Guo, J. E. Dibb, P. B. Shepson, and B. Campbell (1999), Evidence of NO_x production within or upon ice particles in the Greenland snowpack, *Geophysical Research Letters*, *26*, 695-698.

Hutterli, M. A., J. R. McConnell, G. Chen, R. C. Bales, D. D. Davis, and D. H. Lenschow (2004), Formaldehyde and hydrogen peroxide in air, snow and interstitial air at South Pole, *Atmospheric Environment*, *38*, 5439-5450.

Hutterli, M. A., J. R. McConnell, R. W. Stewart, H. W. Jacobi, and R. C. Bales (2001), Impact of temperature-driven cycling of hydrogen peroxide (H_2O_2) between air and snow on the planetary boundary layer, *Journal of Geophysical Research-Atmospheres*, *106*, 15395-15404.

Hutterli, M. A., R. Rothlisberger, and R. C. Bales (1999), Atmosphere-to-snow-to-firn transfer studies of HCHO at Summit, Greenland, *Geophysical Research Letters*, *26*, 1691-1694.

Impey, G. A., C. M. Mihele, K. G. Anlauf, L. A. Barrie, D. R. Hastie, and P. B. Shepson (1999), Measurements of photolyzable halogen compounds and bromine radicals during the Polar Sunrise Experiment 1997, *Journal of Atmospheric Chemistry*, *34*, 21-37.

Impey, G. A., P. B. Shepson, D. R. Hastie, L. A. Barrie, and K. G. Anlauf (1997), Measurements of photolyzable chlorine and bromine during the Polar sunrise experiment 1995, *Journal of Geophysical Research-Atmospheres*, *102*, 16005-16010.

Jacobi, H. W., M. M. Frey, M. A. Hutterli, R. C. Bales, O. Schrems, N. J. Cullen, K. Steffen, and C. Koehler (2002), Measurements of hydrogen peroxide and formaldehyde exchange between the atmosphere and surface snow at Summit, Greenland, *Atmospheric Environment*, *36*, 2619-2628.

Jaegle, L., D. J. Jacob, W. H. Brune, and P. O. Wennberg (2001), Chemistry of HO_x radicals in the upper troposphere, *Atmospheric Environment*, *35*, 469-489.

Jones, A. E., R. Weller, P. S. Anderson, H. W. Jacobi, E. W. Wolff, O. Schrems, and H. Miller (2001), Measurements of NO_x emissions from the Antarctic snowpack, *Geophysical Research Letters*, *28*, 1499-1502.

Korhonen, P., M. Kulmala, A. Laaksonen, Y. Viisanen, R. McGraw, and J. H. Seinfeld (1999), Ternary nucleation of H_2SO_4, NH_3, and H_3O in the atmosphere, *Journal of Geophysical Research-Atmospheres*, *104*, 26349-26353.

Kulmala, M., L. Laakso, K. E. J. Lehtinen, I. Riipinen, M. Dal Maso, T. Anttila, V. M. Kerminen, U. Horrak, M. Vana, and H. Tammet (2004), Initial steps of aerosol growth, *Atmospheric Chemistry and Physics*, *4*, 2553-2560.

Levy, H. (1971), Normal Atmosphere - Large Radical and Formaldehyde Concentrations Predicted, *Science*, *173*, 141-&.

Li, S. M. (1994), Equilibrium of Particle Nitrite with Gas-Phase HONO - Tropospheric Measurements in the High Arctic during Polar Sunrise, *Journal of Geophysical Research-Atmospheres*, *99*, 25469-25478.

Lushnikov, A. A., and A. G. Sutugin (1976), Recent State of Theory on Homogeneous Nucleation, *Uspekhi Khimii*, *45*, 385-415.

Mack, J., and J. R. Bolton (1999), Photochemistry of nitrite and nitrate in aqueous solution: a review, *Journal of Photochemistry and Photobiology a-Chemistry*, *128*, 1-13.

Mauldin, R. L., C. A. Cantrell, M. A. Zondlo, E. Kosciuch, B. A. Ridley, R. Weber, and F. E. Eisele (2003), Measurements of OH, H_2SO_4, and MSA during Tropospheric Ozone Production About the Spring Equinox (TOPSE), *Journal of Geophysical Research-Atmospheres*, *108*, -.

Mauldin, R. L., F. L. Eisele, C. A. Cantrell, E. Kosciuch, B. A. Ridley, B. Lefer, D. J. Tanner, J. B. Nowak, G. Chen, L. Wang, and D. Davis (2001), Measurements of OH aboard the NASA P-3 during PEM-Tropics B, *Journal of Geophysical Research-Atmospheres*, *106*, 32657-32666.

Mauldin, R. L., D. J. Tanner, and F. L. Eisele (1999), Measurements of OH during PEM-Tropics A, *Journal of Geophysical Research-Atmospheres*, *104*, 5817-5827.

Mayewski, P. A., and M. Bender (1995), The GISP2 Ice Core Record - Paleoclimate Highlights, *Reviews of Geophysics*, *33*, 1287-1296.

Michalowski, B. A., J. S. Francisco, S. M. Li, L. A. Barrie, J. W. Bottenheim, and P. B. Shepson (2000), A computer model study of multiphase chemistry in the Arctic boundary layer during polar sunrise, *Journal of Geophysical Research-Atmospheres*, *105*, 15131-15145.

Munger, J. W., D. J. Jacob, S. M. Fan, A. S. Colman, and J. E. Dibb (1999), Concentrations and snow-atmosphere fluxes of reactive nitrogen at Summit, Greenland, *Journal of Geophysical Research-Atmospheres*, *104*, 13721-13734.

Olson, J. R., J. H. Crawford, D. D. Davis, G. Chen, M. A. Avery, J. D. W. Barrick, G. W. Sachse, S. A. Vay, S. T. Sandholm, D. Tan, W. H. Brune, I. C. Faloona, B. G. Heikes, R. E. Shetter, B. L. Lefer, H. B. Singh, R. W. Talbot, and D. R. Blake (2001), Seasonal differences in the photochemistry of the South Pacific: A comparison of observations and model results from PEM-Tropics A and B, *Journal of Geophysical Research-Atmospheres*, *106*, 32749-32766.

Platt, U., and G. Honninger (2003), The role of halogen species in the troposphere, *Chemosphere*, *52*, 325-338.

Prinn, R. (2003a), Is the cleansing capability of the atmosphere (OH concentration) changing?, *Abstracts of Papers of the American Chemical Society*, *226*, U24-U24.

Prinn, R. G. (2003b), The cleansing capacity of the atmosphere, *Annual Review of Environment and Resources*, *28*, 29-57.

Ridley, B., J. Walega, D. Montzka, F. Grahek, E. Atlas, F. Flocke, V. Stroud, J. Deary, A. Gallant, H. Boudries, J. Bottenheim, K. Anlauf, D. Worthy, A. L. Sumner, B. Splawn, and P. Shepson (2000), Is the Arctic surface layer a source and sink of NO_x in winter/spring?, *Journal of Atmospheric Chemistry*, *36*, 1-22.

Riedel, K., W. Allan, R. Weller, and O. Schrems (2005), Discrepancies between formaldehyde measurements and methane oxidation model predictions in the Antarctic troposphere: An assessment of other possible formaldehyde sources, *Journal of Geophysical Research-Atmospheres*, *110*, -.

Riedel, K., R. Weller, and O. Schrems (1999), Variability of formaldehyde in the Antarctic troposphere, *Physical Chemistry Chemical Physics*, *1*, 5523-5527.

Riedel, K., R. Weller, O. Schrems, and G. Konig-Langlo (2000), Variability of tropospheric hydroperoxides at a coastal surface site in Antarctica, *Atmospheric Environment*, *34*, 5225-5234.

Ryerson, T. B., E. J. Williams, and F. C. Fehsenfeld (2000), An efficient photolysis system for fast-response NO_2 measurements, *Journal of Geophysical Research-Atmospheres*, *105*, 26447-26461.

Seinfeld, J. H., and T. E. Ramabhadran (1975), Atmospheric Aerosol Growth by Heterogeneous Condensation, *Atmospheric Environment*, *9*, 1091-1097.

Shaw, G., and G. Wendler (1972), Atmospheric Turbidity Measurements at McCall Glacier in Northern Alaska, *Bulletin of the American Meteorological Society*, *53*, 510-&.

Sigg, A., T. Staffelbach, and A. Neftel (1992), Gas-Phase Measurements of Hydrogen-Peroxide in Greenland and Their Meaning for the Interpretation of H_2O_2 Records in Ice Cores, *Journal of Atmospheric Chemistry*, *14*, 223-232.

Simpson, W. R., M. D. King, H. J. Beine, R. E. Honrath, and M. C. Peterson (2002), Atmospheric photolysis rate coefficients during the Polar Sunrise Experiment ALERT2000, *Atmospheric Environment*, *36*, 2471-2480.

Stoll, H. M. (2006), Climate change - The Arctic tells its story, *Nature*, *441*, 579-581.

Sumner, A. L., P. B. Shepson, A. M. Grannas, J. W. Bottenheim, K. G. Anlauf, D. Worthy, W. H. Schroeder, A. Steffen, F. Domine, S. Perrier, and S. Houdier (2002), Atmospheric chemistry of formaldehyde in the Arctic troposphere at Polar Sunrise, and the influence of the snowpack, *Atmospheric Environment*, *36*, 2553-2562.

Tan, D., I. Faloona, J. B. Simpas, W. Brune, J. Olson, J. Crawford, M. Avery, G. Sachse, S. Vay, S. Sandholm, H. W. Guan, T. Vaughn, J. Mastromarino, B. Heikes, J. Snow, J. Podolske, and H. Singh (2001), OH and HO_2 in the tropical Pacific: Results from PEM-Tropics B, *Journal of Geophysical Research-Atmospheres*, *106*, 32667-32681.

Tanner, D. J., and F. L. Eisele (1995), Present OH Measurement Limits and Associated Uncertainties, *Journal of Geophysical Research-Atmospheres*, *100*, 2883-2892.

Thompson, A. M. (1992), The Oxidizing Capacity of the Earths Atmosphere - Probable Past and Future Changes, *Science*, *256*, 1157-1165.

Walsh, J. E. (1991), Climate Change - the Arctic as a Bellwether, *Nature*, *352*, 19-20.

Wang, Y. H., S. C. Liu, P. H. Wine, D. D. Davis, S. T. Sandholm, E. L. Atlas, M. A. Avery, D. R. Blake, N. J. Blake, W. H. Brune, B. G. Heikes, G. W. Sachse, R. E. Shetter, H. B. Singh, R. W. Talbot, and D. Tan (2001), Factors controlling tropospheric O_3, OH, NO_x and SO_2 over the tropical Pacific during PEM-Tropics B, *Journal of Geophysical Research-Atmospheres*, *106*, 32733-32747.

Weber, R. J., P. H. Mcmurry, F. L. Eisele, and D. J. Tanner (1995), Measurement of Expected Nucleation Precursor Species and 3-500-Nm Diameter Particles at Mauna-Loa-Observatory, Hawaii, *Journal of the Atmospheric Sciences*, *52*, 2242-2257.

Wennberg, P. O., T. F. Hanisco, L. Jaegle, D. J. Jacob, E. J. Hintsa, E. J. Lanzendorf, J. G. Anderson, R. S. Gao, E. R. Keim, S. G. Donnelly, L. A. Del Negro, D. W. Fahey, S. A. McKeen, R. J. Salawitch, C. R. Webster, R. D. May, R. L. Herman, M. H. Proffitt, J. J. Margitan, E. L. Atlas, S. M. Schauffler, F. Flocke, C. T. McElroy, and T. P. Bui (1998), Hydrogen radicals, nitrogen radicals, and the production of O_3 in the upper troposphere, *Science*, *279*, 49-53.

Zhou, X. L., H. J. Beine, R. E. Honrath, J. D. Fuentes, W. Simpson, P. B. Shepson, and J. W. Bottenheim (2001), Snowpack photochemical production of HONO: a major source of OH in the Arctic boundary layer in springtime, *Geophysical Research Letters*, *28*, 4087-4090.

CHAPTER 2

METHODS

2.1 Overview

The hydroxyl radical plays a central role in atmospheric chemistry. However, reliable measurement techniques were unavailable twenty years ago. Early methods used chemical tracers such as ^{14}CO [*Felton et al.,* 1988] and methylchloroform [*Simmonds et al.,* 1988] but experienced difficulty resolving diurnal and spatial trends of OH. These problems were due to the low concentrations (sub-ppt) and short lifetime (~1 sec) of the hydroxyl radical. Since these early methods were indirect they had to be averaged from large spatial and temporal scales. Both issues were addressed by laser induced fluorescence (LIF) [*Mather et al.,* 1997] and chemical ionization mass spectrometry (CIMS) [*Eisele and Tanner,* 1991], two techniques that have been employed widely in recent field campaigns. LIF and CIMS were able to provide measurements of adequate sensitivity and appropriate time response [*Eisele and Bradshaw,* 1993]. The CIMS measurement will be described in this chapter.

The need for pernitric acid measurements at high altitudes and latitudes to constrain HO_x and NO_x budgets has been recently demonstrated [*Chen et al.,* 2004, *Jaegle et al.,* 2001]. CIMS is the only method that has been demonstrated to measure HO_2NO_2 in the atmosphere. During the ISCAT 2000 field campaign the first pernitric acid measurements were collected [*Slusher et al.,* 2002, *Huey et al.,* 2004] and used to constrain a photochemical budget [*Chen et al.,* 2004].

This chapter will be divided into three sections. The first will describe the CIMS in the $OH/HO_2+RO_2/H_2SO_4$ measurement configuration employed at Summit, Greenland. The second details the CIMS configuration used to measure HNO_3, HO_2NO_2, and SO_2 during the ANTCI 2003 field campaign. The final section will detail the 0-D steady state model that was employed to compare measured values.

2.2 CIMS ($OH/HO_2+RO_2/H_2SO_4$ measurement)

The measurements of OH, the sum of HO_2 + RO_2, and sulfuric acid were obtained with a chemical ionization mass spectrometer (CIMS). The techniques used for these measurements were based on the work of *Tanner and Eisele* [1997] and *Edwards et al.* [2003]. The CIMS consisted of an ambient pressure flow tube reactor and an ion source coupled to a quadrupole mass spectrometer (Figure 2.1). The flow reactor was an approximately 15.3 cm long 1.25 cm outer diameter (o.d.) stainless steel tube biased at roughly -190 V. Ambient air was transported at 5.0 slpm into this tube from the inlet to within ~1.5 cm of the sampling pinhole for the mass spectrometer. The flow reactor was equipped with two sets of opposed injectors, 0.0125 cm inner diameter (i.d). x 0.080 cm o.d. stainless steel tubes, placed approximately 5 cm apart (Figure 2.3). Addition of SO_2 and NO through the front injectors (total flow ~35 sccm) allowed for conversion of OH and peroxy radicals to sulfuric acid (see section 2.2.1). Addition of an OH scavenger, hexafluoropropene C_3F_6 (6-12 sccm), through the rear injectors allowed for termination of the radical chemistry [*Dubey et al.,* 1996].

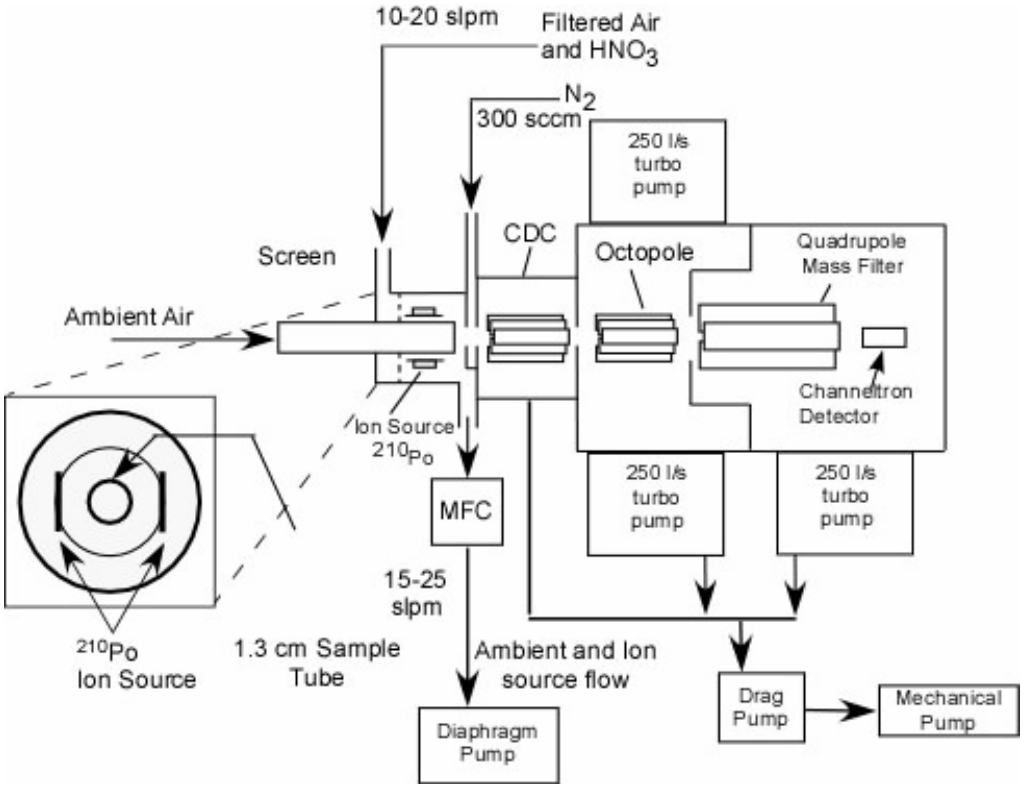

Figure 2.1 Schematic of the ($OH/HO_2+RO_2/H_2SO_4$) Chemical Ionization Mass Spectrometer

Ions were produced by emission of α-particles from a ^{210}Po foil (nominal activity 1.0 mCu) in the annular space between the 1.91 cm o.d. and 2.54 cm o.d. stainless steel tubes. These tubes are concentric with the downstream end of the flow reactor and were held at a potential -220 V. A flow of 20 slpm filtered ambient air doped with nitric acid and C_3F_6 was maintained in the ion source with a diaphragm pump (GAST DOA-V128) and mass flow controller (MKS 1559A). The flow from both the ion source and flow tube was exhausted through another mass flow controller (MKS 1559A) and a second diaphragm pump (KNF-813). Alpha particles from the polonium foil that interacted with the carrier gas formed positive ions and thermalized electrons on a short time scale. These electrons initiate formation of NO_3^- ions and $NO_3^-\bullet(HNO_3)_n$ cluster ions by the following reactions [*Fehsenfeld et al.,* 1975; *Eisele,* 1986].

1) $O_2 + e^- \rightarrow O_2^-$

2) $O_2^- + H_2O \rightarrow OH^- + HO_2$

3) $OH^- + HNO_3 \rightarrow NO_3^- + H_2O$

4) $HNO_3 + e^- \rightarrow NO_2^- + OH$

5) $HNO_3 + NO_2^- \rightarrow NO_3^- + HONO$

6) $HNO_3 + NO_3^- + M \rightarrow NO_3^-\cdot(HNO_3) + M$

The nitrate ions from the source reacted with sulfuric acid by reaction 7 to allow for selective detection as HSO_4^- [*Viggiano et al.,* 1982].

7) $H_2SO_4 + NO_3^-\cdot(HNO_3) \rightarrow HSO_4^-\cdot(HNO_3) + HNO_3$

The potentials of the flow tube and ion source were empirically set to maximize the interaction of the nitrate with the ambient ions exiting the flow tube (Table 2.1 and Figure 2.2). This also maximized the signal levels but did not lead to excessive mixing of the ambient and ion flows which would minimize detection of the HO_x radicals generated in the ion source.

Table 2.1 Voltage sequence used to guide anions to the detection chamber

Voltages	
Ion Source	-220 V
Flow Tube	-190 V
N_2 Buffer	-100 V
Pinhole	-50 V
Collision Dissociation Chamber	-49 V

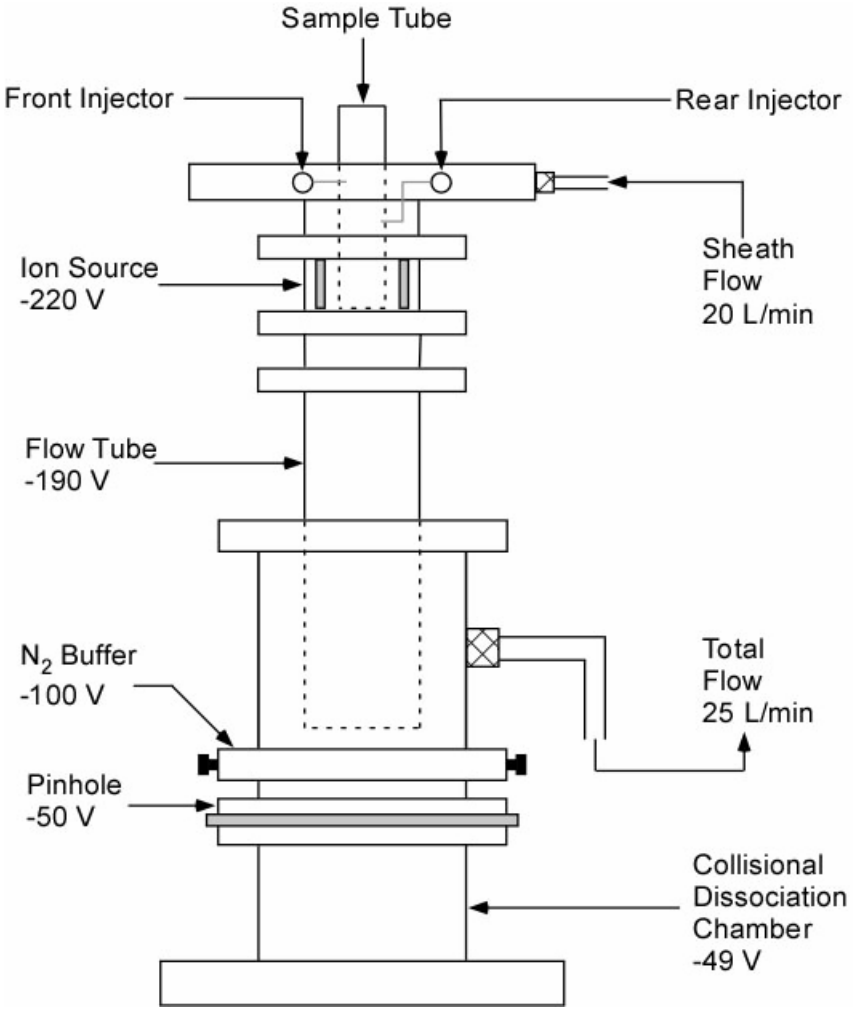

Figure 2.2 Schematic of the front end of the $OH/HO_2/H_2SO_4$ CIMS

A small portion of the effluent of the drift tube (~150 sccm) was sampled by the mass spectrometer which was divided into three differentially pumped chambers. The first chamber was a collision dissociation chamber (CDC) maintained at ~0.4 torr with a drag pump (Alcatel MDP 5011). The CDC is a region of high ion kinetic energy (i.e., high electric field to number density ratio) where cluster ions of nitric acid and/or water are dissociated to simplify the mass spectra.

8) $M + HSO_4^- \cdot (HNO_3) \rightarrow HSO_4^- + HNO_3 + M$

9) $M + HSO_4^- \bullet (H_2O) \rightarrow HSO_4^- + H_2O + M$

The second chamber was the octopole ion guide chamber maintained at 1-2x10^{-3} torr by two turbo molecular pumps (Varian 300HT). The octopole focused the ions from the CDC to the final chamber which contained the quadrupole mass filter and detector. The mass selected output of the quadrupole was detected by a channeltron ion multiplier (K&M 7550). The pressure of the quadrupole chamber was maintained at ~2.0x10^{-5} torr with a third turbo molecular pump (Varian 300HT). The output of the channeltron was amplified and counted as individual ions using standard techniques.

2.2.1 Conversion Chemistry

The nitrate ion chemistry, reaction 7, allowed efficient detection of only a few very strong gas phase acids such as sulfuric, methanesulfonic, and malonic [*Eisele,* 1989]. Consequently, OH and peroxy radicals were converted to sulfuric acid by reactions 10-12 and detected via reaction 7 as described in *Eisele and Tanner* [1997]. OH was titrated by an excess of isotopically labeled sulfur dioxide added to the flow tube (10 sccm 0.9% $^{34}SO_2$ in N_2) through the front set of injectors. This initiated the following series of reactions in the sampled air.

10) $OH + {}^{34}SO_2 \rightarrow HO{}^{34}SO_2$

11) $HO{}^{34}SO_2 + O_2 \rightarrow HO_2 + {}^{34}SO_3$

12) ${}^{34}SO_3 + 2H_2O \rightarrow H_2{}^{34}SO_4 + H_2O$

The use of $^{34}SO_2$ allowed for simultaneous detection of ambient sulfuric (HSO_4^-) at 97 amu and ambient hydroxyl ($H^{34}SO_4^-$) at 99 amu.

Peroxy radicals (HO_2+RO_2) were converted to OH by addition of NO (15 sccm 0.1% NO in N_2) to the flow tube via the front injectors. The OH was then detected by

conversion to H_2SO_4. However, the addition of NO can also lead to formation of nitrous acid.

13) $OH + NO \rightarrow HONO$

Reaction 13 effectively tied up OH and prevented it from being detected by the CIMS. Consequently, the key parameter for the HO_2+RO_2 measurement was the ratio of [NO] to [SO_2] in the flow tube. In general as the [NO]/[SO_2] increased (above a threshold level) the detection efficiency decreased [*Edwards et al.,* 2003]. During the summer 2003 campaign the [NO]/[SO_2] was set in the range of 0.1 to 0.2 to achieve a detection efficiency of 0.5 to 1.0.for HO_2+RO_2. Figure 2.3 depicts the predicted H_2SO_4 production from HO_2 as a function of NO addition based on the analytical solution from *Edwards et al.* [2003]. The actual efficiency of the cycling of HO_2 to OH was determined from the ratio of the peroxy calibration to the hydroyl calibration (see section 2.2.3)

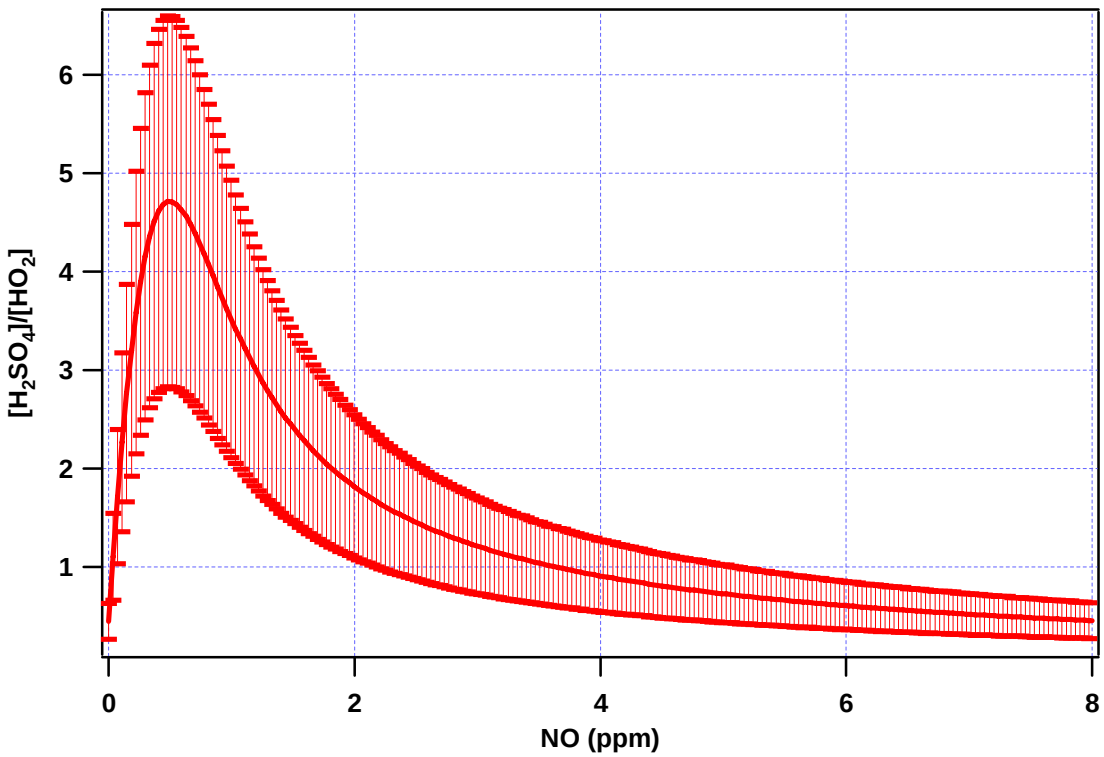

Figure 2.3 Predicted yields of sulfuric acid versus NO at a fixed SO_2 mixing ratio of 32 ppmv. The mixing ratios of NO used during the Summit 2003 field campaign ranged from 3.2 to 6.4 ppmv. The reaction time was 100ms. The estimated uncertainty due to kinetic parameters is ±40%

2.2.2 CIMS configuration and inlet

During the summer 2003 campaign the CIMS and all control electronics were deployed in a temperature regulated sheet metal enclosure placed directly on the snowpack (1.0m deep x 1.1m wide x 1.5m high). The CIMS inlet protruded approximately 20 cm through the roof of the enclosure to minimize shading effects. The inlet (Figure 2.4) consisted of a 7.7cm i.d. x 50 cm long aluminum pipe. A flow of approximately 2400 slpm, corresponding to a velocity of ~8 m/s, was maintained in the inlet with a regenerative blower. The CIMS flow tube was mounted near the downstream end of the inlet in the center of a turbulence reducing screen. A pitot tube was positioned just off the axis of the inlet to continuously monitor the flow velocity. A temperature controlled mercury lamp equipped with a 185nm bandpass filter (Omega Optical) was

mounted in the wall of the pipe to serve as the calibration source of OH and HO_2 radicals (see below).

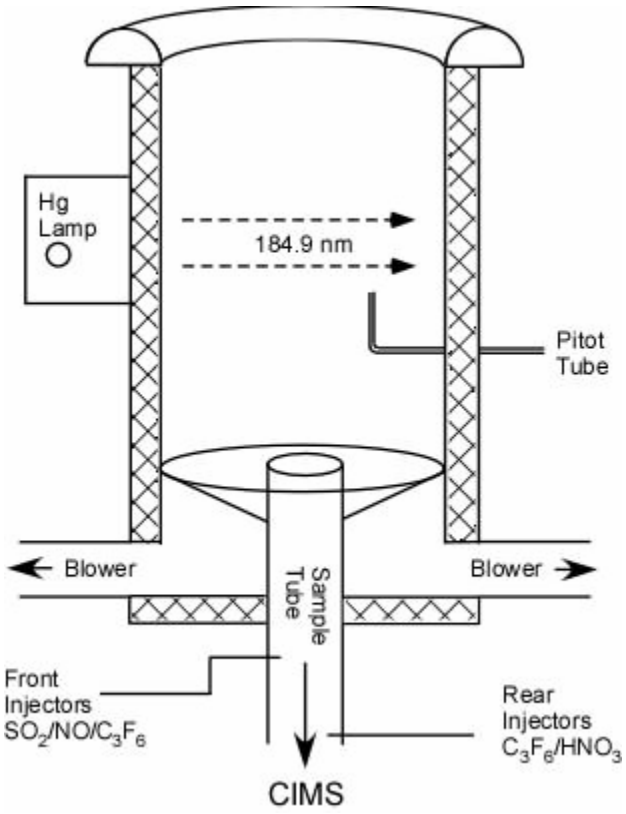

Figure 2.4 Schematic of the (OH/HO_2+RO_2/H_2SO_4) CIMS inlet

The configuration of the CIMS in the heated enclosure was designed for continuous operation for most of the campaign. However, two significant problems were encountered with the experimental design. The first of these was observed during the initial measurement period which was characterized by calm winds and clear skies. These conditions gave rise to significant solar heating of the enclosure including the downstream end of the inlet and the flow tube. As a result the conversion efficiency of SO_3 to H_2SO_4, reaction 12, was attenuated due to the strong negative temperature dependence of the reaction of SO_3 with H_2O [*Lovejoy et al.,* 1996]. This difficulty was overcome by insulating the inlet and the flow tube from the interior of the enclosure thus lowering the temperature of the neutral reaction region. The second problem was the

formation of rime ice on both the inlet screen and flow tube. This primarily occurred during calm evenings when radiation fog was formed. An automated fix for this problem was not found which necessitated frequent cleanings.

2.2.3 Calibration

Since it was impossible to obtain an OH standard, calibrations were performed in the field using ambient water vapor. A mercury lamp was employed to photolyze water within the inlet generating both OH and HO_2.

14) $H_2O + h\nu \rightarrow H + OH$

15) $H + O_2 \rightarrow HO_2$

In order to quantify the amount of OH formed from the photon flux from the Hg lamp, the absorption cross-section of H_2O at 184.9 nm and the number density of ambient water vapor were required.

$$\text{Eq 1)} \quad [OH] = \phi_{184.9nm}\sigma_{H_2O}[H_2O]$$

The photon flux ($\phi_{184.9nm}$) was obtained using three photodiodes to scan the area of the inlet where photolysis occurred. The amperages obtained from the photodiodes that were used for field measurements were later referenced to a NIST CsI photodiode in the lab. The velocity and the width of the illuminated sample were also required to calculate the photon flux. The velocity of the calibration sample was obtained from a pitot tube installed within the inlet.

$$\text{Eq 2)} \quad \phi_{184.9nm} = \frac{photons}{((width)(velocity))} = \frac{photons}{area}$$

The absorption cross section of water at 184.9 nm (σ_{H_2O}) is 7.2x10^{-20} cm^2 photon^{-1} [*Cantrell et al,* 1997]. The number density of water ([H_2O] in molecules cm^{-3}) was obtained from a commercially available dew point meter (Vaisala HMM 211).

The measurement of OH was also dependent on the ratio of the signal of $H^{34}SO_4^-$ (99 amu) to the signal of the reagent ion NO_3^- (62 amu) multiplied by the calibration conversion (1/kt). Because NO_3^- is orders of magnitude larger than $H^{34}SO_4^-$ the reaction is pseudo first order. The concentration of sulfuric acid (formed from titration of OH) is obtained from equation 3.

$$\text{Eq 3)}\ [H_2{}^{34}SO_4] = \left(\frac{1}{kt}\right)\frac{[H^{34}SO_4^-]_t}{[NO_3^-]_t}$$

Since ~4% of ambient sulfuric acid contains the ^{34}S isotope [$H_2{}^{34}SO_4$] ≈ [OH]. This last assumption can breakdown in polluted environments but was not a problem at Summit.

$$\text{Eq 4)}\ [OH] \cong \left(\frac{1}{kt}\right)\frac{[H^{34}SO_4^-]_t}{[NO_3^-]_t}$$

By setting both equations (1 and 4) for hydroxyl number density equal to one another the calibration conversion can be calculated.

$$\text{Eq 5)}\ \frac{1}{kt} = \phi_{184.9}\sigma_{H_2O}[H_2O]\left(\frac{[NO_3^-]_t}{[H^{34}SO_4^-]_t}\right)$$

The calculated calibration conversion for the summer field campaign was 1.8x10^{10} molecules cm^{-3}. Since photolysis of water forms both an OH and HO_2 radical, reactions 14-15, the ratio of ultraviolet generated HO_2+RO_2 signal to OH signal should be 1:1. Deviation from this ratio was used to empirically determine the NO over/under cycling of the observed peroxy signal.

2.2.4 Measurement and Background

Data were collected on a ~7 sec cycle, stepping through the reagent ion (NO_3^- = 62 amu) and the signal ions (HSO_4^-=97 amu, $H^{34}SO_4^-$ =99 amu). After some early experimentation a 20 minute duty cycle was established for radical measurement (see Figure 4). For the first three minutes of the measurement cycle NO was added from the front injectors to cycle the peroxy radicals to OH. To determine the background 8 sccm of C_3F_6 was added through a VALCO switching valve to front injectors for 90 seconds every five minutes. The background measurement was triggered halfway though the NO injection to provide a peroxy radical background. In the absence of C_3F_6 and/or NO a mixture of SO_2 and N_2 flowed through the front injectors to measure OH. A complication in the OH measurement arose due to the time required to turn off the NO flow through the injector. This perturbed the first OH measurement period after a HO_2+RO_2 cycle. The enhancement of OH signal is represented by the boxed region pointed to by the blue arrow in figure 2.5. Therefore these measurements were excluded from the data set and only the last two OH measurement periods were reported.

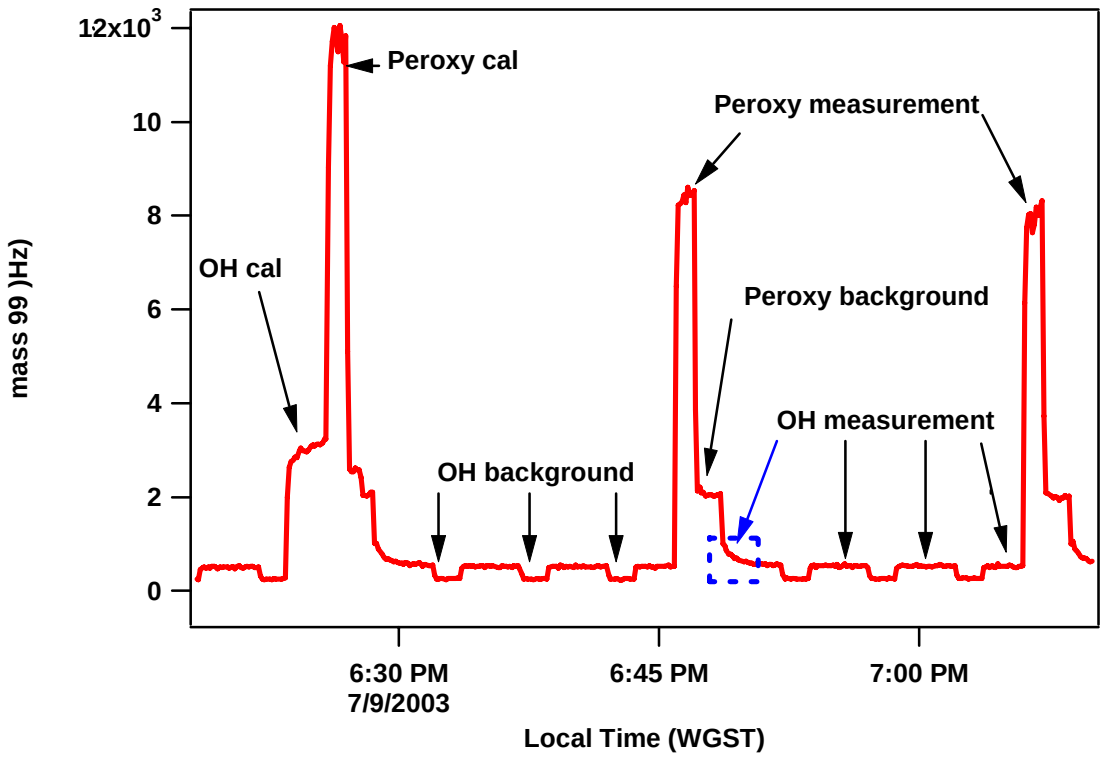

Figure 2.5 Hydroxyl and peroxy duty cycle for the summer 2003 field campaign.

During the spring 2004 field campaign the NO was purged from the tubing with a flow N_2 to a diaphragm pump (Figure 2.6). Figure 2.6 displays the spring 2004 system in hydroxyl background mode. A constant flow of 12 sccm SO_2 flowed to the front injectors regardless of the instrument mode as in the summer 2003 configuration. When in background mode 8 sccm of C_3F_6 was directed to the front injectors. However, in the spring 2004 configuration 38 sccm of dry nitrogen flowed from the front N_2 mass flow controller when in hydroxyl background mode. The flow was split between the front injectors and the diaphragm pump. A 20 sccm flow to the diaphragm pump was maintained by the effluent mass flow controller. It was this 20 sccm flow of N_2 that flushed any remaining NO rapidly out to a diaphragm pump. The remaining 18 sccm of N_2 went to the front injectors. Thus the total flow to the front injectors in OH

background mode was 38 sccm (SO_2 = 12 sccm, pulsed C_3F_6 = 8 sccm, front N_2 = 18 sccm).

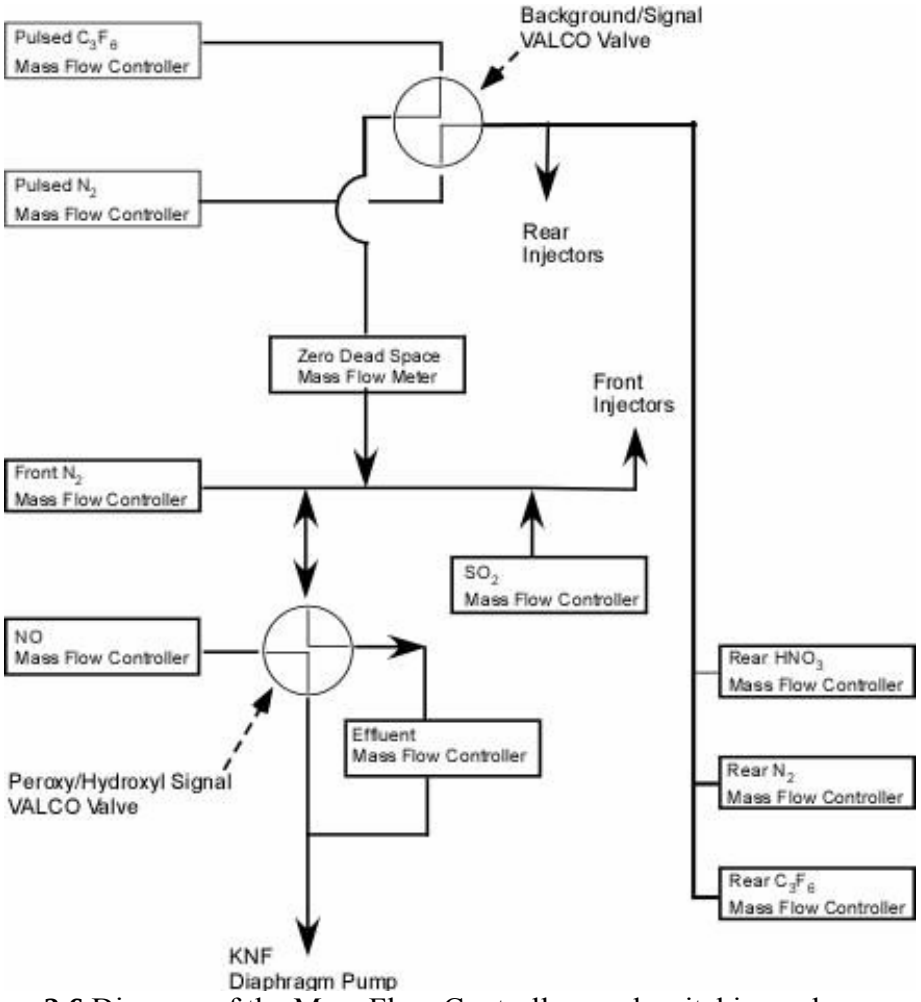

Figure 2.6 Diagram of the Mass Flow Controllers and switching valves used for measurements and backgrounds (peroxy measurement mode)

When in the hydroxyl measurement mode, the background/signal VALCO switching valve was thrown and 8 sccm of nitrogen flowed from the pulsed N_2 mass flow controller to the front injectors, replacing the 8 sccm of C_3F_6 (SO_2 = 12 sccm, pulsed N_2 = 8 sccm, front N_2 = 18 sccm). In peroxy measurement mode the peroxy/hydroxyl VALCO switching valve was thrown and 15 sccm of the NO addition (0.203% NO in N_2) was directed to the front injectors. Simultaneously, the flow from the front N_2 injector was reduced from 38 to 3 sccm (SO_2 =12 sccm, pulsed N_2 = 8 sccm, NO = 15 sccm, front N_2

= 3 sccm). Finally, in peroxy background mode the signal/ background switching valve was thrown again and 8 sccm of C_3F_6 replaced the 8 sccm of N_2 (SO_2 = 12 sccm, pulsed C_3F_6 = 8 sccm, NO = 15 sccm, front N_2 = 3sccm). In both measurement modes the total flow to the front injectors was 38 sccm keeping the dynamics constant within the sample tube. Table 2.2 lists all flows used during the spring 2004 field campaign; the flows to the front injectors for measurement mode are listed in red.

Table 2.2 Gas flows used during spring 2004 field campaign

Mass Flow Controller	Peroxy Measurement	Hydroxyl Measurement
#1 Total Flow	25 slpm	25 slpm
#2 Sheath Flow	20 slpm	20 slpm
#3 Rear HNO_3	28 sccm	28 sccm
#4 Rear N_2	15 sccm	15 sccm
#5 Rear C_3F_6	1 sccm	1 sccm
#6 Front N_2	3 sccm	38 sccm
#7 Front SO_2	12 sccm	12 sccm
#8 Front C_3F_6	8 sccm	8 sccm
#9 Front N_2	8 sccm	8 sccm
#10 Pinhole N_2	300 sccm	300 sccm
#11 Effluent flow	0 sccm	-20 sccm
#12 NO flow	15 sccm	0 sccm
Total Flow (front injectors)	38 sccm	38 sccm

Figure 2.7 shows the measurement cycle used during the spring 2004 field campaign. The improvements in the switching time of NO addition were apparent in the OH measurements immediately following the peroxy measurements. Since OH concentrations were expected to be attenuated during the spring two changes were made to the measurement cycle. Because the time to cycle for HO_2+RO_2 to OH was reduced the hydroxyl measurement period was extended and the number of peroxy measurements was increased. OH concentrations were expected to be at or near the limit of detection around the vernal equinox at Summit; therefore, it was important to increase the number of peroxy measurements in this environment.

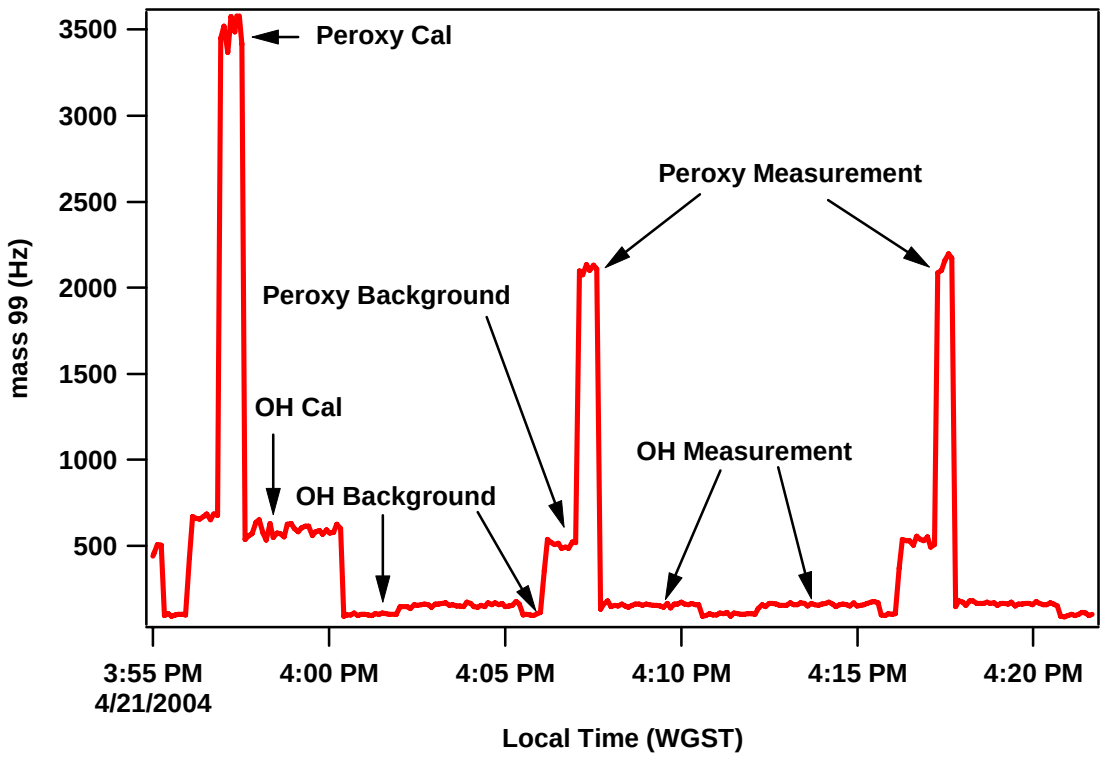

Figure 2.7 Hydroxyl and peroxy duty cycle for the spring 2004 field campaign

2.2.5 Accuracy and Limit of Detection

The accuracy of the measurement depended on the uncertainty inherent in the absorption cross section of water at 184.9 nm, the diodes used to measure the photon flux, the velocity measured inside the inlet, and the water concentration obtained from the dew point monitor. The absorption cross section is known within 5% (Cantrell et al., 1997). The accuracy of the dew point monitor (see below) was 1 °C between -10 and -40 °C. This translated into an uncertainty of 20%.in measured H_2O concentration. The uncertainty inherent in obtaining the photon flux was estimated at 12% and the velocity of the inlet was known within 2%. For the summer 2003 campaign the statistical error at the 3σ level for the OH calibration signal was typically 9%. This gives a total estimated uncertainty for the CIMS OH measurement of 25%. The statistical error at the 3σ level for the peroxy calibration was 25% leading to a measurement uncertainty of 37%. The

uncertainties are summarized in Table 2.3. The limit of detection for OH was approximately $1.3x10^5$molecules cm^{-3} for a 10 minute integration period and was estimated as three standard deviations of the background measurement.

Table 2.3 Summary of the uncertainties in the $OH/HO_2/H_2SO_4$ measurement for the summer 2003 field campaign

Uncertainty in the peroxy and hydroxyl measurements	
Absorption cross-section of H_2O at 184.9 nm	5%
Photon Flux (Diodes)	12%
Inlet Velocity (Pitot tube)	2%
$[H_2O]$ Dew point meter	20%
3σ statistical error for OH calibration	9%
3σ statistical error for the peroxy calibration	25%

The spring 2004 measurement uncertainties for the absorption cross section, H_2O concentration, photon flux and inlet velocity were the same as for the summer 2003 campaign. The 3σ statistical error was again 9% for the OH measurement, while the 3σ statistical error for the peroxy measurement improved dramatically to 10%. The reasons for this improvement were a direct result of changes in the timing sequence for the background and calibrations. The new cycle provided longer uninterrupted peroxy calibrations and the number of useable HO_2+RO_2 calibrations was increased by a factor of four. The limit of detection was calculated from the hourly average of the background in the spring. A limit of detection of $2.0x10^5$ molecules cm^{-3} was derived from three standard deviations of the hourly averaged background.

2.3 CIMS ($HNO_3/HO_2NO_2/SO_2$) instrument

Ambient measurements of pernitric acid, nitric acid, and sulfur dioxide were obtained using a CIMS instrument located on the second floor of the Atmospheric Research Observatory during the ANTCI 2003 field campaign. The mass spectrometer set up is similar to the $OH/HO_2+RO_2/H_2SO_4$ instrument used at Summit. However, the inlet configuration and ion chemistry were different and will be addressed in sections 2.3.1 and 2.3.2.

The mass spectrometer was again divided into three differentially pumped chambers (Figure 2.8). The first was a collision dissociation chamber (CDC) that was maintained at a pressure of ~0.4 torr by a molecular drag pump (Alcatel MDP 5011). The voltage of the CDC was empirically set at 108V. The second chamber contained the octopole ion guide chamber and was maintained at ~$1.0x10^{-3}$ torr by a turbo molecular pump (Varian 300HT). The masses were again selected by a quadrupole mass filter. The third chamber housed a channeltron detector and was maintained at a pressure ~$5.0x10^{-5}$ torr by a second turbo molecular pump (Varian 300HT).

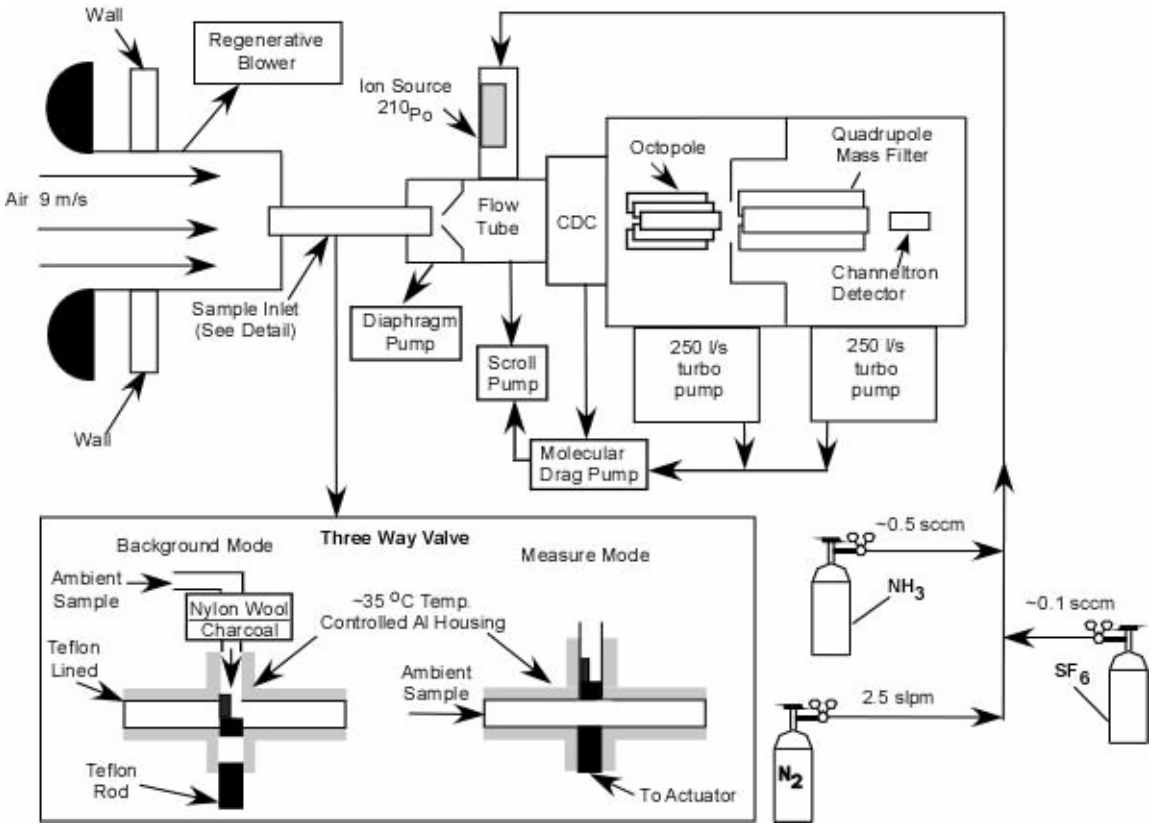

Figure 2.8 Schematic of $HNO_4/HNO_3/SO_2$ CIMS used during the ANTCI 2003 field campaign

2.3.1 Inlet Configuration

The high flow section of the $HNO_3/HNO_4/SO_2$ inlet was the identical to the inlet $OH/HO_2+RO_2/H_2SO_4$ measurement (Figure 2.4). Air was sampled through a 7.7cm i.d. x 50 cm aluminum inlet located 10 meters above the snow in the Atmospheric Research Observatory. The inlet was oriented so that it was facing the clean air sector, an area of restricted travel and upwind of the Amundsen-Scott station. A flow rate of ~2400 slpm was maintained inside the aluminum pipe by a regenerative blower.

The primary change in the $HNO_3/HO_2NO_2/SO_2$ measurement configuration was the addition of a heated three way valve to the front end of the mass spectrometer to

obtain background measurements. Two 9.53 mm o.d. Teflon tubes mated to a cylindrical Teflon shaft in the three way valve (inset Figure 2.8 and Figure 2.9). The position of the Teflon shaft determined whether the instrument was in measurement or background mode and was periodically shifted by a pneumatic cylinder. When in measurement mode outside air passed through what was essentially a 20 cm Teflon sample tube leading to the aperture of the flow tube. In background mode outside air was diverted through a scrubber containing nylon wool and charcoal before entering the flow tube. The entire apparatus was housed in an aluminum block maintained at a temperature of 40C.

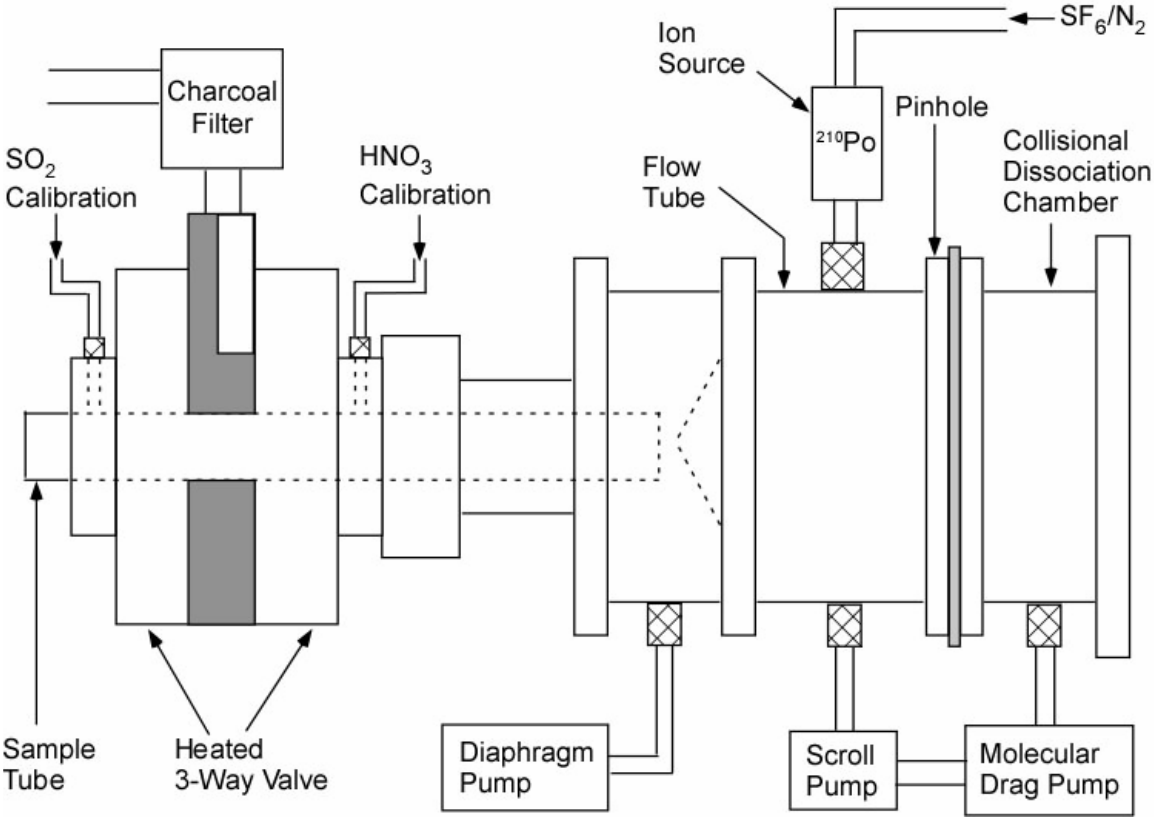

Figure 2.9 Schematic of the front end of the $HNO_3/HO_2NO_2/SO_2$ CIMS

The flow tube in $HNO_3/HNO_4/SO_2$ measurement configuration was a 3.5 cm i.d. x 10.2 cm stainless steel tube biased at -109V (Figure 2.9). A pressure of ~11 torr was maintained within the flow reactor by a Varian (PTS-300) scroll pump. Reagent ions

were produced by ^{210}Po alpha particle emitter. A flow of 2.6 slpm of dry nitrogen transported the reagent ions into the flow tube to react with the air sample. After reacting the ions then entered the Collisional Dissociation Chamber through a 0.030" pinhole.

Table 2.4 Flows and voltages used in $HNO_4/HNO_3/SO_2$ CIMS configuration

Flows	
Total Flow into Sample Tube	7.8 slpm
Diaphragm Pump (Overflow)	6.8 slpm
Sample flow	1.0 slpm
HNO_3 calibration	19.1 sccm
SO_2 calibration	19.9 sccm
Ion Source	2.6 slpm
Voltages	
Collision Dissociation Chamber	-109V
Pinhole	-108

2.3.2 Ion Chemistry and measurement cycle

The reagent ion SF_6^- was formed by attachment of thermalized electrons to sulfur hexafluoride (SF_6).

16) $SF_6 + e^- \rightarrow SF_6^-$

HNO_3, HNO_4 and SO_2 react with SF_6^- to form the following product ions [*Huey et al.*, 1995, *Slusher et al.*, 2001].

17a) $SF_6^- + HNO_3 \rightarrow NO_3^-\bullet HF + SF_5$

17b) $\rightarrow SF_5^- + HF + NO_3$

17c) $\rightarrow SF_5NO_3^- + ?$

17d) $\rightarrow NO_3^- + ?$

18a) $SF_6^- + HO_2NO_2 \rightarrow NO_4^-\bullet HF + SF_5$

18b) $\rightarrow SF_5^- + HF + O_2 + ?$

18c) $\rightarrow NO_2^-\bullet HF + SF_5 + O_2$

18d) $\rightarrow NO_3^- + ?$

19a) $SF_6^- + SO_2 \rightarrow F_2SO_2^- + SF_4$

19b) $\rightarrow SF_5^- + FSO_2$

19c) $\rightarrow FSO_2^- + SF_5$

The first reaction in each sequence was responsible for the product ion measured. In the reactions of SF_6^- with HNO_3 and SO_2 (reactions 17a and 19a) represented the channels with the greatest yield, ~92% and ~54% respectively. In the HNO_4 reaction the fluoride transfer represented a minor transfer channel (~25%) but produced a product ion that was selective to pernitric acid. The reagent ion and product ions were all measured sequentially. A typical duty cycle consisted of measuring 146 amu (SF_6^-) for 50 ms, 82 amu (NO_3^-•HF) for 2 s, 98 amu (NO_4^-•HF) for 2 s, and 102 amu ($F_2SO_2^-$) for 500 ms. Background measurements were collected every 15 minutes by diverting ambient flow through a low pressure drop filter (see figures 2.8-2.9).

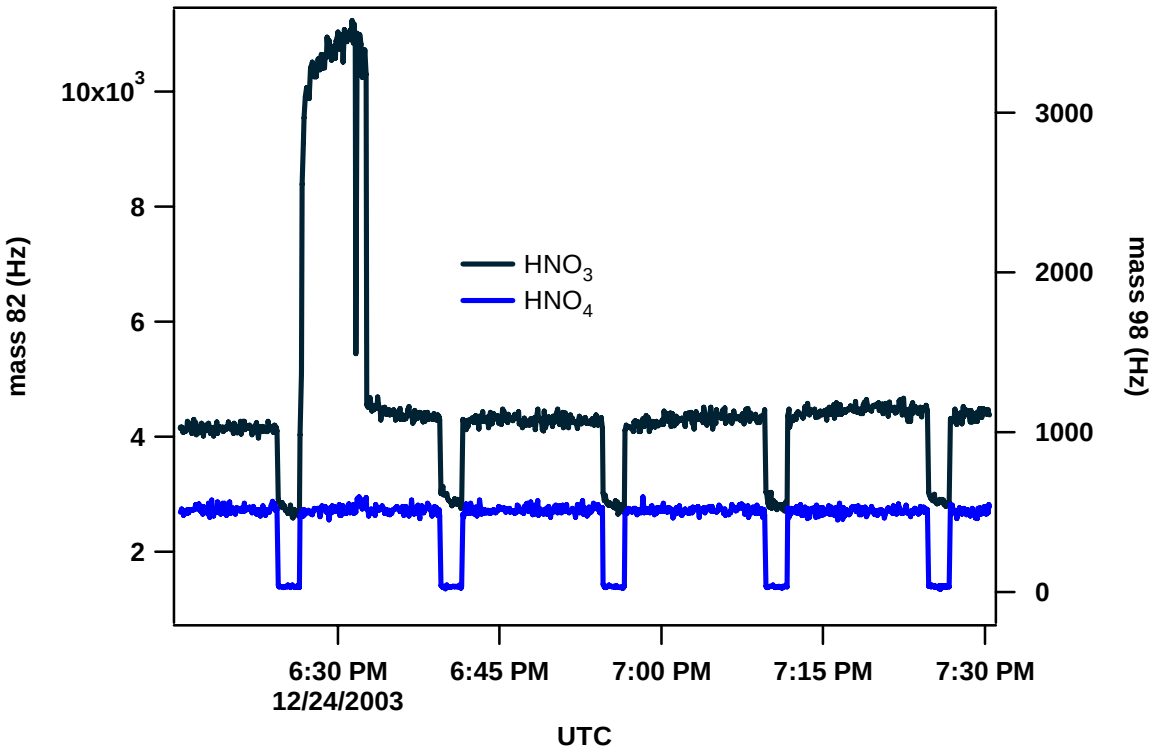

Figure 2.10 Pernitric and nitric acid duty cycle for the ANTCI 2003 field campaign

2.3.3 Calibration

On site calibrations of HNO_3 and SO_2 were performed every two hours with permeation tubes maintained at 40C. The permeation rate of the nitric acid calibration was 21.65 ng min^{-1} and entered the inlet flow (6.8slpm) at a rate of 20 sccm producing a mixing ratio of 1132 pptv. The permeation rate of the sulfur dioxide calibration was 172 ng min^{-1} and entered the inlet flow to produce a mixing ratio of 8853 pptv. Typical sensitivities for HNO_3 and SO_2 were 7 and 13 Hz per ppt respectively.

Calibration of pernitric acid had to be performed after the mission. The pernitric acid was synthesized in the lab from $BF_4 \bullet NO_2$ salt dissolved in concentrated H_2O_2 as described in Kenley et al., (1981). The pernitric acid standard solution was placed in a chilled ethanol bath at -30 C. to minimize thermal decomposition. Dry nitrogen was bubbled through the pernitric standard to deliver HO_2NO_2 to the CIMS. Pernitric acid was then thermally decomposed to NO_2 at ~90C and the decrease of pernitric acid (mass 98) was ratioed to the increase in NO_2 (mass46). The decrease in HO_2NO_2 from thermal decomposition was compared to the concomitant increase in NO_2 (reaction 20).

20) $SF_6^- + NO_2 \rightarrow NO_2^- + SF_6$

The sensitivities of the CIMS to NO_2 and SO_2 were obtained by calibration to gravimetrically prepared standards, NO_2 = 99.8 ppm (Scott-Marin) and SO_2 = 1.59 ppm (Scott-Marin). From the thermal decomposition of HO_2NO_2 and the calibration to the standards a ratio of the sensitivity of pernitric acid to sulfur dioxide (HO_2NO_2/SO_2 = 0.80) was calculated. A sensitivity of 10 pptv was derived for the CIMS during the ANTCI 2003 mission.

2.3.4 Accuracy and Limit of Detection

The estimated uncertainty of HNO_3 and SO_2 were derived from the uncertainty of the standards and the precision (2σ) of the calibrations obtained in the field The SO_2 permeation tube was calibrated using a 1.59 ppm SO_2 standard cylinder (Scott-Marin). The uncertainty of the gas cylinder was ±5%, the uncertainty of the mass flow controller (MKS 100) was of ±1%. The precision of the 234 SO_2 calibrations obtained during the ANTCI 2003 field campaign was 8%. Therefore the estimated uncertainty of the SO_2 measurement was ~9%. The HNO_3 permeation tube was calibrated by bubbling a sample into water and comparing it to an ion chromatograph. The uncertainty associated with the ion chromatographic nitrate measurement was ±10%, the uncertainty of mass flow controller was ±1%, and the precision of the three HNO_3 samples was 5%. The precision of the 242 HNO_3 field calibrations was 20%. The estimated uncertainty of the HNO_3 measurement was ~24%. The uncertainty of the HO_2NO_2 measurements depends on the NO_2 standard (2%) and SO_2 measurement (9%) and the ratio of sensitivity of SO_2 (mass102) to HO_2NO_2 (mass98) that was obtained after the mission. A 20% uncertainty for HO_2NO_2/SO_2 was obtained from comparison of the post mission pernitric calibrations collected after the ISCAT 2000 field campaign, the New England Air Quality Study (NEAQS), and ANTCI 2003. The uncertainty for the HO_2NO_2 measurement was ~31%.

The limit of detection (LOD) for sulfur dioxide and nitric acid were calculated from three standard deviations of the 90 second background signal. The LOD for both SO_2 and HO_2NO_2 were both less than 1pptv for a 10 minute average. The LOD for nitric acid was 13 pptv for a 10 minute average and was derived from the variance of the HNO_3 backgrounds.

2.4 Photochemical Model

Number densities of OH, HO_2, NO_2, and various RO_2 species (e.g. CH_3O_2) were calculated with a steady state box model that utilized explicit HO_x-NO_x-CH_4 chemistry (30 reactions) and was very similar to the model described in Chen et al. (2004). The model is recursive and was initialized with an estimate for each predicted species (i.e. OH, HO_2, CH_3O_2, NO_2, HO_2NO_2, CH_3OOH, CH_3OONO_2 and CH_3OH). The model ran until the values of all predicted species converged. This would require upwards of 1000 iterations. The model calculations were constrained by observations of a suite of chemical species such as HO_x precursors H_2O_2 and CH_2O, and photolysis rates obtained from the field campaigns. All model calculations were performed on a ten minute data merge. Further descripition of the model mechanism and the IGOR model code are provided in Appendix A.

There have been two subsequent modifications to the model. In order to compare the possible role of snowpack emission, formaldehyde, hydrogen peroxide and nitrous acid were calculated in addition to the other species from steady state. Later a seven reaction mechanism was added to predict the effect of bromine chemistry. The model was constrained to a (hypothetical) BrO measurement, and steady state concentrations of hypobromous acid (HOBr) and bromine radicals (Br) were calculated. A reaction mechanism for all species with reaction rates calculated at 250K and 680 mb has been provided. Median measured photolysis rates for local noon (10:00 A.M.-3:00 P.M. WGST) during the Summit 2003 field campaign and the early spring 2004 campaign (March 27th-April 10th) are also provided.

Table 2.5 Reaction Mechanism for steady state model

Reaction	Rate at 250 K and 680 mb
$O(^1D) + O_2 \rightarrow O(^3P) + O_2$	$k_1 = 4.2e^{-11} cm^3$ molecules^{-1} s^{-1}
$O(^1D) + N_2 \rightarrow O(^3P) + N_2$	$k_2 = 3.3e^{-11} cm^3$ molecules^{-1} s^{-1}
$O(^1D) + H_2O \rightarrow 2OH$	$k_3 = 2.2e^{-10} cm^3$ molecules^{-1} s^{-1}
$OH + CO + O_2 \rightarrow HO_2 + CO_2$	$k_4 = 2.1e^{-13} cm^3$ molecules^{-1} s^{-1}
$OH + CH_4 + O_2 \rightarrow CH_3O_2 + H_2O$	$k_5 = 2.0\ e^{-15} cm^3$ molecules^{-1} s^{-1}
$CH_3O_2 + NO + O_2 \rightarrow HO_2 + NO_2 + CH_2O$	$k_6 = 9.3e^{-12} cm^3$ molecules^{-1} s^{-1}
$CH_3O_2 + HO_2 \rightarrow CH_3OOH + O_2$	$k_7 = 8.2e^{-12} cm^3$ molecules^{-1} s^{-1}
$HO_2 + NO \rightarrow OH + NO_2$	$k_8 = 9.5e^{-12} cm^3$ molecules^{-1} s^{-1}
$OH + HO_2 \rightarrow H_2O + O_2$	$k_9 = 1.3e^{-10} cm^3$ molecules^{-1} s^{-1}
$HO_2 + HO_2 \rightarrow H_2O_2 + O_2$	$k_{10} = 5.1e^{-12} cm^3$ molecules^{-1} s^{-1}
$NO + O_3 \rightarrow NO_2 + O_2$	$k_{11} = 7.4e^{-15} cm^3$ molecules^{-1} s^{-1}
$OH + NO + M \rightarrow HONO + M$	$k_{12} = 8.5e^{-12} cm^3$ molecules^{-1} s^{-1}
$HO_2 + O_3 \rightarrow OH + 2O_2$	$k_{13} = 1.4e^{-15} cm^3$ molecules^{-1} s^{-1}
$OH + O_3 \rightarrow HO_2 + O_2$	$k_{14} = 4.0e^{-14} cm^3$ molecules^{-1} s^{-1}
$OH + HONO \rightarrow NO_2 + H_2O$	$k_{15} = 3.8e^{-12} cm^3$ molecules^{-1} s^{-1}
$OH + NO_2 + M \rightarrow HNO_3 + M$	$k_{16} = 1.2e^{-11} cm^3$ molecules^{-1} s^{-1}
$OH + HNO_3 + M \rightarrow NO_3 + H_2O + M$	$k_{17} = 2.8e^{-13} cm^3$ molecules^{-1} s^{-1}
$OH + OH + M \rightarrow H_2O_2 + M$	$k_{18} = 7.7e^{-12} cm^3$ molecules^{-1} s^{-1}
$OH + H_2O_2 \rightarrow HO_2 + H_2O$	$k_{19} = 1.5e^{-12} cm^3$ molecules^{-1} s^{-1}
$OH + CH_2O + O_2 \rightarrow HO_2 + CO + H_2O$	$k_{20} = 9.0e^{-12} cm^3$ molecules^{-1} s^{-1}
$HO_2 + NO_2 + M \rightarrow HO_2NO_2 + M$	$k_{21} = 1.5e^{-12} cm^3$ molecules^{-1} s^{-1}
$HO_2NO_2 + M \rightarrow HO_2 + NO_2 + M$	$k_{22} = 4.1e^{-5} cm^3$ molecules^{-1} s^{-1}
$OH + HO_2NO_2 \rightarrow NO_2 + H_2O + O_2$	$k_{23} = 5.9e^{-12} cm^3$ molecules^{-1} s^{-1}
$CH_3O_2 + CH_3O_2 \rightarrow CH_3OH + CH_2O + O_2$	$k_{24} = 3.4e^{-13} cm^3$ molecules^{-1} s^{-1}
$CH_3O_2 + CH_3O_2 + 2O_2 \rightarrow 2HO_2 + 2CH_2O + O_2$	$k_{25} = 1.1e^{-13} cm^3$ molecules^{-1} s^{-1}
$OH + CH_3OOH \rightarrow CH_3O_2 + H_2O$	$k_{26} = 5.9e^{-12} cm^3$ molecules^{-1} s^{-1}
$OH + CH_3OOH \rightarrow OH + CH_2O + H_2O$	$k_{27} = 2.5e^{-12} cm^3$ molecules^{-1} s^{-1}
$CH_3O_2 + NO_2 + M \rightarrow CH_3OONO_2 + M$	$k_{28} = 6.0e^{-12} cm^3$ molecules^{-1} s^{-1}
$CH_3OONO_2 + M \rightarrow CH_3O_2 + NO_2 + M$	$k_{29} = 1.6e^{-3} cm^3$ molecules^{-1} s^{-1}
$OH + CH_3OH + O_2 \rightarrow HO_2 + CH_2O + H_2O$	$k_{30} = 6.1e^{-13} cm^3$ molecules^{-1} s^{-1}
$Br + O_3 \rightarrow BrO + O_2$	$k_{31} = 6.9e^{-13} cm^3$ molecules^{-1} s^{-1}
$Br + CH_2O + O_2 \rightarrow HO_2 + CO + HBr$	$k_{32} = 6.9e^{-13} cm^3$ molecules^{-1} s^{-1}
$BrO + BrO \rightarrow 2Br + O_2$	$k_{33} = 3.8e^{-12} cm^3$ molecules^{-1} s^{-1}
$BrO + HO_2 \rightarrow HOBr + O_2$	$k_{34} = 2.9e^{-11} cm^3$ molecules^{-1} s^{-1}
$BrO + CH_3O_2 \rightarrow HOBr + CH_2O_2$	$k_{35} = 4.1e^{-12} cm^3$ molecules^{-1} s^{-1}
$BrO + CH_3O_2 + O_2 \rightarrow HO_2 + Br + CH_2O + O_2$	$k_{36} = 1.6e^{-12} cm^3$ molecules^{-1} s^{-1}
$BrO + NO \rightarrow Br + NO_2$	$k_{37} = 2.5e^{-11} cm^3$ molecules^{-1} s^{-1}

Table 2.6 Measured Photolysis rates at Summit Greenland

Reaction	Summer 2003	Early Spring 2004
$O_3 + h\nu \rightarrow O(^1D) + O_2$	$2.8e^{-5}$ s^{-1}	$4.0e^{-6}$ s^{-1}
$NO_2 + h\nu \rightarrow NO + NO_2$	$1.5e^{-2}$ s^{-1}	$8.3e^{-3}$ s^{-1}
$HONO + h\nu \rightarrow OH + NO$	$3.3e^{-3}$ s^{-1}	$1.8e^{-3}$ s^{-1}
$HNO_3 + h\nu \rightarrow OH + NO_2$	$7.0e^{-7}$ s^{-1}	$1.7e^{-7}$ s^{-1}
$HO_2NO_2 + h\nu \rightarrow HO_2 + NO_2$	$6.0e^{-6}$ s^{-1}	$1.6e^{-6}$ s^{-1}
$HO_2NO_2 + h\nu \rightarrow OH + NO_3$		
$CH_2O + h\nu \rightarrow H + HCO$	$4.6e^{-5}$ s^{-1}	$1.7e^{-5}$ s^{-1}
$CH_2O + h\nu \rightarrow H_2 + CO$	$6.9e^{-5}$ s^{-1}	$2.6e^{-5}$ s^{-1}
$CH_3OOH + h\nu \rightarrow OH + CH_3O$	$8.2e^{-6}$ s^{-1}	$1.2e^{-6}$ s^{-1}
$H_2O_2 + h\nu \rightarrow 2OH$	$9.6e^{-6}$ s^{-1}	$3.7e^{-6}$ s^{-1}

2.5 References

Cantrell, C. A., A. Zimmer, and G. S. Tyndall (1997), Absorption cross sections for water vapor from 183 to 193 nm, *Geophysical Research Letters*, *24*, 2195-2198.

Chen, G., D. Davis, J. Crawford, L. M. Hutterli, L. G. Huey, D. Slusher, L. Mauldin, F. Eisele, D. Tanner, J. Dibb, M. Buhr, J. McConnell, B. Lefer, R. Shetter, D. Blake, C. H. Song, K. Lombardi, and J. Arnoldy (2004), A reassessment of HO_x South Pole chemistry based on observations recorded during ISCAT 2000, *Atmospheric Environment*, *38*, 5451-5461.

Dubey, M. K., T. F. Hanisco, P. O. Wennberg, and J. G. Anderson (1996), Monitoring potential photochemical interference in laser-induced fluorescence measurements of atmospheric OH, *Geophysical Research Letters*, *23*, 3215-3218.

Edwards, G. D., C. A. Cantrell, S. Stephens, B. Hill, O. Goyea, R. E. Shetter, R. L. Mauldin, E. Kosciuch, D. J. Tanner, and F. L. Eisele (2003), Chemical ionization mass spectrometer instrument for the measurement of tropospheric HO_2 and RO_2, *Analytical Chemistry*, *75*, 5317-5327.

Eisele, F. L. (1986), Identification of Tropospheric Ions, *Journal of Geophysical Research-Atmospheres*, *91*, 7897-7906.

Eisele, F. L. (1989), Natural and Anthropogenic Negative-Ions in the Troposphere, *Journal of Geophysical Research-Atmospheres*, *94*, 2183-2196.

Eisele, F. L. (1995), New Insight and Questions Resulting from Recent Ion-Assisted OH Measurements, *Journal of the Atmospheric Sciences*, *52*, 3337-3341.

Eisele, F. L., and J. D. Bradshaw (1993), The Elusive Hydroxyl Radical Measuring OH in the Atmosphere, *Analytical Chemistry*, *65*, A927-&.

Eisele, F. L., G. H. Mount, F. C. Fehsenfeld, J. Harder, E. Marovich, D. D. Parrish, J. Roberts, and M. Trainer (1994), Intercomparison of Tropospheric OH and Ancillary Trace Gas Measurements at Fritz Peak Observatory, Colorado, *Journal of Geophysical Research-Atmospheres*, *99*, 18605-18626.

Eisele, F. L., G. H. Mount, D. Tanner, A. Jefferson, R. Shetter, J. W. Harder, and E. J. Williams (1997), Understanding the production and interconversion of the hydroxyl radical during the Tropospheric OH Photochemistry Experiment, *Journal of Geophysical Research-Atmospheres*, *102*, 6457-6465.

Eisele, F. L., and D. J. Tanner (1991), Ion-Assisted Tropospheric OH Measurements, *Journal of Geophysical Research-Atmospheres*, *96*, 9295-9308.

Eisele, F. L., and D. J. Tanner (1993), Measurement of the Gas-Phase Concentration of H2So4 and Methane Sulfonic-Acid and Estimates of H_2SO_4 Production and Loss in the Atmosphere, *Journal of Geophysical Research-Atmospheres*, *98*, 9001-9010.

Eisele, F. L., D. J. Tanner, C. A. Cantrell, and J. G. Calvert (1996), Measurements and steady state calculations of OH concentrations at Mauna Loa observatory, *Journal of Geophysical Research-Atmospheres*, *101*, 14665-14679.

Fehsenfeld, F. C., C. J. Howard, and A. L. Schmeltekopf (1975), Gas-Phase Ion Chemistry of Hno3, *Journal of Chemical Physics*, *63*, 2835-2842.

Felton, C. C., J. C. Sheppard, and M. J. Campbell (1988), Measurements of the Diurnal OH Cycle by a C-14 Tracer Method, *Nature*, *335*, 53-55.

Huey, L. G., D. R. Hanson, and C. J. Howard (1995), Reactions of SF_6- and I- with Atmospheric Trace Gases, *Journal of Physical Chemistry*, *99*, 5001-5008.

Huey, L. G., D. J. Tanner, D. L. Slusher, J. E. Dibb, R. Arimoto, G. Chen, D. Davis, M. P. Buhr, J. B. Nowak, R. L. Mauldin, F. L. Eisele, and E. Kosciuch (2004), CIMS measurements of HNO_3 and SO_2 at the South Pole during ISCAT 2000, *Atmospheric Environment*, *38*, 5411-5421.

Kenley, R. A., P. L. Trevor, and B. Y. Lan (1981), Preparation and Thermal-Decomposition of Pernitric Acid ($HOONO_2$) in Aqueous-Media, *Journal of the American Chemical Society*, *103*, 2203-2206.

Lovejoy, E. R., D. R. Hanson, and L. G. Huey (1996), Kinetics and products of the gas-phase reaction of SO_3 with water, *Journal of Physical Chemistry*, *100*, 19911-19916.

Mather, J. H., P. S. Stevens, and W. H. Brune (1997), OH and HO_2 measurements using laser-induced fluorescence, *Journal of Geophysical Research-Atmospheres*, *102*, 6427-6436.

Simmonds, P. G., D. M. Cunnold, F. N. Alyea, C. A. Cardelino, A. J. Crawford, R. G. Prinn, P. J. Fraser, R. A. Rasmussen, and R. D. Rosen (1988), Carbon-Tetrachloride Lifetimes and Emissions Determined from Daily Global Measurements during 1978-1985, *Journal of Atmospheric Chemistry*, *7*, 35-58.

Slusher, D. L., L. G. Huey, D. J. Tanner, G. Chen, D. D. Davis, M. Buhr, J. B. Nowak, F. L. Eisele, E. Kosciuch, R. L. Mauldin, B. L. Lefer, R. E. Shetter, and J. E. Dibb (2002), Measurements of pernitric acid at the South Pole during ISCAT 2000, *Geophysical Research Letters*, *29*, -.

Slusher, D. L., S. J. Pitteri, B. J. Haman, D. J. Tanner, and L. G. Huey (2001), A chemical ionization technique for measurement of pernitric acid in the upper troposphere and the polar boundary layer, *Geophysical Research Letters*, *28*, 3875-3878.

Tanner, D. J., and F. L. Eisele (1995), Present OH Measurement Limits and Associated Uncertainties, *Journal of Geophysical Research-Atmospheres*, *100*, 2883-2892.

Tanner, D. J., A. Jefferson, and F. L. Eisele (1997), Selected ion chemical ionization mass spectrometric measurement of OH, *Journal of Geophysical Research-Atmospheres*, *102*, 6415-6425.

Viggiano, A. A., R. A. Perry, D. L. Albritton, E. E. Ferguson, and F. C. Fehsenfeld (1982), Stratospheric Negative-Ion Reaction-Rates with H_2SO_4, *Journal of Geophysical Research-Oceans and Atmospheres*, *87*, 7340-7342.

CHAPTER 3

PEROXY AND HYDROXYL RADICAL MEASUREMENTS OBTAINED FROM THE SUMMER 2003 FIELD CAMPAIGN AT SUMMIT, GREENLAND

3.1 Introduction

The first measurements of peroxy (HO_2+RO_2) and hydroxyl (OH) radicals above the arctic snowpack were collected during the summer 2003 campaign at Summit, Greenland. The median measured number densities for peroxy and hydroxyl radicals were $2.2x10^8$ molecules cm^{-3} and $6.4x10^6$ molecules cm^{-3} respectively. The observed peroxy radical values were in excellent agreement ($R^2 = 0.83$, M/O = 1.06) with highly constrained model predictions. However, calculated hydroxyl number densities were consistently more than a factor of two lower than the observed values These results indicate that our current understanding of radical sources and sinks is in accord with our observations in this environment but that there may be a mechanism that is perturbing the (HO_2+RO_2)/OH ratio. This observed ratio was also found to depend on meteorological conditions especially during periods of high winds accompanied by blowing snow. Figure 1 presents a time series of measurements and model predictions of both peroxy and hydroxyl radicals along with wind speeds. Backward transport model simulations indicate that these periods of high winds were characterized by rapid transport (1-2 days)

of marine boundary air layer to Summit. This and other data suggests that the boundary layer photochemistry at Summit may be periodically impacted by halogens.

3.2 Methods

Hydroxyl and peroxy radical measurements at Summit were obtained with a CIMS set on the snow pack in a heated enclosure. Measured concentrations were compared to a highly constrained 0-D steady state photochemical model. Both the instrument and the model are explained in detail in Chapter 2. Two model runs were used to determine the effect of HONO on radical concentrations. The first model run was constrained to the full suite of measured species which included j-values, O_3, CO, CH_4, H_2O, NO, CH_2O, H_2O_2, and HONO. The second run was constrained to the same suite of measurements with the exception of HONO. HONO was calculated by assuming it was in steady state.

1. $OH + NO + M \rightarrow HONO + M$
2. $HONO + h\nu \rightarrow OH + NO$
3. $OH + HONO \rightarrow H_2O + NO_2$

Since the photolytic lifetime of HONO is short ($\tau_{HONO} \approx 10$min) the steady state assumption is reasonable. The steady state concentration of HONO is obtained from reactions 1-3.

$$[HONO]_{SS} = \frac{k_1[OH][NO]}{j_2 + k_3[OH]}$$

All model calculations were performed on a ten minute data merge. Two filters were applied to the data to remove invalid or questionable data points. The first was for enhanced NO concentrations (>100ppt) due to the station generator impacting the

measurement site. The pollution (high NO_x) events were often accompanied by light winds from the north to northeast (an auxiliary filter). The second filter was for wind speeds above 6 m s^{-1}. It was applied since higher wind speeds were found to increase the uncertainty in the instrument calibration as well as to decrease the sensitivity of the instrument. In addition, the high wind filter also allowed us to separate out the periods of blowing snow which exhibited HO_x chemistry that was very different than observed during calm periods (see below).

3.2.1 Additional Measurements

Measurements of NO, ozone, water vapor, HONO, HNO_3, H_2O_2, CH_2O and actinic flux were all obtained within five meters of the CIMS instrument. Water vapor and ozone concentrations were measured with commercial instruments (Vaisala HMM 211 and Thermo Environmental Model 49). NO mixing ratios were obtained from a chemiluminescence detector nearly identical to that described by *Ryerson et al.* [2000]. Photodissociation rates were calculated from data gathered from a Scanning Actinic Flux Spectroradiometer [*Shetter and Müller,* 1999]. Nitrous and nitric acid were sampled by a mist chamber coupled with an ion chromatograph as described by *Dibb et al.* [1998]. Hydrogen peroxide and formaldehyde were quantitatively scrubbed from the air into a water stream and then fluorometrically detected in the liquid phase [*Hutterli et. al,* 2004]. Volatile organic compounds including carbon monoxide and methane were measured in whole air samples collected at Summit in steel canisters pressurized with a metal bellows pump [*Swanson et al.* 2002].

3.2.2 FLEXPART model

The Lagrangian particle dispersion model FLEXPART was used to determine the source region of air impacting Summit. FLEXPART is a particle dispersion model with full turbulence and convection parameterizations [*Stohl et al.,* 2005] and for this study was run backward in time from the Summit site. The theory underlying the backward calculations is presented by *Seibert and Frank* [2004], and applications to aircraft measurements were presented by *Stohl et al.,* [2003]. Backward simulations are presented for the high wind event (June 28) and representative low wind day (July 9). The model output consists of mapped emission sensitivities, which are proportional to residence times of the particles and, for the purpose of this study, can be interpreted in a similar way as simple back trajectory calculations.

3.3 Peroxy Radicals (HO_2+RO_2)

The median measured HO_2+RO_2 number density for the entire mission was $2.2x10^8$ molecules cm^{-3} (mean $2.4x10^8$ molecules cm^{-3}). During the observation period with concurrent HONO measurements the median number density for HO_2+RO_2 was $3.4x10^8$ molecules cm^{-3}. The HONO measurement coverage excludes ~25% of the HO_x measurements, usually between 22:00 P.M.-8:00 A.M. West Greenland Summer Time (WGST = UTC-2 hrs). Median noontime, 10:00 A.M-3:00 P.M.WGST, values for peroxy radicals were $4.1x10^8$molecules cm^{-3}. A comparison of measured and modeled (without HONO) peroxy radical number densities is presented in Figure 3.1. These data have been filtered for station pollution but not for high winds. Wind speed has also been

included to demonstrate the correlation between high winds and the periods of greatest divergence between the measured and modeled values.

Two model runs were compared to observations (Figure 3.2). In the first run the model was constrained to all measured precursors (solid black diamonds) and in the second run measured HONO was excluded from the model (open green diamonds). Model predictions for HO_2+RO_2 were in excellent agreement ($R^2 = 0.83$ see Figure 3.2) with observed peroxy values when constrained to H_2O_2 and CH_2O observations and for wind velocities less than 6 m/s. Even when the high wind speed peroxy measurements were included the correlation was still robust ($R^2 = 0.75$). The median ratio of modeled to observed (M/O) for peroxy radicals was 1.06 for the filtered data set. When HONO was added as a constraint to the model the M/O ratio increases by ~20% for peroxy radicals.

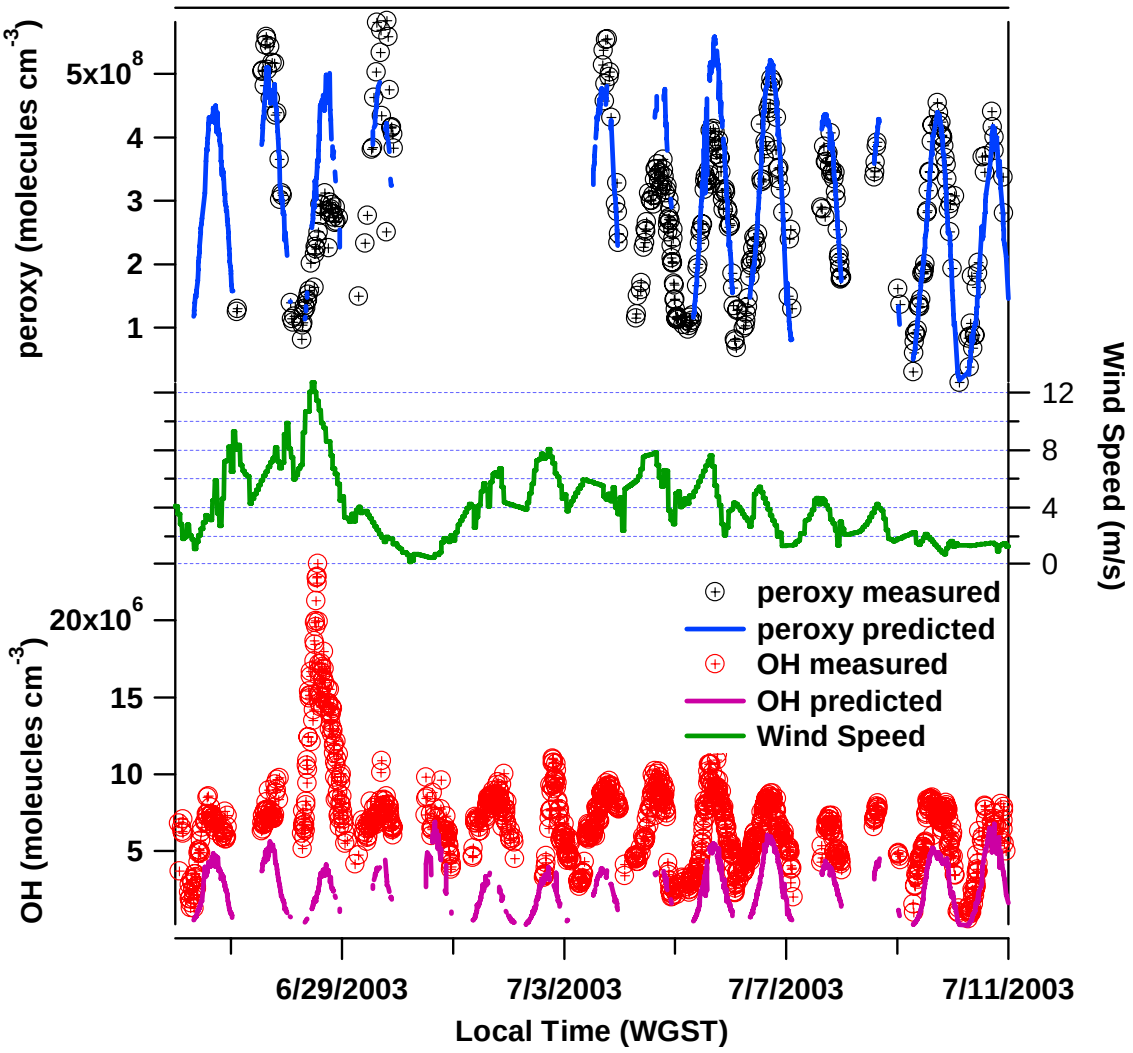

Figure 3.1 Time series of hydroxyl and peroxy radical measurements and wind speed. The black circles and the solid blue line represent measured and modeled peroxy concentrations. The red circles and solid purple line represent measured and modeled hydroxyl concentrations. The green line indicates wind speed. Note that the gap in peroxy radical measurement was due to removal of the NO addition. This was done to make sure that a possible NO leak in the sample tube did not lead to high measurements of hydroxyl radicals.

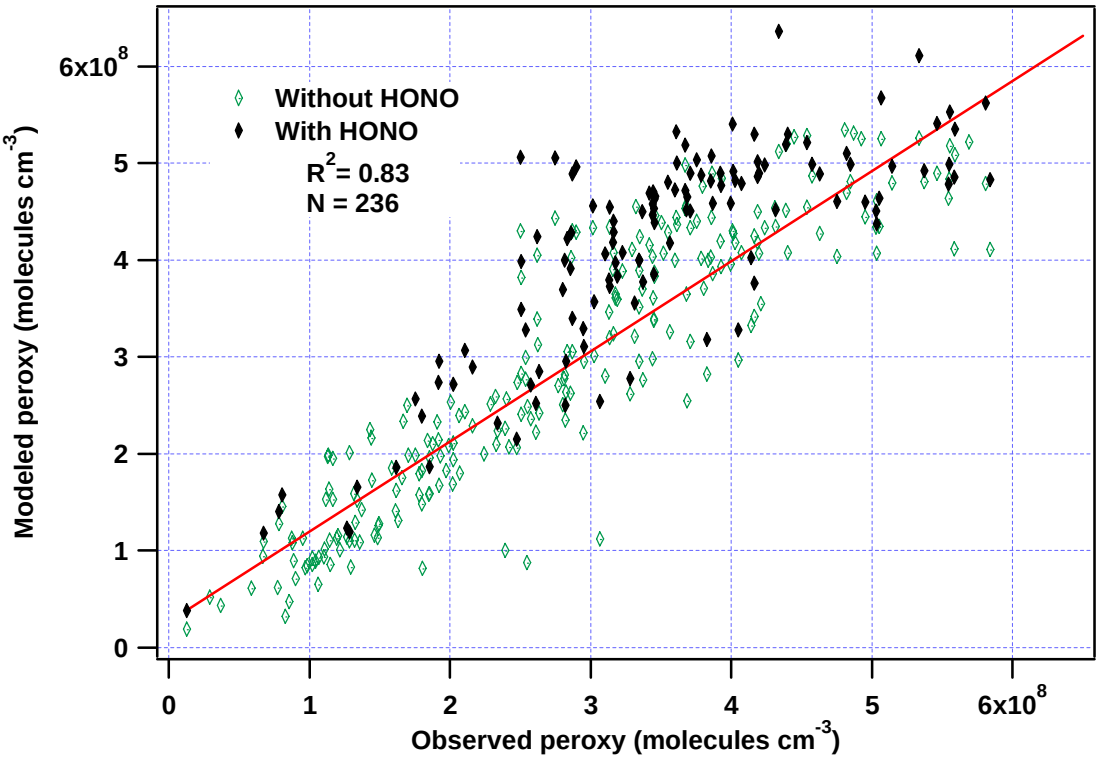

Figure 3.2 Scatter plot of predicted vs. measured $HO_2 + RO_2$ radicals. Model results without HONO are represented by open green diamonds and results with HONO are indicated by solid black diamonds. The linear regression is fit to model results without HONO.

Finally the observations and model prediction (with HONO) for the entire field campaign were averaged into a composite 24-hour 'day' with 10 minute time resolution, shown in figure 3.3. The correlation between the binned observations and the model was excellent (R^2 of 0.88) with a median M/O of 1.16. Slightly better results were obtained when comparing the binned data not constrained to observed HONO with a median M/O of 1.01.

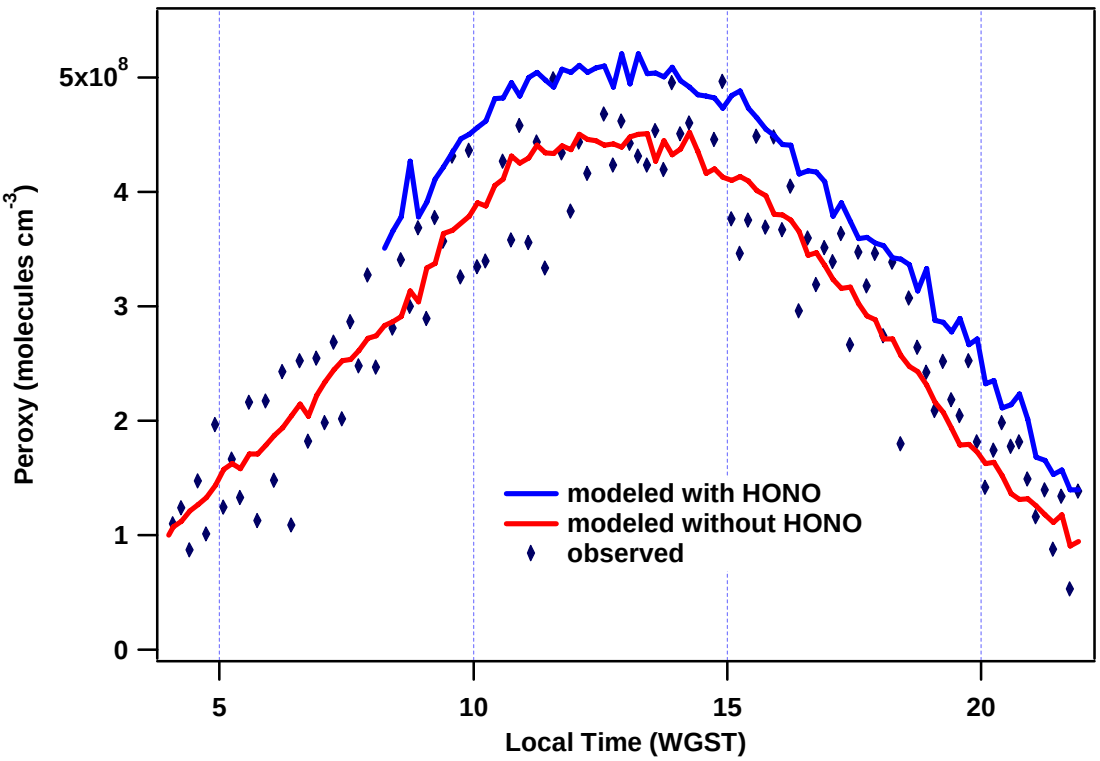

Figure 3.3 Composite 24 hr measurements and model predictions of peroxy radicals. Model predictions constrained by measured H_2O_2, CH_2O and HONO are represented by the blue line. The red line is the same model but not constrained to measured HONO.

3.4 Hydroxyl Radicals (OH)

The median observed OH number density was 6.4×10^6 molecules cm^{-3} (mean 6.3×10^6 molecules cm^{-3}) for the entire mission. The median OH during periods of concurrent HONO measurements was 7.7×10^6 molecules cm^{-3} and the noontime median OH concentration was 8.4×10^6 molecules cm^{-3}. The agreement between OH measurements and model predictions was not as good as for the peroxy radicals. Measured values were typically a factor of 2-3 higher than the predicted values. The discrepancy between the model and measured values was found to depend strongly on meteorology. This was depicted in the time series presented in figure 3.1. During the periods of high wind and blowing snow (>6 m s^{-1}) highly elevated concentrations of OH were routinely observed (see below and Figure 3.1). However, during clear periods with

light winds model predictions and observations were in better agreement. The longest such period was between July 8 and July 11. During this time a reasonable correlation ($R^2 = 0.47$) and median M/O (0.65) were found when the model was constrained by HONO (Figure 3.4). When the model was not constrained by HONO the correlation was improved ($R^2 = 0.77$) while the median M/O dropped to 0.48. However, much of the improvement in the correlation can be attributed to greater data coverage when the comparison was not limited to the HONO data set.

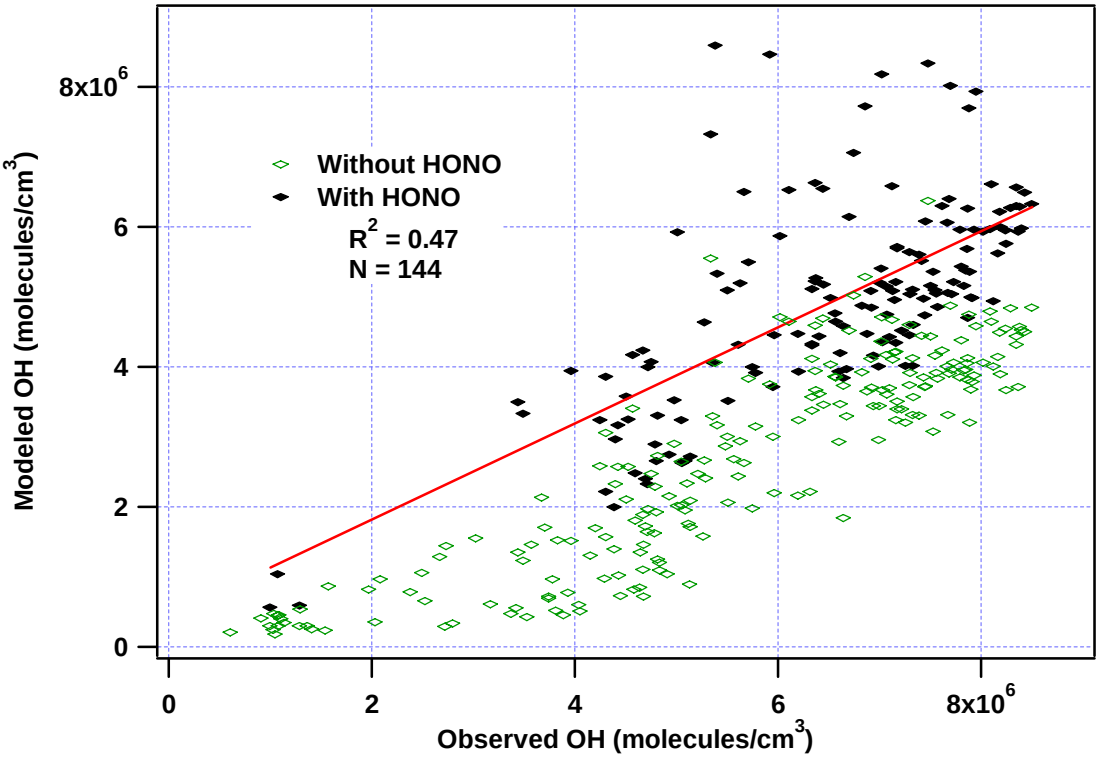

Figure 3.4 Scatter plot of predicted versus measured OH radicals for the last four days of the field campaign (7/8-7/11 2003). Model results without HONO are represented by open green diamonds and results with HONO are indicated by solid black diamonds. The linear regression is fit to model results with HONO.

The correlation between the low wind speed, binned 10 minute modeled, and measured OH was strong (R^2 of 0.83, Figure 3.5). However, even with this extensive data selection the model still under predicted the OH concentration by a factor of two when constrained to HONO. This indicated that the predicted ratio of peroxy radicals to hydroxyl radicals ((HO_2+RO_2)/OH) was too high. The median predicted (HO_2+RO_2)/OH for the low wind data was 115:1 and was essentially independent of HONO. In contrast the median measured (HO_2+RO_2)/OH was 45:1.

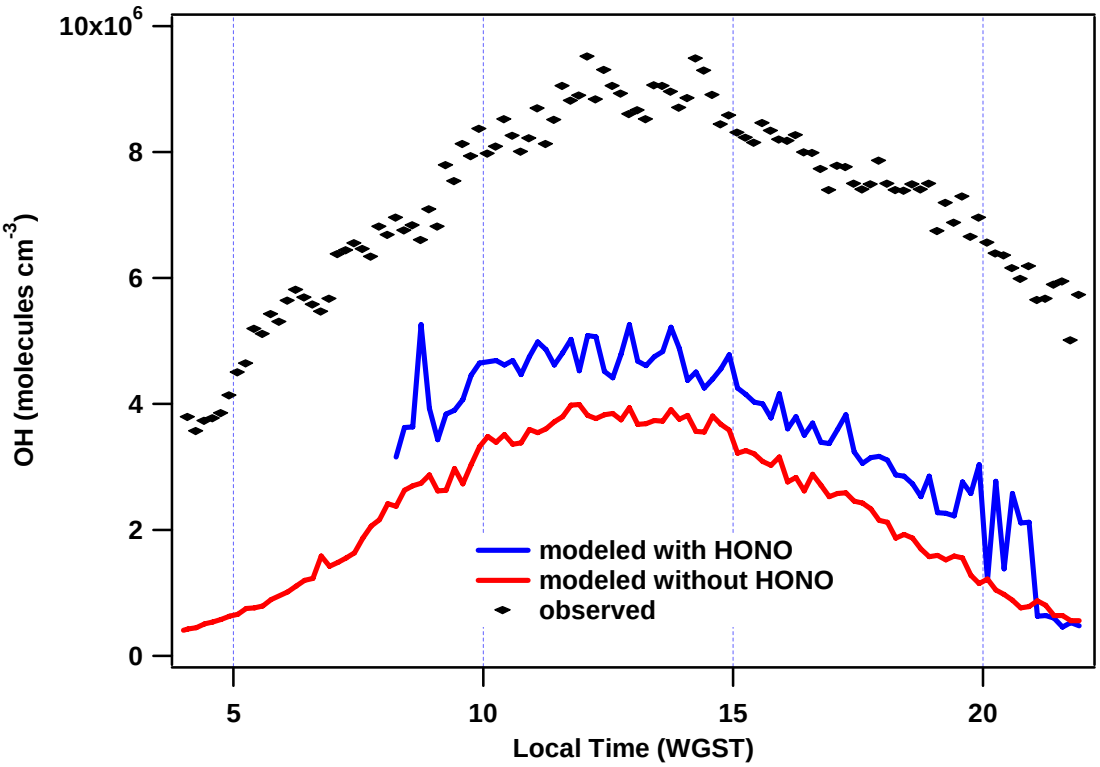

Figure 3.5 Composite 24 hour measurements and model predictions of hydroxyl radicals. Model predictions constrained by measured H_2O_2, CH_2O, and HONO are represented by the blue line. The red line is the same model but not constrained to measured HONO.

3.5 Case Studies-High and Low Wind

As mentioned previously, meteorological conditions appear to play a role in the radical concentrations. For this reason, data from July 9 and June 28 were shown in more detail to illustrate data from meteorological extremes. July 9 (Figure 3.6) was a clear day with light winds (mean = 1.6m s^{-1}) and an average temperature of -17.6°C. The median number density for OH was $5.6x10^6$ molecules cm^{-3} and $2.5x10^8$molecules cm^{-3} for HO_2+RO_2 with a corresponding (HO_2+RO_2)/OH ratio of 45:1.

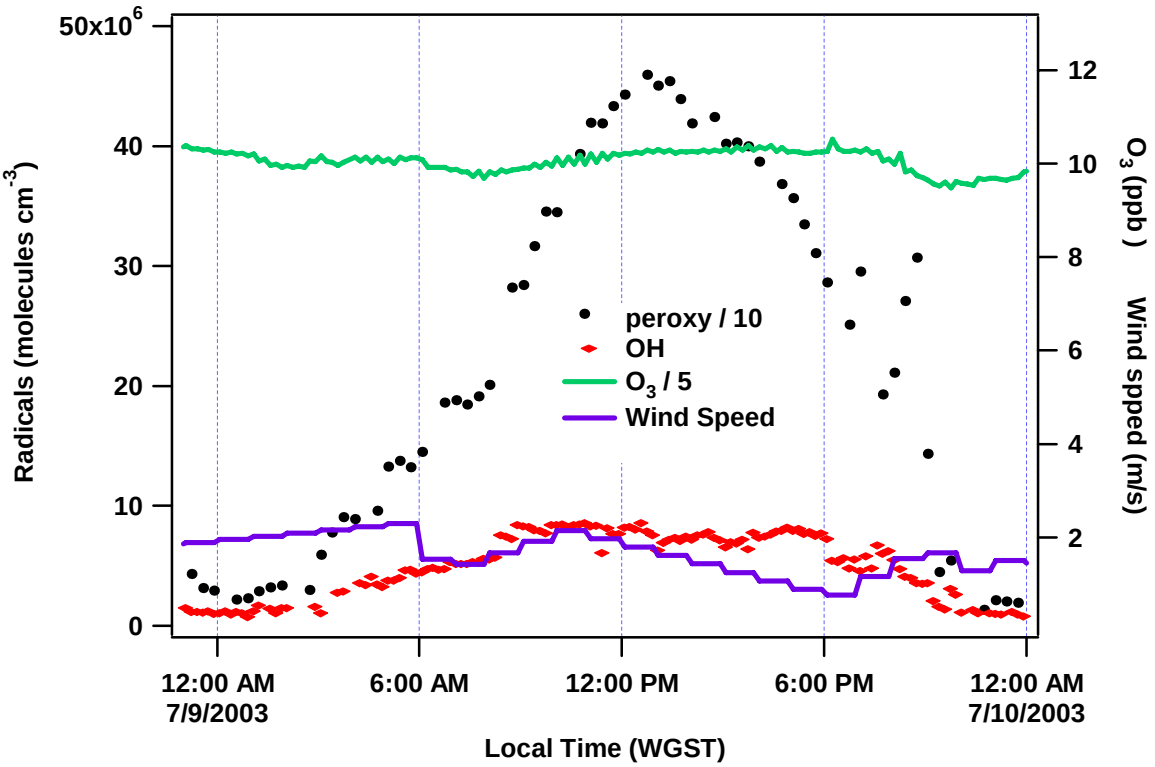

Figure 3.6 Measured values for radicals, ozone and wind speed on July 9. Black Dots = peroxy radicals (number density/10), Red Diamonds = OH (number density), Green Line = Ozone (ppbv/5) and Blue Line = wind speed (m s^{-1}).

At midday (10:00 A.M.-3:00 P.M. WGST) OH production was 3.8×10^6 molecules cm^{-3} s^{-1} and HO_x production was 2.0×10^6 molecules cm^{-3} s^{-1}. OH production was a factor of two larger than HO_x production because the cycling of HO_2 to OH by NO was calculated to be the dominant source of hydroxyl radicals on this date. The mean midday NO mixing ratio was 28 pptv and the predicted (HO_2+RO_2)/OH ratio was 83:1. Observed midday OH and HO_2+RO_2 number densities were 7.7×10^6 molecules cm^{-3} and 4.3×10^8 molecules cm^{-3} respectively, which led to a (HO_2+RO_2)/OH ratio of 56:1. Ozone remained fairly constant (50 ppb) throughout the measurement period dropping down to a minimum of 47.5 ppb late in the day. Backward simulations derived from the FLEXPART model (Figure 3.7) indicate that the majority of the air sampled at Summit had been lingering over the Greenland ice sheet for several days and was mainly from high altitudes with little time spent in the boundary layer.

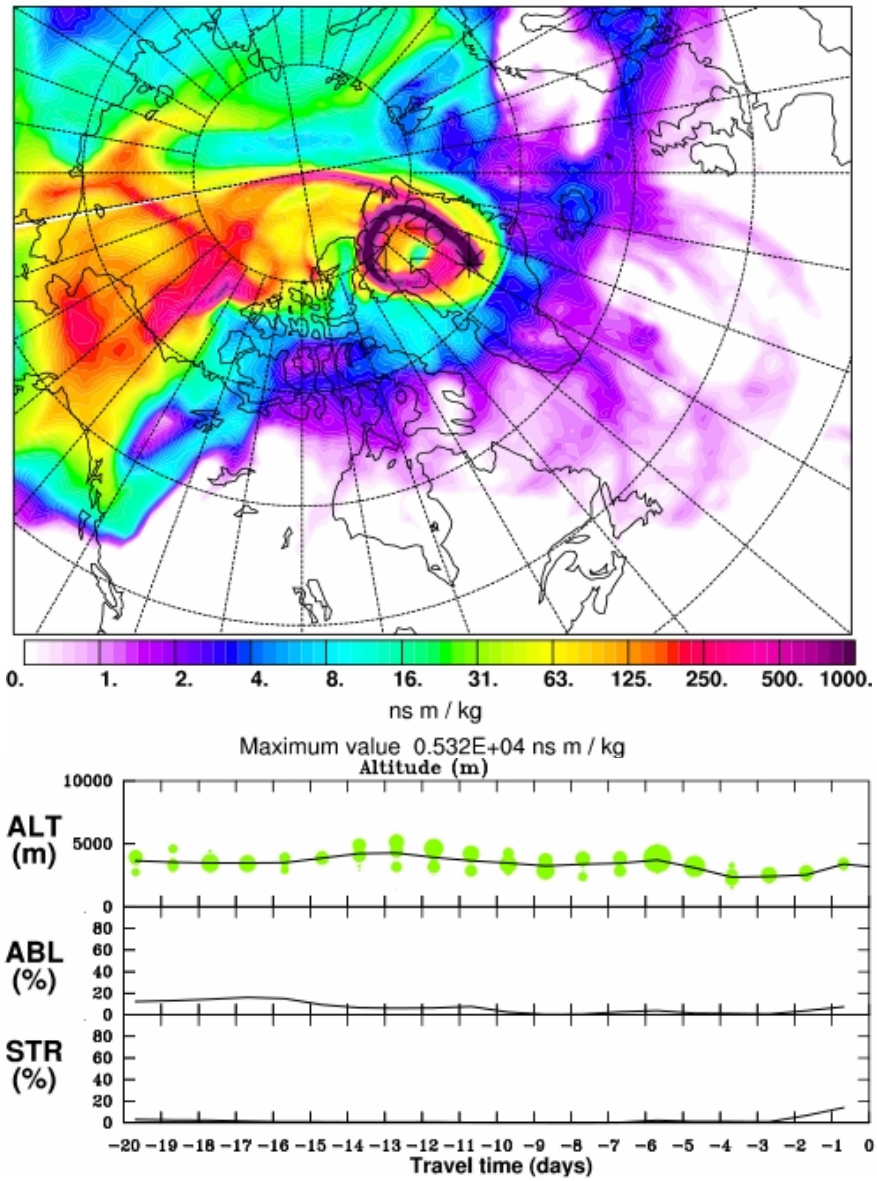

Figure 3.7. FLEXPART 20-day model back projection for July 9. The emission sensitivity integrated over the entire atmospheric column (at top) indicates that the majority of the air sampled at Summit was from the surrounding Geenland Ice cap. The altitude profile reinforces this conclusion and indicates that the air spent little time in the boundary layer. This was confirmed by low values of the emission sensitivity for the lowest 100m of the atmosphere (not shown).

In contrast June 28 (Figure 3.8) was a warm day, average temperature -12.4°C, with strong advection from the south accompanied by heavy blowing/falling snow. Visibility was frequently less than 10 meters. The median OH concentration was $1.1x10^7$molecules cm^{-3}, the highest daily average for the mission, while the peroxy number density was a relatively modest $2.1x10^8$ molecules cm^{-3}. The daily $(HO_2+RO_2)/OH$ ratio was 19:1. By comparison the midday OH and HO_x rates of production were $2.8x10^6$ and $2.1x10^6$ molecules cm^{-3} s^{-1} respectively. The NO midday mixing ratio was 9 pptv.

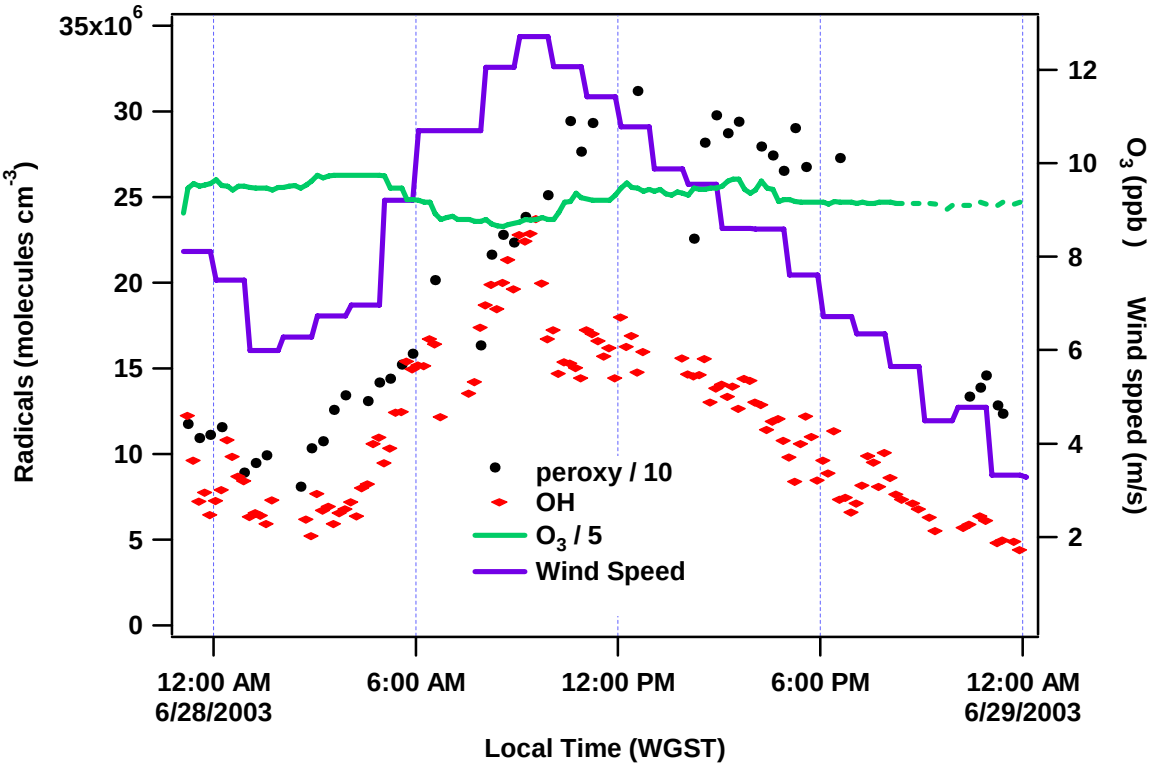

Figure 3.8 Measured values for radicals, ozone and wind speed on June 28. Black Dots = peroxy radicals (number density/10), Red Diamonds = OH (number density), Green Line = Ozone (ppbv/5) and Blue Line = wind speed (m s^{-1})

The predicted midday (HO_2+RO_2)/OH ratio was 128:1, a factor of seven greater than the observed ratio. The period between 8:00-10:00 A.M. further illustrates this point. During this period the wind speed achieved an hourly averaged maximum of 12 m s^{-1}, the highest observed over the campaign, and was accompanied by the daytime minimum mixing ratio of ozone (44 ppbv). The measured OH number densities climbed to $2.0x10^7$molecules cm^{-3} during this event and the ratio of (HO_2+RO_2)/OH dropped to 10:1. The modeled (HO_2+RO_2)/OH during the high wind event was 143:1, a 14 fold increase over the observed ratio. In addition the largest disagreement between modeled and observed HO_2+RO_2 was observed during this time. The FLEXPART backwards simulations (Figure 3.9) show that the air sampled at Summit on June 28 was influenced by a low pressure system in the Irminger Sea. Retroplume analysis indicates that the majority of the Summit air mass had been located over the ocean recently (1-2 days) with a large component from the boundary layer. The data suggests that, during these extreme conditions, there was either a positive experimental artifact in the OH or there was unidentified chemistry that significantly perturbed the (HO_2+RO_2)/OH ratio associated with blowing snow or marine air masses.

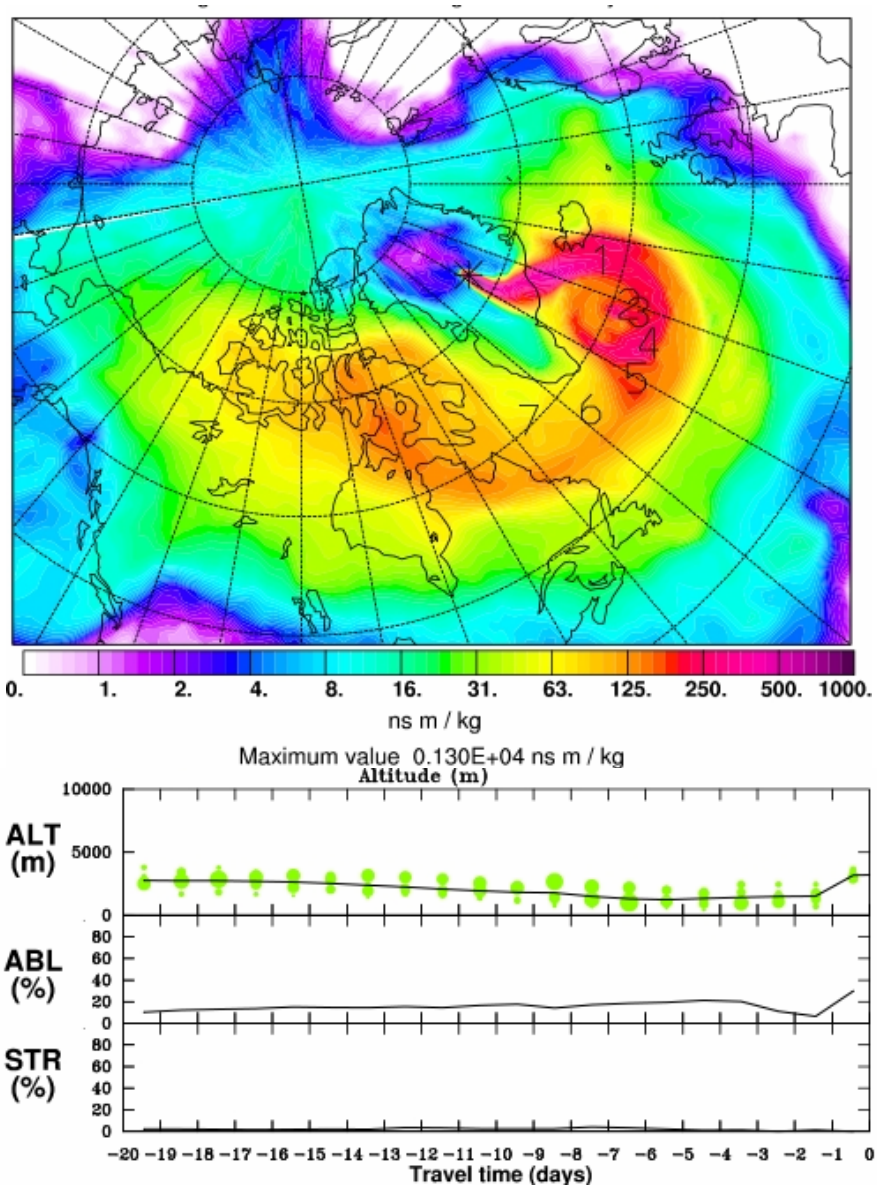

Figure 3.9 FLEXPART model 20-day back projection for June 28. The emission sensitivity integrated over the entire atmospheric (at top) indicates that there was a strong flow of marine air to Summit from a low pressure system in the North Atlantic. Numbers mark the average position of the air mass at daily intervals back in time and show that the air was already south of Iceland the previous day. A marine boundary layer origin is also suggested by the low average altitude of the tracked particles (lower panel) and the significant percentage of boundary layer air. Plots of the emission sensitivity for the lowest 100m of the atmosphere (not shown) also reveal high values over the North Atlantic Ocean.

3.6 Discussion

The excellent agreement between measured and modeled peroxy radical number densities suggests that HO_x sources and sinks at Summit were relatively well understood. On average the largest source in the HO_x budget was photolysis of O_3 (~40%), followed by the photolysis of H_2O_2 (~30%), photolysis of HONO (~22%) and photolysis of CH_2O (~8%) when the model was constrained by HONO. When the model was not constrained to HONO it lowered the predicted values for peroxy and hydroxyl radicals by ~20%, which was similar in magnitude to uncertainty of photolysis rate of HONO [*Stutz et al.,* 2000]. By comparison the South Pole model runs constrained with observed HONO values were entirely inconsistent with measured OH values. This led to speculation by *Chen et al.,* [2004] that the HONO mist chamber values might be due to some interfering species. The lower impact of HONO at Summit relative to the South Pole was a function of both lower mixing ratios, South Pole median = 33 ppt [*Dibb et al.,* 2004], Summit median = 10 ppt [*Dibb*, in press], and higher radical production from ozone and hydrogen peroxide. Consequently, the Summit 2003 data did not provide a good test of the validity of measured HONO values. However, the data clearly indicate that HONO was not the dominant HO_x source at Summit in the summer of 2003.

Inclusion of HONO does improve the modeled to observed ratio for OH. Over the entire mission (without filter for high wind) the median M/O increased from 0.39 to 0.45 when the model was constrained to HONO. The improvement was even more dramatic during the last four days of the mission, an extended period of calm winds and clear skies, when the median M/O improved from 0.47 to 0.65 with HONO. This ~35%

underestimation "best case" scenario was on the order of the uncertainty in the measurement. However, the inclusion of HONO does not improve the agreement between the predicted and measured ratio of $(HO_2+RO_2)/OH$. In addition during periods of highest winds (>10m s^{-1}) the measured values of OH were an order of magnitude larger than the predicted. An experimental artifact in high winds and blowing snow would provide a simple explanation to this observation. However, characterization of the instrument indicates that the instrument only loses sensitivity to OH during periods of high crosswinds.

The measured OH values compare reasonably well with the predicted noontime values of OH in *Yang et al.,* [2002], but the measured peroxy values were a factor of two less than their predicted values. It should be noted that the measurements and their model predictions were for two different years and the models used in the present work were constrained by a greater suite of measured values. For this reason, we performed model calculations constrained to 1999 values for the input parameters (H_2O, NO, O_3, HONO, CH_2O, H_2O_2, CO, CH_4, j-values) used in the Yang model. We calculate an OH number density of $4.7x10^6$molecules cm^{-3} and a peroxy radical number density of $4.4x10^8$ molecules cm^{-3}. Both are roughly a factor of two less than the values predicted by *Yang et al.* [2002]. There are also differences in the relative magnitude of HO_x sources between the two models. This disagreement between the two models does vary to some extent with the value of the parameter α ($\alpha = [HO_2]/[HO_2]+[CH_3O_2]$) that was used to constrain the Yang model. The model used in this work did not use this parameter but instead explicitly calculated peroxy radical concentrations from the mechanism. This

difference between the calculations was a likely source of the discrepancy between the results.

Since measured peroxy radical levels were well reproduced by model calculations, ozone production rates ($PO_3 = k_1[RO_2][NO]+k_2[HO_2][NO]$) should be accurately predicted. During the 2003 Summit field campaign average production rates of ~0.8 ppbv/day were calculated for the boundary layer, which was about 2% of the daily average ozone mixing ratio. However, at Summit surface layer photochemical production did not appear to influence ozone levels [*Helmig et al.,* in press]. In fact the boundary layer at Summit appeared to be slightly depleted in ozone as balloon profiles frequently show higher mixing ratios above the boundary layer [*Helmig et al.,* 2002]. In addition firn air measurements of ozone at Summit were lower than ambient, often by a factor of two or more [*Peterson and Honrath,* 2001]. The difference between ambient and firn measurements was greatest during the day implying photochemical loss in the interstitial air [*Peterson and Honrath,* 2001].

These observations were not in accord with those at the South Pole, where an average boundary layer production of ~2 ppbv day^{-1} was predicted [*Chen et al.,* 2004] The South Pole ozone record displays photochemical production during early summer that is superimposed on the summer minimum in average ozone levels [*Crawford et al.,* 2001]. Balloon measurements of ozone at the South Pole also show an enhancement of ozone in the boundary layer [*Helmig et al*. in press], and destruction in the firn air is of lesser magnitude than what was observed at Summit. Data from ISCAT 2000 indicates a depletion of ~20% in the firn [*Davis et al.,* unpublished results].

We speculate that the lack of observed ozone production at Summit and the perturbed (HO_2+RO_2)/OH ratio might be explained by a similar chemical mechanism. The presence of halogen radicals could help explain both the slight depletion of boundary layer ozone and the enhancement in OH [*Foster et al.,* 2001; *von Glasow et al.,* 2004; *Stutz et al.,* 1999]. At coastal Arctic sites increases in bromine oxide (BrO) have been well documented during ozone depletion events [*Barrie et al.,* 1988, *Hausmann and Platt,* 1994, *Hönninger and Platt*, 2002]. It is also possible that this chemistry could be altered by heterogeneous processes due to increased surface area (blowing snow) in the high wind events. Alternatively, rapid transport of air from the marine boundary layer (as suggested by FLEXPART backwards simulations) to Summit might be another mechanism for activating halogen chemistry.

The connection between HO_x chemistry and halogen oxides has been recently investigated in coastal environments. Measurements of HO_x, BrO and IO were obtained at Mace Head, Ireland, during the NAMBLEX field campaign [*Bloss et al.,* 2005, *Smith et al.,* 2006, *Sommarvia et al.,* 2006]. Daily maximum mixing ratios of IO were between 0.8-4.0 pptv [*Bloss et al.,* 2005] and BrO levels were measured up to 6.5 pptv [*Saiz-Lopex et al.,* 2004]. In this coastal environment photolysis of HOI was calculated to be responsible for 15% OH production and photolysis of HOBr was estimated to be of similar magnitude. These results demonstrate that halogens could significantly impact the HO_2+RO_2 to OH ratio through photolysis of HOI and/or HOBr.

Although there are no measurements of BrO or IO at Summit there exists ancillary evidence that suggests that both species may be present. Low concentrations (1-2 pptv) of soluble gas phase bromide were detected by the UNH mist chamber during the

summer 2003 mission. However, on June 28th soluble gas phase bromide was above 8 pptv from the onset of measurement (10:00 A.M. WGST) until 2:30 P.M. WGST and reached a maximum of 11 pptv during this period. Halocarbons such as methyl bromide, ethyl bromide, methyl iodide, and ethyl iodide have been observed in the atmosphere at Summit [*Swanson et al.,* 2002]. The observed concentrations of all four were enhanced in the firn column indicating active photochemistry involving halogen radicals within the snowpack [*A. Swanson,* private communication]. Annual changes of iso-butane/propane ratios in the firn column at Summit also suggest a seasonal variance of bromine radicals.

In order to see how much bromine would be required to bring the model predictions into agreement with our measurements the following bromine reaction scheme was added to the model chemistry.

4. $Br + O_3 \rightarrow BrO + O_2$

5. $Br + CH_2O + O_2 \rightarrow HBr + CO + HO_2$

6. $BrO + HO_2 \rightarrow HOBr + O_2$

7. $BrO + BrO \rightarrow 2Br + O_2$

8. $BrO + CH_3O_2 \rightarrow HOBr + CH_2O_2$

9. $BrO + CH_3O_2 + O_2 \rightarrow Br + CH_2O + HO_2 + O_2$

10. $BrO + NO \rightarrow Br + NO_2$

11. $HOBr + h\nu \rightarrow OH + Br$

12. $BrO + h\nu \rightarrow Br + O$

Two model runs with 5ppt and 10ppt of BrO were performed with and without HONO as a model constraint and are presented in Table 1. The modeled to observed ratio for OH improved to 0.68 with inclusion of 5 pptv of BrO and 0.83 with 10 pptv of BrO with the

model constrained to HONO. Both values are within the measurement uncertainty for the CIMS. IO could also have a similar effect on the peroxy to OH radical ratio but at lower concentrations (~1-3ppt) due to a four fold increase in the reaction rate with HO_2. Both calm and windy periods were also examined to see how much BrO was required to bring modeled and observed values into agreement. When 5 ppt of BrO is added to the final four days of the measurement period the M/O for OH increased to 0.95. By comparison ~135 ppt of BrO was needed to predict the $2.1x10^7$molecules/cm^3 of OH observed during the high wind event (8.00-10 P.M.) on June 28. The high BrO introduced into the model also leads to a predicted HO_2+RO_2/OH of 14:1 and an ozone destruction rate of ~8ppb/hr during the two hour wind maximum.

Table 3.1 Median noontime (10:00 A.M.- 3:00 P.M.) model predictions for radicals (molecules/cm^3) and modeled to observed ratios with BrO chemistry

Model Input	HO_2+RO_2	OH	M/O HO_2+RO_2	M/O OH
no HONO	4.1e8	3.6 e6	1.03	0.46
HONO	4.5e8	4.3e6	1.23	0.58
5ppt BrO	4.1e8	4.5e6	1.00	0.58
10ppt BrO	4.0e8	5.4e6	0.99	0.70
HONO+5ppt BrO	4.4e8	5.2e6	1.20	0.68
HONO+10ppt BrO	4.3e8	6.2e6	1.18	0.83

Finally evidence from in situ balloon measurements [*Fitzenberger et al.,* 2000] and satellite observations [*Ritcher et al.,* 1998] indicate that BrO may be present throughout the troposphere. This satellite data shows a BrO column density that corresponds to mixing ratio of a few pptv if it is uniformly distributed throughout the troposphere over Greenland in the summer. Consequently, we believe that further study of photochemistry at Summit should address the potential link between HO_x and halogen chemistry in this environment.

3.7 Summary

The excellent agreement between modeled and observed values for HO_2+RO_2 indicates a good understanding of radical sources and sinks at Summit. The OH modeled to observed comparison is not as good, but improves substantially when filtered for high winds and averaged over the duration of the mission into a 24-hourr composite day. However, the model still under predicts the observed OH levels by a factor of two. Hydroxyl radical observations are much higher than model predictions during periods of high winds and blowing snow and rapid transport of marine air to Summit. This indicates that these conditions either produce an artifact within the CIMS or lead to enhanced OH partitioning. We suggest that low levels of BrO and/or IO could explain the observed (HO_2+RO_2)/OH ratio to a significant extent. Inclusion of HONO does improve the agreement between measured and modeled OH, but does not improve the agreement between the predicted and observed (HO_2+RO_2)/OH ratio. The impact of HONO on HO_x levels is ~ 20% on average which is well within the uncertainty of the measurements alone. For this reason, the impact of HONO in this environment is not elucidated by this data set.

3.8 References

Barrie, L. A., J. W. Bottenheim, R. C. Schnell, P. J. Crutzen, and R. A. Rasmussen (1988), Ozone Destruction and Photochemical-Reactions at Polar Sunrise in the Lower Arctic Atmosphere, *Nature*, *334*, 138-141.

Bloss, W. J., J. D. Lee, G. P. Johnson, R. Sommariva, D. E. Heard, A. Saiz-Lopez, J. M. C. Plane, G. McFiggans, H. Coe, M. Flynn, P. Williams, A. R. Rickard, and Z. L. Fleming (2005), Impact of halogen monoxide chemistry upon boundary layer OH and HO_2 concentrations at a coastal site, *Geophysical Research Letters*, *32*, -.

Chen, G., D. Davis, J. Crawford, L. M. Hutterli, L. G. Huey, D. Slusher, L. Mauldin, F. Eisele, D. Tanner, J. Dibb, M. Buhr, J. McConnell, B. Lefer, R. Shetter, D. Blake, C. H. Song, K. Lombardi, and J. Arnoldy (2004), A reassessment of HO_x South Pole chemistry based on observations recorded during ISCAT 2000, *Atmospheric Environment*, *38*, 5451-5461.

Crawford, J. H., D. D. Davis, G. Chen, M. Buhr, S. Oltmans, R. Weller, L. Mauldin, F. Eisele, R. Shetter, B. Lefer, R. Arimoto, and A. Hogan (2001), Evidence for photochemical production of ozone at the South Pole surface, *Geophysical Research Letters*, *28*, 3641-3644.

Dibb, J. E., L. G. Huey, D. L. Slusher, and D. J. Tanner (2004), Soluble reactive nitrogen oxides at South Pole during ISCAT 2000, *Atmospheric Environment*, *38*, 5399-5409.

Dibb, J. E., R. W. Talbot, J. W. Munger, D. J. Jacob, and S. M. Fan (1998), Air-snow exchange of HNO_3 and NO_y at Summit, Greenland, *Journal of Geophysical Research-Atmospheres*, *103*, 3475-3486.

Fitzenberger, R., H. Bosch, C. Camy-Peyret, M. P. Chipperfield, H. Harder, U. Platt, B. M. Sinnhuber, T. Wagner, and K. Pfeilsticker (2000), First profile measurements of tropospheric BrO, *Geophysical Research Letters*, *27*, 2921-2924.

Foster, K. L., R. A. Plastridge, J. W. Bottenheim, P. B. Shepson, B. J. Finlayson-Pitts, and C. W. Spicer (2001), The role of Br_2 and BrCl in surface ozone destruction at polar sunrise, *Science*, *291*, 471-474.

Hausmann, M., and U. Platt (1994), Spectroscopic Measurement of Bromine Oxide and Ozone in the High Arctic during Polar Sunrise Experiment 1992, *Journal of Geophysical Research-Atmospheres*, *99*, 25399-25413.

Helmig, D., J. Boulter, D. David, J. W. Birks, N. J. Cullen, K. Steffen, B. J. Johnson, and S. J. Oltmans (2002), Ozone and meteorological Summit, Greenland, boundary-layer conditions at during 3-21 June 2000, *Atmospheric Environment*, *36*, 2595-2608.

Honninger, G., and U. Platt (2002), Observations of BrO and its vertical distribution during surface ozone depletion at Alert, *Atmospheric Environment*, *36*, 2481-2489.

Hutterli, M. A., J. R. McConnell, G. Chen, R. C. Bales, D. D. Davis, and D. H. Lenschow (2004), Formaldehyde and hydrogen peroxide in air, snow and interstitial air at South Pole, *Atmospheric Environment*, *38*, 5439-5450.

Peterson, M. C., and R. E. Honrath (2001), Observations of rapid photochemical destruction of ozone in snowpack interstitial air, *Geophysical Research Letters*, *28*, 511-514.

Richter, A., F. Wittrock, M. Eisinger, and J. P. Burrows (1998), GOME observations of tropospheric BrO in northern hemispheric spring and summer 1997, *Geophysical Research Letters*, *25*, 2683-2686.

Ryerson, T. B., E. J. Williams, and F. C. Fehsenfeld (2000), An efficient photolysis system for fast-response NO_2 measurements, *Journal of Geophysical Research-Atmospheres*, *105*, 26447-26461.

Saiz-Lopez, A., J. M. C. Plane, and J. A. Shillito (2004), Bromine oxide in the mid-latitude marine boundary layer, *Geophysical Research Letters*, *31*, -.

Seibert, P., and A. Frank (2004), Source-receptor matrix calculation with a Lagrangian particle dispersion model in backward mode, *Atmospheric Chemistry and Physics*, *4*, 51-63.

Shetter, R. E., and M. Muller (1999), Photolysis frequency measurements using actinic flux spectroradiometry during the PEM-Tropics mission: Instrumentation description and some results, *Journal of Geophysical Research-Atmospheres*, *104*, 5647-5661.

Smith, S. C., J. D. Lee, W. J. Bloss, G. P. Johnson, T. Ingham, and D. E. Heard (2006), Concentrations of OH and HO_2 radicals during NAMBLEX: measurements and steady state analysis, *Atmospheric Chemistry and Physics*, *6*, 1435-1453.

Sommariva, R., W. J. Bloss, N. Brough, N. Carslaw, M. Flynn, A. L. Haggerstone, D. E. Heard, J. R. Hopkins, J. D. Lee, A. C. Lewis, G. McFiggans, P. S. Monks, S. A. Penkett, M. J. Pilling, J. M. C. Plane, K. A. Read, A. Saiz-Lopez, A. R. Rickard, and P. I. Williams (2006), OH and HO2 chemistry during NAMBLEX: roles of oxygenates, halogen oxides and heterogeneous uptake, *Atmospheric Chemistry and Physics*, *6*, 1135-1153.

Stohl, A., C. Forster, S. Eckhardt, N. Spichtinger, H. Huntrieser, J. Heland, H. Schlager, S. Wilhelm, F. Arnold, and O. Cooper (2003), A backward modeling study of intercontinental pollution transport using aircraft measurements, *Journal of Geophysical Research-Atmospheres*, *108*, -.

Stohl, A., C. Forster, A. Frank, P. Seibert, and G. Wotawa (2005), Technical note: The Lagrangian particle dispersion model FLEXPART version 6.2, *Atmospheric Chemistry and Physics*, *5*, 2461-2474.

Stutz, J., K. Hebestreit, B. Alicke, and U. Platt (1999), Chemistry of halogen oxides in the troposphere: Comparison of model calculations with recent field data, *Journal of Atmospheric Chemistry*, *34*, 65-85.

Stutz, J., E. S. Kim, U. Platt, P. Bruno, C. Perrino, and A. Febo (2000), UV-visible absorption cross sections of nitrous acid, *Journal of Geophysical Research-Atmospheres*, *105*, 14585-14592.

Swanson, A. L., N. J. Blake, J. E. Dibb, M. R. Albert, D. R. Blake, and F. S. Rowland (2002), Photochemically induced production of CH_3Br, CH_3I, C_2H_5I, ethene, and propene within surface snow at Summit, Greenland, *Atmospheric Environment*, *36*, 2671-2682.

von Glasow, R., R. von Kuhlmann, M. G. Lawrence, U. Platt, and P. J. Crutzen (2004), Impact of reactive bromine chemistry in the troposphere, *Atmospheric Chemistry and Physics*, *4*, 2481-2497.

Yang, J., R. E. Honrath, M. C. Peterson, J. E. Dibb, A. L. Sumner, P. B. Shepson, M. Frey, H. W. Jacobi, A. Swanson, and N. Blake (2002), Impacts of snowpack emissions on deduced levels of OH and peroxy radicals at Summit, Greenland, *Atmospheric Environment*, *36*, 2523-2534.

CHAPTER 4

PEROXY AND HYDROXYL RADICAL MEASUREMENTS OBTAINED FROM THE SPRING 2004 FIELD CAMPAIGN AT SUMMIT, GREENLAND

4.1 Introduction

In order to study the impact of snow emissions on the photochemistry of the arctic boundary layer two field campaigns at Summit, Greenland were carried out in the summer of 2003 and the spring of 2004. The radical chemistry was directly probed during both of these campaigns by chemical ionization mass spectrometry (CIMS) measurements of peroxy (HO_2+RO_2) and hydroxyl (OH) radicals. In addition, a wide range of other species such as photolysis frequencies, radical precursors, nitric oxide, and hydrocarbons were also measured to highly constrain model calculations of the radical number densities. This allowed for a critical test of our understanding of photochemistry at Summit.

The summer 2003 results have been discussed in Chapter 3 and are only briefly summarized here. Median number densities for peroxy radicals during the summer field campaign were 2.4×10^8 molecules cm^{-3} for the entire mission and were 4.1×10^8 molecules cm^{-3} for noontime (10:00 A.M.-3:00 P.M. WGST); both in accord with model predictions. In contrast hydroxyl number densities were generally a factor of two greater

than model predictions indicating an unaccounted for source of OH. The agreement between model and observed was generally best around noon, although this was dependent on meteorological conditions. An analysis of the HO_x budget indicated that photolysis of ozone and hydrogen peroxide were the major sources and HO_x radical self reactions were the dominant sinks [*Chen et al.,* in review]. For this reason predicted HO_x levels were found to be insensitive to measured HONO and CH_2O.

In this chapter the results of the Summit, Greenland spring 2004 campaign are presented. Measurements of peroxy, hydroxyl, and nitric oxide radicals were obtained from March 27 to April 29, a period when photolysis rates and temperatures were rapidly changing. Previous field campaigns have shown elevated concentrations of HO_x precursors such as HONO [*Dibb et al.,* 2004; *Dibb et al.,*2002; *Honrath et al.,* 2002; *Zhou et al.,*2000; *Beine et al.,* 2000; *Li.,* 1992], CH_2O [*Reidel et al.,* 2005; *Frey et al.,* 2004; *Sumner et al.,* 2002; *Sumner and Shepson,* 1999; *Hutterli et al.,* 1999] and H_2O_2 [*Frey et al.,* 2005; *Jacobi et al.,* 2004; *Hutterli et al.,* 2004:2001; *McConnell et al.,* 1997; *Bales et al.,* 1995] at high latitude sites. Elevated NO_x [*Ridley et al.,* 2000; *Jones et al.,* 2000:1999; *Davis et al.,* 2004:2001; *Dibb et al.,* 2002] has also been observed during polar field campaigns. The enhancement of NO_x and HO_x precursors has been attributed to emission from the snowpack and was expected to influence HO_x concentrations in the polar boundary layer. Comparison of the measured radical levels to calculated values from a 0-D steady state photochemical model are presented and a radical budget is derived. In particular, this chapter allows a more thorough investigation of other potential HO_x sources such as HONO, CH_2O, and H_2O_2 since the ozone photolysis channel is diminished at lower dew points and higher solar zenith angles. In addition,

this data set allows us to evaluate our understanding of HO_x chemistry in this polar environment over a wide range of physical and chemical conditions.

4.2 Methods

The hydroxyl and peroxy measurement technique has been described in Chapter 2. The instrumental configuration of the CIMS was essentially the same as in the summer field campaign although in the spring the CIMS was housed in a moveable heated building with the peroxide/formaldehyde and NO instruments. The plumbing in the CIMS was also modified for the spring campaign to reduce the time required to switch from peroxy measurement mode to hydroxyl measurement mode (Chapter 2). The 0-D steady state model used in the summer 2003 field campaign was also employed during the spring 2004 field campaign. However, to determine the effect of the snowpack emission the model was modified to predict concentrations of formaldehyde and hydrogen peroxide from gas phase chemistry. The suite of measurements used to constrain the model in the summer 2003 mission (Chapter 3) was available for the spring 2004 field campaigns

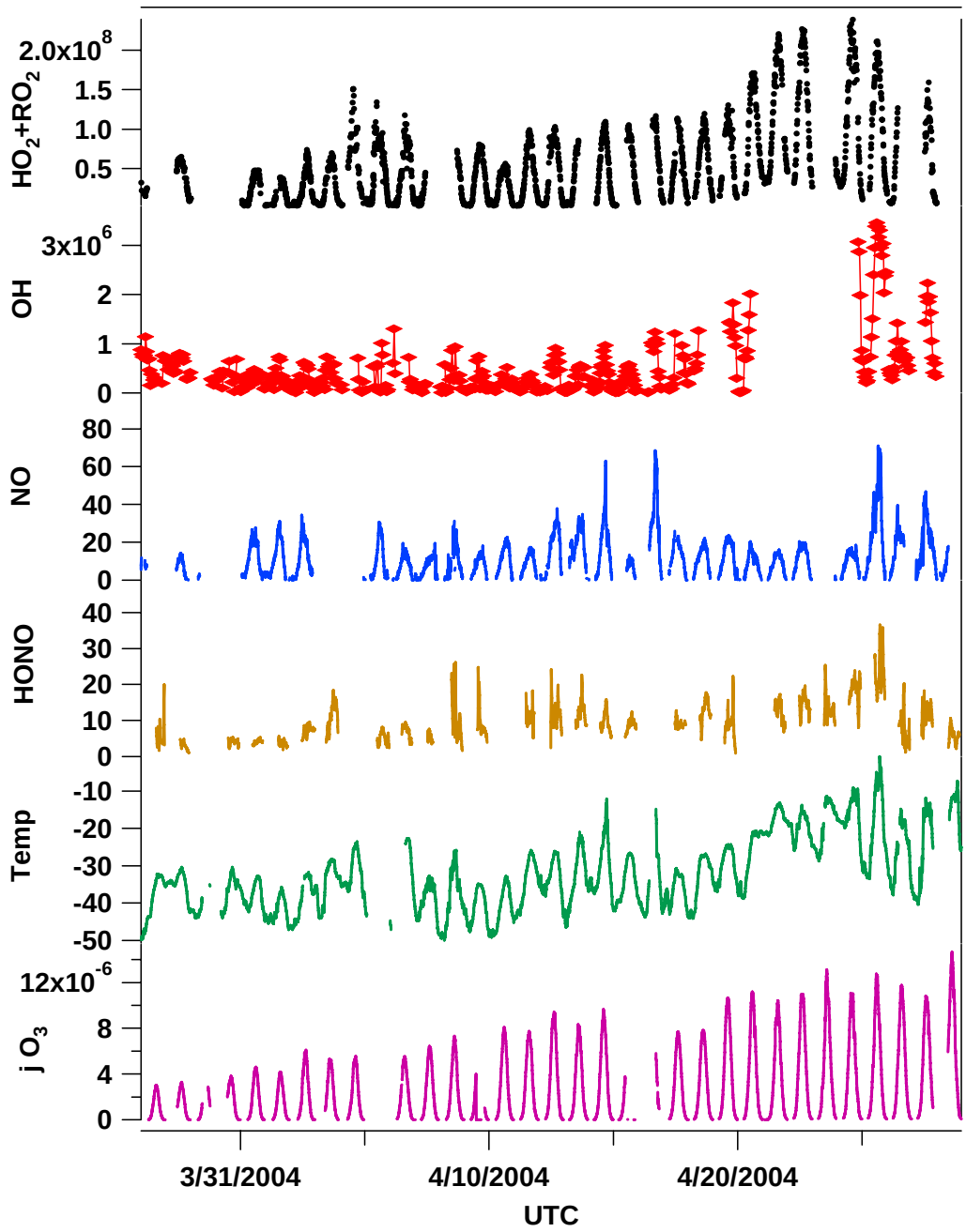

Figure 4.1 Time series for peroxy radicals (black dots), hydroxyl radicals (red diamonds), nitric oxide (blue line), HONO (tan line), temperature (green line) and photolysis rate of ozone (purple line). HO_2+RO_2 and OH measurements are listed as number densities (molecules cm^{-3}). NO and HONO measurements are in pptv. Temperature is in centigrade and j O_3 measurements are in s^{-1}. All values are averaged over 10 minutes except for hydroxyl radicals which are averaged hourly

4.3 Results

As expected, spring 2004 peroxy and hydroxyl data were much lower than summer 2003 values, however NO mixing ratios were of similar magnitude for both campaigns. A time series of measurements of peroxy radicals, hydroxyl radicals, NO, HONO, temperature, and ozone photolysis rates (jO_3) is presented in figure 4.1. Since the spring field campaign occurred during a period of rapidly changing conditions (i.e., insolation and temperature), the data have been divided into an early (prior to April 11) and a late (after April 19th) period.

4.3.1 Peroxy Radicals (HO_2+RO_2)

These changes were also apparent in the rapid increase in noontime HO_2+RO_2 measurements during the mission (Table 4.1). For example, the observed midday concentration of HO_2+RO_2 radicals on April 25 was a factor of five higher than the midday concentration on March 27 (Figure 4.1). The early median HO_2+RO_2 radical number density was 2.2×10^7 molecules cm^{-3} (mean =3.0×10^7 molecules cm^{-3}), while the late median number density was 9.5×10^7 molecules cm^{-3} (mean=1.0×10^8 molecules cm^{-3}). For local noon (10:00 A.M.-3:00 P.M. WGST) the early median number density was 6.0×10^7 molecules/cm^3 (mean=6.2×10^7 molecules cm^{-3}), and the late median number density was 1.9×10^8 molecules cm^{-3} (mean=1.8×10^8 molecules cm^{-3}). For noontime values the early period median HO_2+RO_2 concentration was ~15% of the summer 2003 concentration, and the later period increased to ~50% of the summer values.

Table 4.1 Comparison of median noontime (10:00-15:00 WGST) concentrations of peroxy and hydroxyl radicals and nitric oxide

Species	Early (Before 4/11)	Late (After 4/19)	Summer 2003
HO_2+RO_2	$6.0x10^7$molecules cm^{-3}	$1.9x10^8$molecules cm^{-3}	$4.1x10^8$molecules cm^{-3}
OH	$4.1x10^5$molecules cm^{-3}	$1.9x10^6$molecules cm^{-3}	$8.4x10^6$molecules cm^{-3}
NO	18 pptv	19 pptv	18 pptv
NO_2 Predicted	14 pptv	18 pptv	23 pptv
τ_{NOx}	7.0 hr	6.2 hr	7.2 hr

4.3.2 Hydroxyl Radicals (OH)

For the early spring the median OH concentration was $2.5x10^5$ molecules cm^{-3} (mean=$3.0x10^5$ molecules cm^{-3}), with ~40% of the measurements at or below the detection limit. The late spring OH measurements increased to a median of $8.9x10^5$ molecules cm^{-3} (mean=$1.2x10^6$ molecules cm^{-3}). The median noontime number density of hydroxyl was $4.1x10^5$ molecules cm^{-3} (mean=$4.5x10^5$ molecules cm^{-3}) for the early period and increased to $1.9x10^6$ molecules cm^{-3} (mean=$2.0x10^6$ molecules cm^{-3}) for the late period. The median noontime number density of hydroxyl radicals during the early spring was ~5% of the summer concentrations. The late spring noontime OH number density increases to 25% of the median summer concentration. It should be noted that the late spring OH data set was limited due to the removal of measurements obtained during periods of high winds (>6 m/s). Periods of high winds have led to high hydroxyl concentrations in both the summer (Chapter 3) and spring campaigns (see below). After filtering the data it appears that the HO_2+RO_2/OH ratio steadily decreased through the spring measurement period.

4.3.3 Nitric Oxide (NO)

In contrast to the peroxy and hydroxyl radicals, noontime NO levels were much closer to the summer mixing ratios during the entire spring mission. The noontime values were similar to midday mean measured mixing ratios from the Summit summer 1999 (24.7 pptv) and 2000 (16.0 pptv) field campaigns [*Yang et al.,* 2002]. We also predicted NO_2 mixing ratios for each temperature regime and used them to calculate the NO_x lifetime (τ_{NOx}) to determine if this was impacting the observed NO levels. Formation of nitric acid (HNO_3) and pernitric acid (HO_2NO_2) are the two loss terms for NO_x. Since the photolytic lifetime of nitric acid was long and oxidation by the hydroxyl radical was slow ($\tau_{HNO3} \approx 3$ weeks), HNO_3 formation was considered a NO_x loss. By comparison formation of pernitric acid was considered a NO_x reservoir with highly variable lifetime that was strongly dependent on temperature. Although thermal decomposition, photolysis, oxidation, and deposition all determine the lifetime of HNO_4 only the fraction of HNO_4 that deposits is a NO_x loss.

$$\tau_{NO_x} = \frac{\frac{[NO]}{[NO_2]} + 1}{k[OH] + k[HO_2](\frac{k_{Deposit}}{HNO_4 loss})}$$

Interestingly, the calculated lifetime for NO_x remained fairly constant despite the dramatic increase in HO_x. This can be attributed to increased thermal decomposition of pernitric acid at warmer temperatures. In the early spring deposition of pernitric acid was estimated to account for roughly 95% of the NO_x loss; the other 5% is due to formation of nitric acid (HNO_3). By comparison, in summer 2003 NO_x losses were predicted to be evenly divided between HO_2NO_2 and HNO_3.

There is, however, an increase in the median NO mixing ratio when all measurements were compared for the spring campaign. The early spring median NO mixing ratio was 8 pptv and increased to a late spring mixing ratio of 13 pptv. The late spring value is the same as the median summer 2003 NO mixing ratio of 13 pptv. This change during the spring campaign was not unexpected since the amount of daylight was increasing dramatically during this period. The NO time series (Figure 1) exhibits the expected diurnal profile and there exists a moderate correlation ($R^2 = 0.36$) between the photolysis rate of nitrate and NO. Since photolysis of nitrate cannot account for all of the variance in the NO measurement, other factors such as boundary layer depth and mixing time may also play a role. For example, there exists a small anticorrelation ($R^2=0.09$) with wind speed. This was probably due to a higher boundary layer and longer mixing times during the high wind events. However, ventilation of the higher NO concentrations within the firn may offset these effects.

4.4 Model Comparison

Predictions from a highly constrained 0-D steady-state photochemical model were used to compare measurements of peroxy and hydroxyl radicals. Of particular interest was the role of HONO in the spring. Therefore, two model runs were performed to asses the impact of HONO on the HO_x levels. The first constrained all measured HO_x precursors including HONO. The second was constrained to the same suite of measurements except HONO. HONO values were calculated from steady state.

4.4.1 Peroxy Radicals (HO_2+RO_2)

When the model was constrained to HONO (Figure 4.2, upper panel) the predicted HO_2+RO_2 concentrations exceeded the measured values by a factor of 2.2 (median). The modeled (M) to observed (O) ratio was highest during the early period (M/O =2.4), and decreased to 1.74 in the late period. By comparison the median M/O ratio for peroxy number densities over the entire mission was 1.05 when predicted HONO was employed (Figure 4.2, lower panel). The early period also had a slightly higher median ratio (M/O =1.06) than the late period (M/O = 0.99). The median mixing ratio of HONO for the spring campaign is 8.8 pptv (mean = 10.0 pptv). By comparison the median predicted HONO mixing ratio from steady state for the spring campaign was 0.04 pptv (mean = 0.06 pptv).

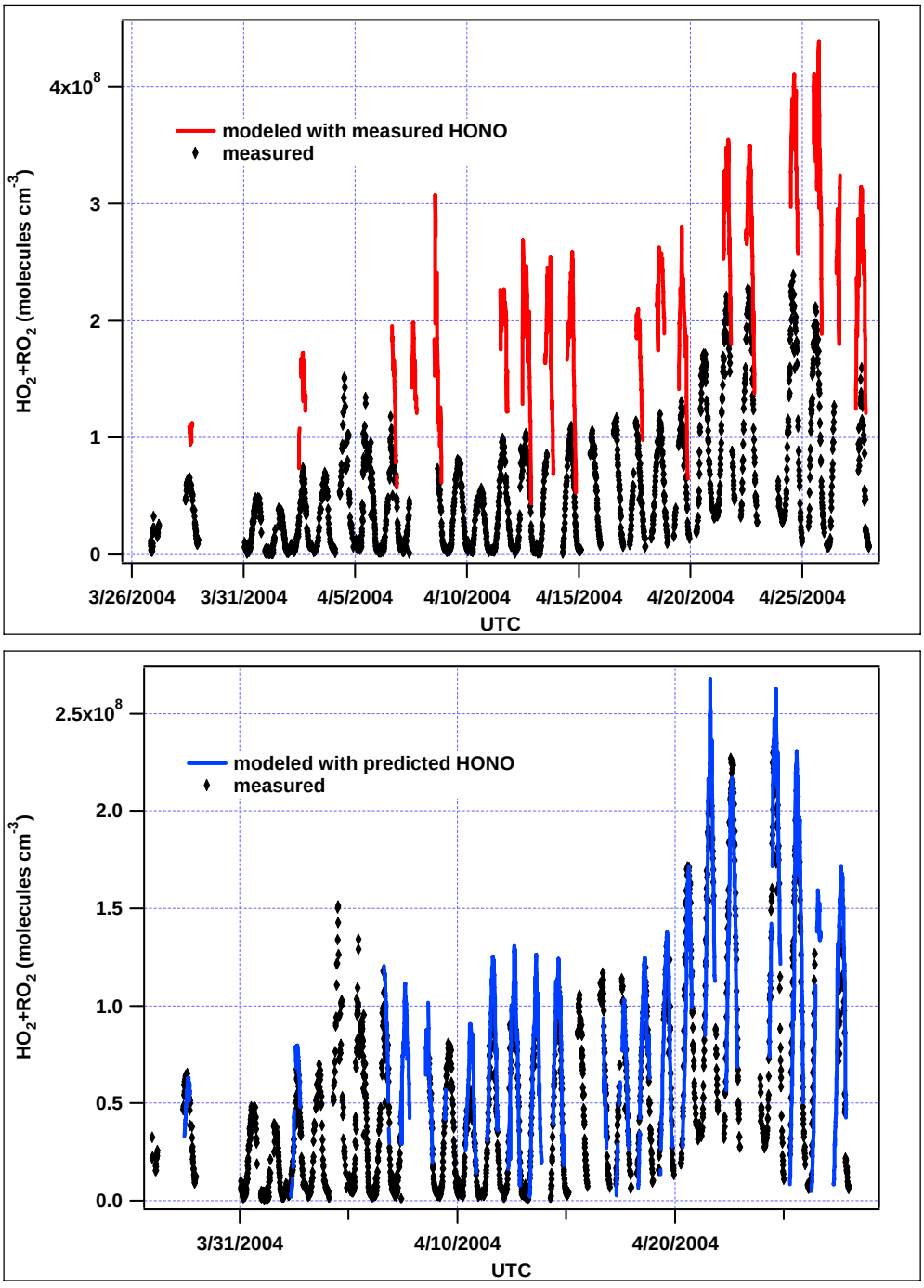

Figure 4.2 Time series of HO_2+RO_2 measurements and model predictions. The top chart has predicted HO_2+RO_2 values that were constrained to measured concentrations of HONO. The bottom chart has predicted HO_2+RO_2 values constrained to predicted concentrations of HONO.

Model sensitivity analysis determined that measured HONO would have to be reduced by a factor of six to bring predictions to within the uncertainty of the HO_2+RO_2 measurement. The correlation between modeled (with predicted HONO) and observed HO_2+RO_2 concentrations was a robust 0.86 (Figure 4.3) for the entire mission. The correlation between modeled HO_2+RO_2 with measured HONO values is also very strong (R^2=0.80).

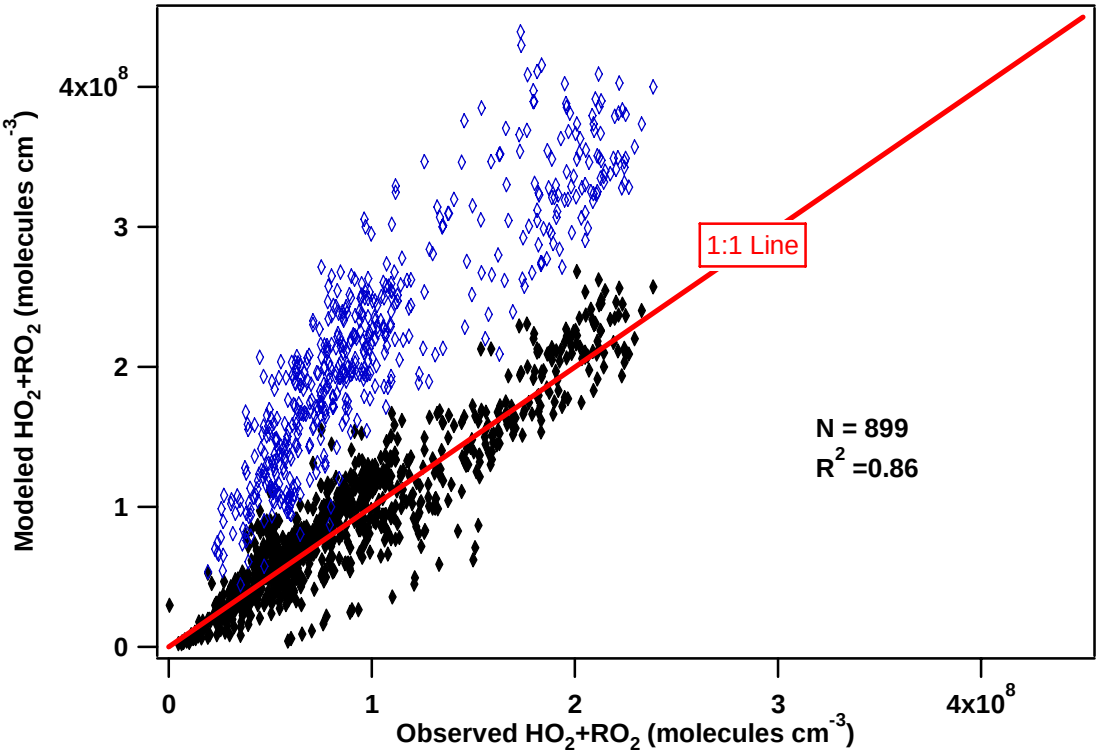

Figure 4.3 Scatter plot of modeled and observed HO_2+RO_2 radicals. Open blue diamonds represent model runs with measured HONO. Solid black diamonds represent model runs with predicted HONO concentrations

4.4.2 Hydroxyl Radical (OH)

As mentioned previously, 70% of hourly average OH measurements were within a factor of three of the limit of detection. This result was not surprising given the attenuated primary production from high solar zenith angles and low dew points. Elevated CO mixing ratios of 150-170 ppb, an approximately 50% enhancement compared to summer values, also enhance the ratio of HO_2/OH. However, the model was in reasonable agreement with the measured values if predicted HONO values are employed. Figure 4.4 (lower panel) shows that the median modeled to observed ratio is 0.78 (mean=0.94). When HONO measurements constrain the model (Figure 4.4, upper panel) the median modeled to observed ratio increases to 2.34 (mean=2.70).

This is in accord with the over prediction of HO_2+RO_2 when the model is constrained to HONO observations. Figure 4.5 indicates that the correlation between model calculations (HONO predicted) of OH and measured OH is reasonably strong (R^2 0.55). The correlation between modeled OH (HONO measured) and measured OH is similar (R^2=0.60), even though the predicted values are more than a factor of two greater than the observed concentrations.

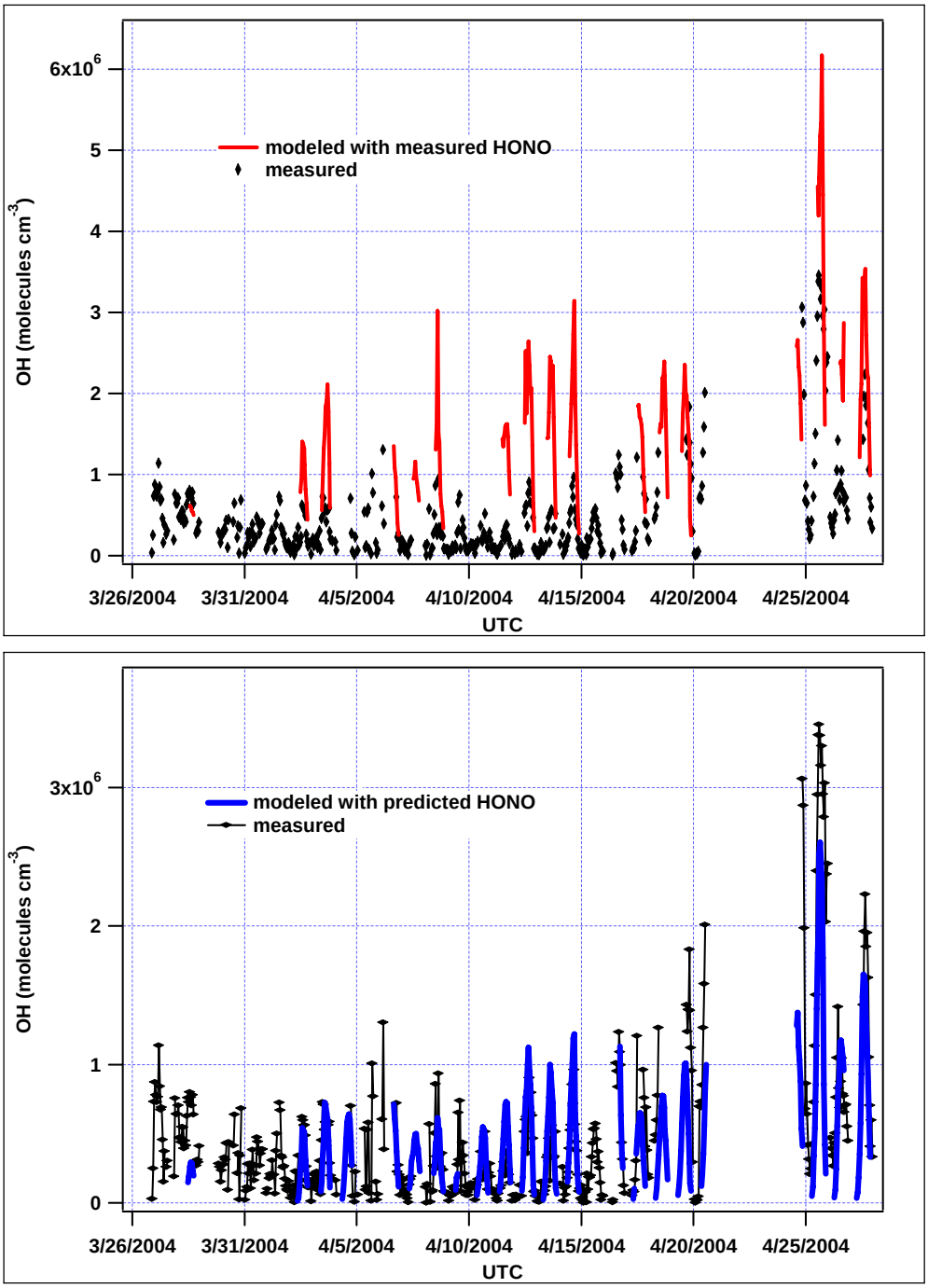

Figure 4.4 Time series of OH measurements and model predictions. The top chart has predicted OH values that were constrained to measured concentrations of HONO. The bottom chart has predicted OH values constrained to predicted concentrations of HONO.

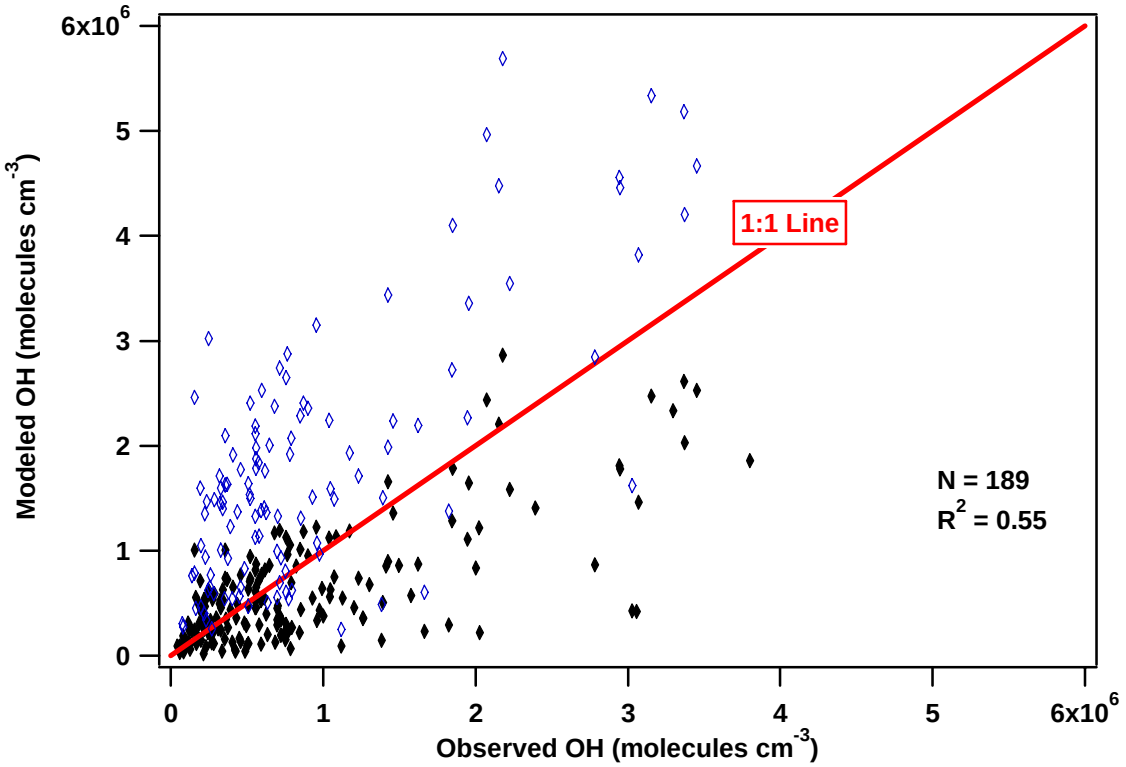

Figure 4.5 Scatter plot of modeled and observed OH radicals. Open blue diamonds represent model runs with measured HONO. Solid black diamonds represent model runs predicted HONO concentrations

As in the summer 2003 field campaign OH enhancements during high wind events were observed. On April 21 through 24 observed OH number densities were as high as 1.5×10^7 molecules cm^{-3}. This may again indicate that unaccounted for cycling of HO_2 to OH may be occurring during the high wind event (Chapter 3). Retroplume simulations from the Lagrangian particle dispersion model FLEXPART [*Stohl et al.,* 2005] indicate that the air sampled at Summit had recently been over the North Sea. Cycling of HO_2 to OH by halogens has been observed at maritime sites [*Bloss et al.,* 2005, *Saiz-Lopez et al.,* 2004] and has been suggested as a possible mechanism for OH enhancement at Summit (Chapter 3).

4.4.3 HO_x production

Another test of the observed HO_x chemistry was to compare the correlation of measured and predicted values in chemical coordinates [*Cohen et al.,* 2000]. If HONO measurements were included they will be the dominant HO_x source accounting for ~70% of the total budget (see Discussion). To a first approximation, production of HO_x ($P(HO_x)$ will equal the photolysis of rate of HONO (j[HONO]). The major loss terms for HO_x are reaction of HO_2 radicals with themselves and deposition of pernitric acid. Therefore,

$$\frac{d[HO_x]}{dt} \cong j[HONO] - k[HO_2]^2 - k_{deposit}[HNO_4]$$

The modeled HO_2+RO_2 concentrations exhibit a strong correlation with respect to $P(HO_x) \approx j$[HONO]. In figure 4.6 linear regressions of modeled HO_2+RO_2 (upper graph) and observed HO_2+RO_2 (lower graph) are plotted as a functions of the square root of production of HO_x from HONO and are color coded with dew point. The correlation between predicted HO_2+RO_2 radical levels and $(j[HONO])^{1/2}$ is strong (R^2=0.85). However, the correlation falls off significantly when measured HO_2+RO_2 concentrations are plotted versus $(j[HONO])^{1/2}$ (R^2=0.64). The observed data points that are in greatest disagreement with $(j[HONO])^{1/2}$ occur at the highest dew points.

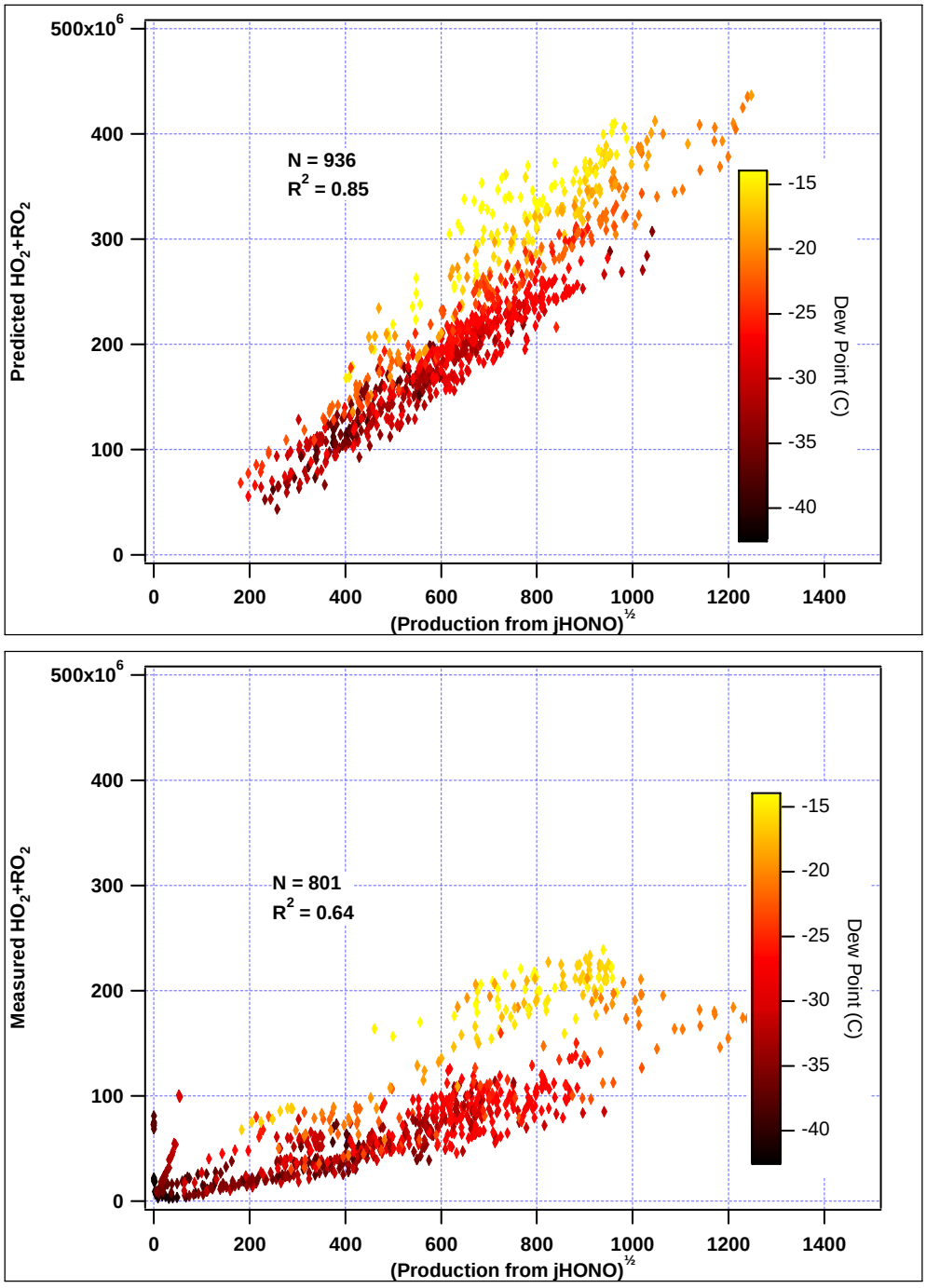

Figure 4.6 Predicted peroxy concentrations (top) and measured peroxy concentrations (bottom) vs the square root of production of HO_x from photolysis of HONO. The data are color coded to dew point.

By comparison when the predicted HONO values were excluded from peroxy number density calculations then HO_x production was split between photolysis of ozone, formaldehyde and hydrogen peroxide. If, to a first approximation, we assume that production of HO_x is due to photolysis of ozone then $P(HO_x) \approx j[O_3]$.

1. $O_3 + h\nu \rightarrow O_2 + O(^1D)$
2. $O(^1D) + N_2 \rightarrow O(^3P) + N_2$
3. $O(^1D) + O_2 \rightarrow O(^3P) + O_2$
4. $O(^1D) + H_2O \rightarrow 2OH$

It is important to recognize that water concentrations are intimately connected to HO_x production from ozone.

$$\frac{d[HO_x]}{dt} = j[O_3]\left(\frac{k_4[H_2O]}{k2[N_2] + k_3[O_2] + k_4[H_2O]}\right) - k[HO_2]^2 - k_{deposit}[HNO_4]$$

Again the modeled HO_2+RO_2 values displayed a strong correlation to production from ozone. Linear regressions of predicted HO_2+RO_2 (Figure 4.7, upper panel) and measured HO_2+RO_2 (Figure 4.7, lower panel) are plotted as a function of the square root of the production of HO_x from ozone of $(j[O_3])^{1/2}$ and are also color coded as a function of dew point. The correlation between predicted HO_2+RO_2 and $(j[O_3])^{1/2}$ is excellent (R^2 of 0.96). The correlation between measured HO_2+RO_2 and the square root of ozone production is also very high (R^2=0.90).

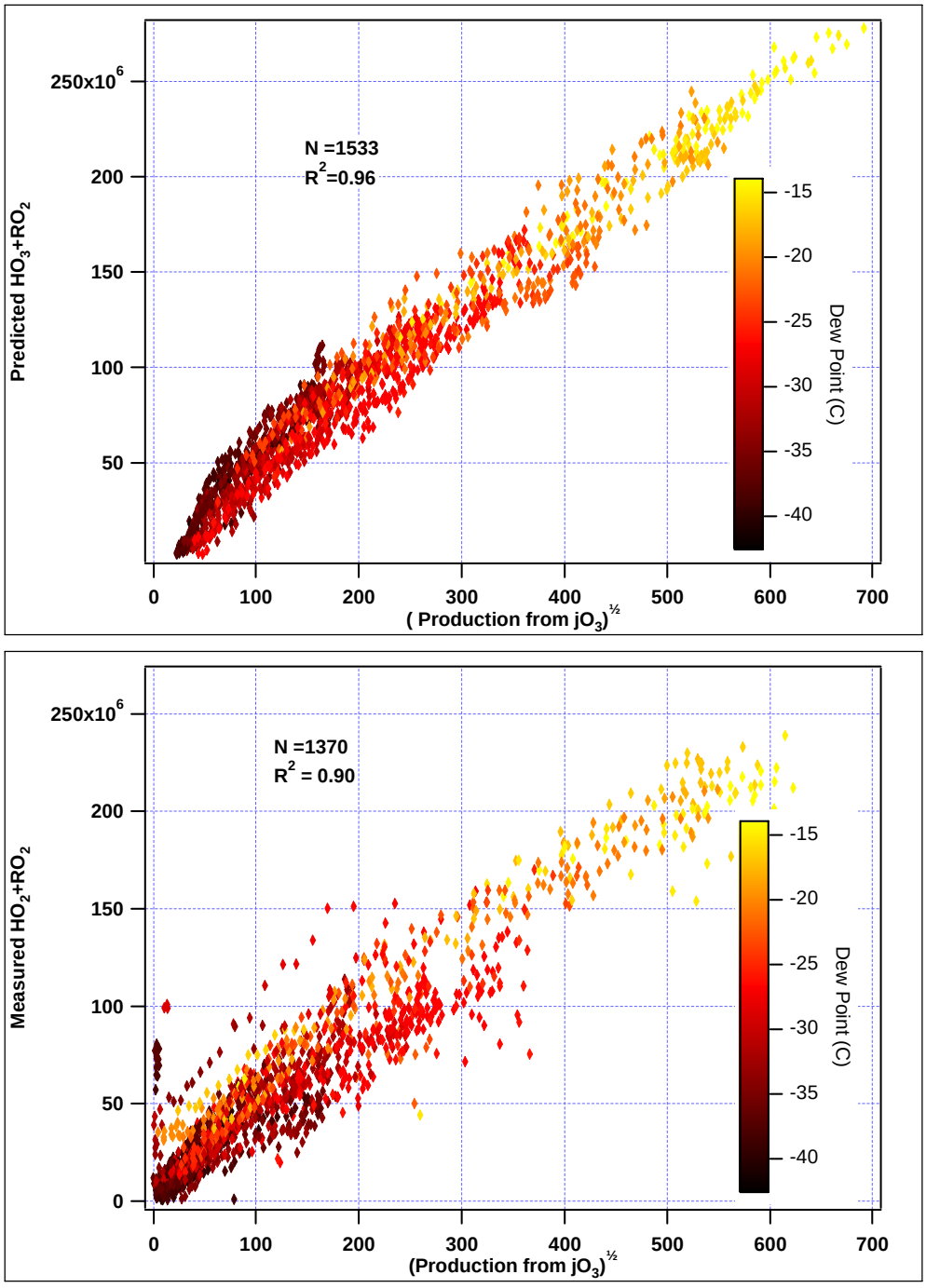

Figure 4.7 Predicted peroxy concentrations (top) and measured peroxy concentrations (bottom) vs the square root of production of HO_x from photolysis of ozone. The data are color coded to dew point.

The agreement between the measured peroxy number densities with model peroxy concentrations obtained with predicted HONO values (M/O = 1.05) and the correlation between $P(HO_x) \approx jO_3$ indicates that observed soluble nitrite is not just gas phase HONO.

4.5 Budget Analysis

Primary production by photolysis of ozone and hydrogen peroxide were the largest sources of HO_x during the summer 2003 field campaign and overwhelmed the contributions of the other precursors emitted from the snowpack [*Chen et al.*, 2006]. The spring 2004 field campaign was conducted in an environment where the ozone photolytic source was initially attenuated. The magnitude of HO_x production from photolysis of ozone undergoes significant change over the measurement period. The noontime photolysis rate of ozone (jO_3) changes by a factor of four. By comparison the noontime photolysis rates of HONO (jHONO) and NO_2 (jNO_2) change by a factor of two and photolysis of nitrate ($jNO_3^-{}_{(aq)}$) changes by a factor of three. Noontime H_2O number densities vary by an order of magnitude during the campaign. Sensitivity analyses were conducted with the 0-D steady state model to determine the contributions of each HO_x precursor. The initial run was constrained to all measured values and the model over predicted peroxy radical concentrations by a factor of two (Figure 4.2, upper panel). HONO was by far the largest source accounting for ~70% of the total budget. A second run was performed with predicted HONO concentrations and the model was in excellent agreement with measured values (Figure 4.3). Inclusion of HONO has caused problems with comparisons between model predictions and observations at the South Pole [*Chen et al.*, 2004] and Halley Bay [*Bloss et al.*, 2005] as well. Since inclusion of HONO is

incompatible with measured values, the HO_x budget will be calculated in the absence of measured HONO values.

In figure 4.8 the relative contribution of photolytic sources is obtained from a steady state model constrained to measured values of all HO_x precursors except HONO. The budget indicates that both formaldehyde and hydrogen peroxide play a larger role than photolysis of ozone during the early period of the field campaign. Not surprisingly, ozone photolysis again becomes the largest HO_x source when solar zenith angles decrease and dew points rise in late spring.

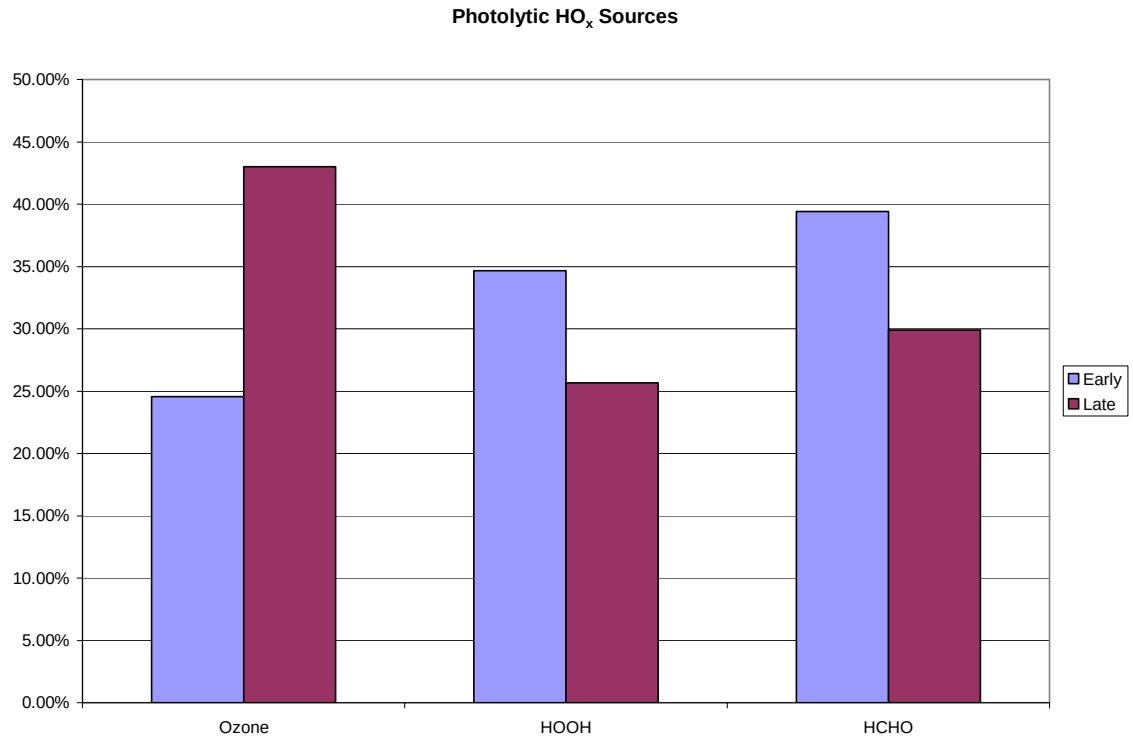

Figure 4.8 Relative contributions of the photolytic sources to the HO_x budget during the spring 2004 field campaign at Summit

The predicted HO_x sinks are displayed in figure 4.9. During the early period deposition of pernitric acid was predicted to be the dominant HO_x sink. As temperatures rise (decreasing HNO_4 lifetime) and $P(HO_x)$ increases the self reaction of HO_2 becomes

the dominant HO_x loss pathway. The middle loss column, methane oxidation, deserves added attention. It includes not only the oxidation of methane, but also HO_x production and/or loss from methyl peroxy radicals (CH_3O_2) and methyl hydrogen peroxide (CH_3OOH) (see section 1.2.3 in Chapter 1). The magnitude of methane oxidation as a sink (or a possible source) is dependent on NO_x concentrations

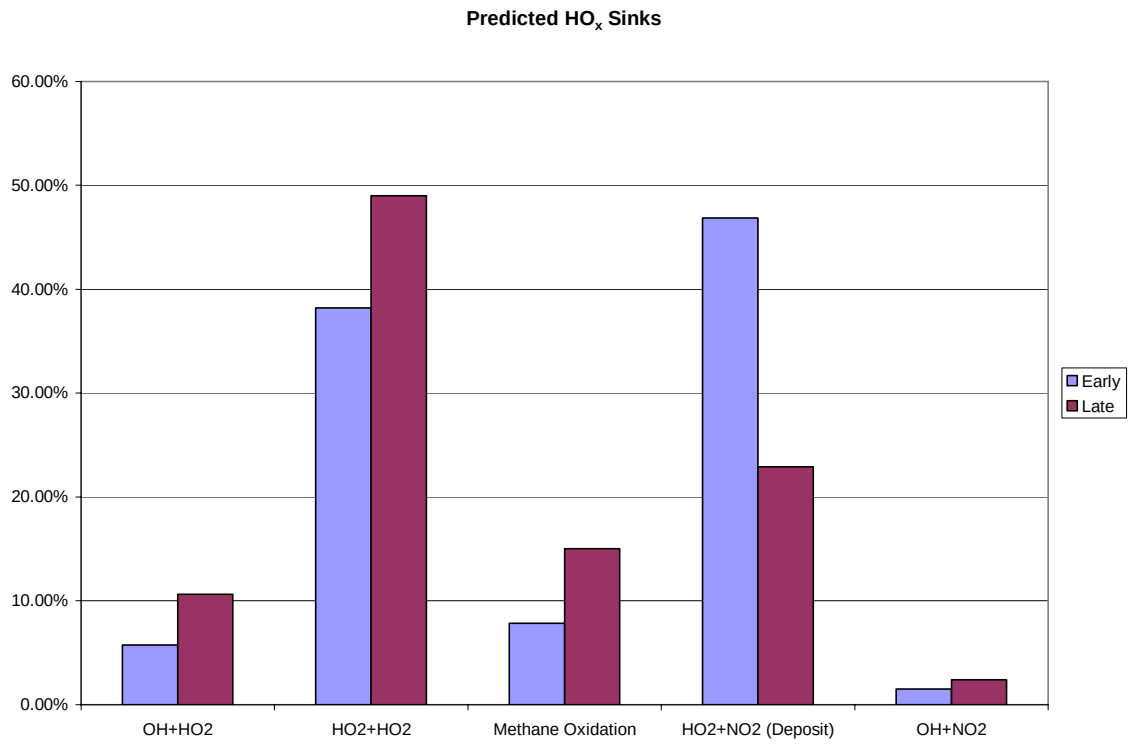

Figure 4.9 Relative magnitude of predicted HO_x sinks for the spring 2004 field campaign at Summit

Methane oxidation leads to another way of looking at the source budget. Formaldehyde is a product of methane oxidation. Therefore a fraction of the total observed formaldehyde concentration has been generated by photochemistry. Since formaldehyde has a relatively short lifetime ($\tau_{CH2O} \approx 5$hrs) it was calculated from a steady state assumption.

$$[HCHO]_{ss} = \frac{k[CH_3O_2][NO] + (2k_a + k_b)[CH_3O_2]^2 + j[CH_3OOH] + k[CH_3OOH][OH]}{j_{H_2+CO} + j_{H+HCO} + k[OH]}$$

The difference between predicted and observed values of formaldehyde was attributed to a snow source. Methane oxidation can account for ~40% of the observed formaldehyde during the early spring and ~60% of the measured formaldehyde during the late spring.

Hydrogen peroxide has a significantly longer lifetime (τ_{HOOH} ~ two days) and the steady state approximation breaks down. Therefore, a time dependent method was employed in order to account for the contribution of observed H_2O_2 from gas phase photochemistry.

$$[H_2O_2]_{n+1} = \frac{k[HO_2]_n}{(j + k[OH]_n)}[HO_2] + ([H_2O_2]_n - \frac{k[HO_2]_n}{(j + k[OH]_n)}[HO_2])e^{-(j+k[OH])\Delta T}$$

The predicted concentration of hydrogen peroxide is calculated on a 10 minute time step from photochemical production and loss (reactions 55 and 17). The percentage of observed H_2O_2 was calculated from the ratio of the change in predicted hydrogen peroxide to the change in observed hydrogen peroxide.

$$\frac{\Delta[H_2O_2]_{pred}}{\Delta[H_2O_2]_{obs}} = \frac{[H_2O_2]_{pred\,n+1} - [H_2O_2]_{pred\,n}}{[H_2O_2]_{obs\,n+1} - [H_2O_2]_{obs\,n}}$$

The ratio of photochemical production of H_2O_2 to the change in observed H_2O_2 provides a first order prediction of the magnitude of the snow source. During the early period of

the spring campaign ~20% of the daily change in hydrogen peroxide can be attributed to gas phase photochemistry. By the late spring gas phase photochemistry can account for half of the daily change.

Therefore, we estimate that photochemistry accounts for ~33% of the $P(HO_x)$ during the early period and ~55% of $P(HO_x)$ during the late spring (Figure 4.10), Snow sources of hydrogen peroxide and formaldehyde account for ~50% of $P(HO_x)$ during the early period and ~33% of $P(HO_x)$ during the late period. Methane oxidation accounts for the remaining HO_x production.

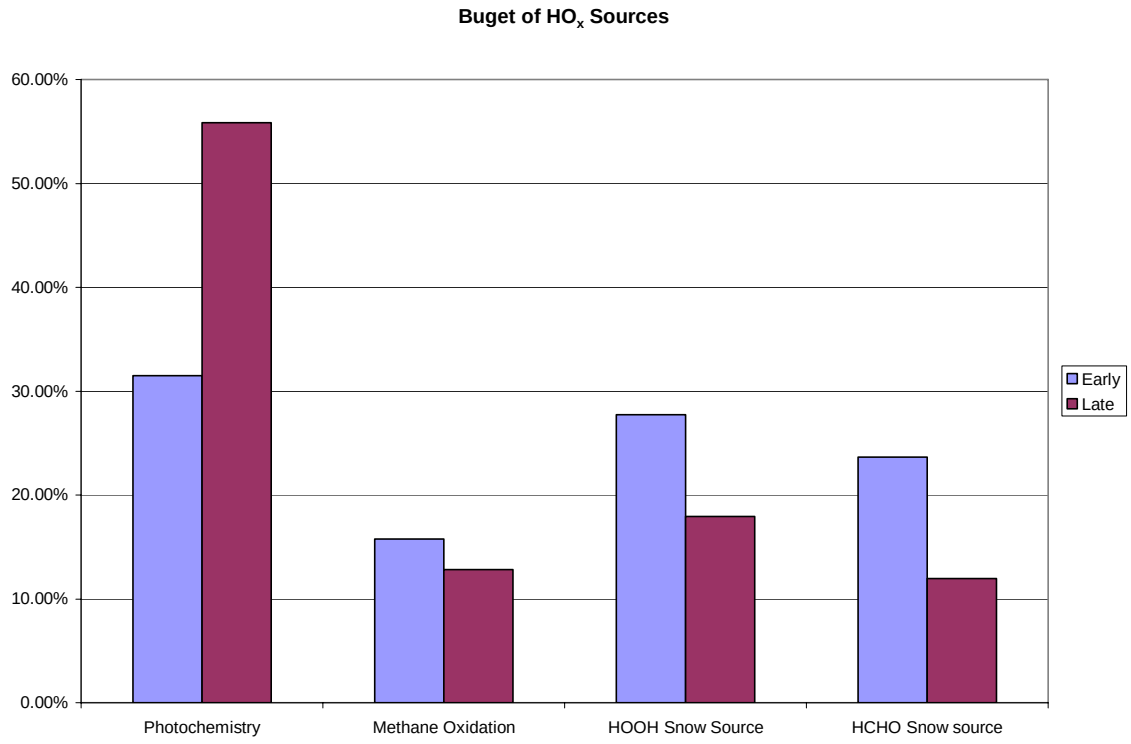

Figure 4.10 Revised HO_x budget accounting for chemical sources for the spring 2004 field campaign at Summit

4.6 Summary

The HO_2+RO_2 measurements were in excellent agreement with model predictions if HONO was excluded as a constraint (M/O =1.05 and R^2=0.85). Addition of HONO causes the model to over predict observed HO_2+RO_2 by more than a factor of two. This is opposed to our findings during the summer 2003 field campaign when inclusion of HONO did not appreciably alter predicted HO_2+RO_2 values. However, HONO measurements have been difficult to reconcile with model predictions and HO_x observations in other polar campaigns [*Chen et al.*, 2004; *Bloss et al.*, 2005] and may be questionable in other environments. Measured values of HO_2+RO_2 display a much stronger correlation with photolysis of ozone (R^2=0.90) than with photolysis of nitrous acid (R^2=0.64). This further indicates that soluble nitrite measurement does not correspond to just gas phase HONO.

OH concentrations were also in reasonable agreement with model predictions if not constrained to HONO (M/O = 0.74 and R^2=0.55). The modeled to observed OH ratios were within the uncertainty of the measurement. The relatively high observed OH concentrations indicate that HO_2/OH ratios were perturbed in the spring but not to the same magnitude that they are in summer (Chapter 3). OH enhancement was again observed during high wind events. This suggests that the possible HO_x cycling processes (halogens) encountered in summer were also present during the spring.

Finally budget analysis shows that hydrogen peroxide and formaldehyde were the largest sources during the early spring. The majority of measured H_2O_2 (~80%) and CH_2O (~60%) obtained before April 11 were attributed to the snowpack. After April 19 about half of the H_2O_2 and ~60% of the CH_2O can be attributed to photochemical

production. In the early spring period gas phase photochemistry is estimated to be responsible for a third of the HO_x production. By late spring over half of the HO_x production can be attributed to gas phase photochemistry.

4.7 References

Beine, H. J., and T. Krognes (2000), The seasonal cycle of peroxyacetyl nitrate (PAN) in the European Arctic, *Atmospheric Environment*, *34*, 933-940.

Bloss, W. J., J. D. Lee, G. P. Johnson, R. Sommariva, D. E. Heard, A. Saiz-Lopez, J. M. C. Plane, G. McFiggans, H. Coe, M. Flynn, P. Williams, A. R. Rickard, and Z. L. Fleming (2005), Impact of halogen monoxide chemistry upon boundary layer OH and HO_2 concentrations at a coastal site, *Geophysical Research Letters*, *32*, -.

Chen, G., D. Davis, J. Crawford, L. M. Hutterli, L. G. Huey, D. Slusher, L. Mauldin, F. Eisele, D. Tanner, J. Dibb, M. Buhr, J. McConnell, B. Lefer, R. Shetter, D. Blake, C. H. Song, K. Lombardi, and J. Arnoldy (2004), A reassessment of HO_x South Pole chemistry based on observations recorded during ISCAT 2000, *Atmospheric Environment*, *38*, 5451-5461.

Chen, G., D. Davis, J. Crawford, J. B. Nowak, F. Eisele, R. L. Mauldin, D. Tanner, M. Buhr, R. Shetter, B. Lefer, R. Arimoto, A. Hogan, and D. Blake (2001), An investigation of South Pole HO_x chemistry: Comparison of model results with ISCAT observations, *Geophysical Research Letters*, *28*, 3633-3636.

Cohen, R. C., K. K. Perkins, L. C. Koch, R. M. Stimpfle, P. O. Wennberg, T. F. Hanisco, E. J. Lanzendorf, G. P. Bonne, P. B. Voss, R. J. Salawitch, L. A. Del Negro, J. C. Wilson, C. T. McElroy, and T. P. Bui (2000), Quantitative constraints on the atmospheric chemistry of nitrogen oxides: An analysis along chemical coordinates, *Journal of Geophysical Research-Atmospheres*, *105*, 24283-24304.

Crawford, J. H., D. D. Davis, G. Chen, M. Buhr, S. Oltmans, R. Weller, L. Mauldin, F. Eisele, R. Shetter, B. Lefer, R. Arimoto, and A. Hogan (2001), Evidence for photochemical production of ozone at the South Pole surface, *Geophysical Research Letters*, *28*, 3641-3644.

Davis, D., G. Chen, M. Buhr, J. Crawford, D. Lenschow, B. Lefer, R. Shetter, F. Eisele, L. Mauldin, and A. Hogan (2004), South Pole NO_x chemistry: an assessment of factors controlling variability and absolute levels, *Atmospheric Environment*, *38*, 5375-5388.

Davis, D., J. B. Nowak, G. Chen, M. Buhr, R. Arimoto, A. Hogan, F. Eisele, L. Mauldin, D. Tanner, R. Shetter, B. Lefer, and P. McMurry (2001), Unexpected high levels of NO observed at South Pole, *Geophysical Research Letters*, *28*, 3625-3628.

Dibb, J. E., M. Arsenault, M. C. Peterson, and R. E. Honrath (2002), Fast nitrogen oxide photochemistry in Summit, Greenland snow, *Atmospheric Environment*, *36*, 2501-2511.

Dibb, J. E., L. G. Huey, D. L. Slusher, and D. J. Tanner (2004), Soluble reactive nitrogen oxides at South Pole during ISCAT 2000, *Atmospheric Environment*, *38*, 5399-5409.

Frey, M. M., R. W. Stewart, J. R. McConnell, and R. C. Bales (2005), Atmospheric hydroperoxides in West Antarctica: Links to stratospheric ozone and atmospheric oxidation capacity, *Journal of Geophysical Research-Atmospheres*, *110*, -.

Honrath, R. E., Y. Lu, M. C. Peterson, J. E. Dibb, M. A. Arsenault, N. J. Cullen, and K. Steffen (2002), Vertical fluxes of NO_x, HONO, and HNO_3 above the snowpack at Summit, Greenland, *Atmospheric Environment*, *36*, 2629-2640.

Hutterli, M. A., J. R. McConnell, G. Chen, R. C. Bales, D. D. Davis, and D. H. Lenschow (2004), Formaldehyde and hydrogen peroxide in air, snow and interstitial air at South Pole, *Atmospheric Environment*, *38*, 5439-5450.

Hutterli, M. A., J. R. McConnell, R. W. Stewart, H. W. Jacobi, and R. C. Bales (2001), Impact of temperature-driven cycling of hydrogen peroxide (H_2O_2) between air and snow on the planetary boundary layer, *Journal of Geophysical Research-Atmospheres*, *106*, 15395-15404.

Hutterli, M. A., R. Rothlisberger, and R. C. Bales (1999), Atmosphere-to-snow-to-firn transfer studies of HCHO at Summit, Greenland, *Geophysical Research Letters*, *26*, 1691-1694.

Jacobi, H. W., R. C. Bales, R. E. Honrath, M. C. Peterson, J. E. Dibb, A. L. Swanson, and M. R. Albert (2004), Reactive trace gases measured in the interstitial air of surface snow at Summit, Greenland, *Atmospheric Environment*, *38*, 1687-1697.

Jacobi, H. W., M. M. Frey, M. A. Hutterli, R. C. Bales, O. Schrems, N. J. Cullen, K. Steffen, and C. Koehler (2002), Measurements of hydrogen peroxide and formaldehyde exchange between the atmosphere and surface snow at Summit, Greenland, *Atmospheric Environment*, *36*, 2619-2628.

Jones, A. E., R. Weller, A. Minikin, E. W. Wolff, W. T. Sturges, H. P. McIntyre, S. R. Leonard, O. Schrems, and S. Bauguitte (1999), Oxidized nitrogen chemistry and speciation in the Antarctic troposphere, *Journal of Geophysical Research-Atmospheres*, *104*, 21355-21366.

Jones, A. E., R. Weller, E. W. Wolff, and H. W. Jacobi (2000), Speciation and rate of photochemical NO and NO_2 production in Antarctic snow, *Geophysical Research Letters*, *27*, 345-348.

Saiz-Lopez, A., J. M. C. Plane, and J. A. Shillito (2004), Bromine oxide in the mid-latitude marine boundary layer, *Geophysical Research Letters*, *31*, -.

Stohl, A., C. Forster, A. Frank, P. Seibert, and G. Wotawa (2005), Technical note: The Lagrangian particle dispersion model FLEXPART version 6.2, *Atmospheric Chemistry and Physics*, *5*, 2461-2474.

Sumner, A. L., and P. B. Shepson (1999), Snowpack production of formaldehyde and its effect on the Arctic troposphere, *Nature*, *398*, 230-233.

Sumner, A. L., P. B. Shepson, A. M. Grannas, J. W. Bottenheim, K. G. Anlauf, D. Worthy, W. H. Schroeder, A. Steffen, F. Domine, S. Perrier, and S. Houdier (2002), Atmospheric chemistry of formaldehyde in the Arctic troposphere at Polar Sunrise, and the influence of the snowpack, *Atmospheric Environment*, *36*, 2553-2562.

Yang, J., R. E. Honrath, M. C. Peterson, J. E. Dibb, A. L. Sumner, P. B. Shepson, M. Frey, H. W. Jacobi, A. Swanson, and N. Blake (2002), Impacts of snowpack emissions on deduced levels of OH and peroxy radicals at Summit, Greenland, *Atmospheric Environment*, *36*, 2523-2534.

CHAPTER 5

NITRIC ACID AND PERNITRIC ACID MEASUREMENTS OBTAINED FROM THE ANTCI 2003 FIELD CAMPAIGN AT THE SOUTH POLE

5.1 Introduction

In December of 2003 measurements of nitric acid (HNO_3) and pernitric acid (HO_2NO_2) were obtained with a chemical ionization mass spectrometer (CIMS) as a part of the Antarctic Tropospheric Chemistry Investigation (ANTCI) at the Amundsen-Scott Station. The South Pole provided an optimal location to examine the partitioning of reactive nitrogen species at cold temperatures over wide range of NO_x ($NO+NO_2$) concentrations. In addition the extensive suite of chemical species obtained during ANTCI allowed for highly constrained predictions of short lived species such as OH, HO_2, and HO_2NO_2. This provides a further test of our understanding of photochemistry in polar regions and our ability to predict reactive nitrogen partitioning.

Formation of nitric and pernitric acid can provide terminal steps for both HO_x ($OH + HO_2$) and NO_x radical chains. Since photolytic and oxidative lifetimes for nitric acid are long (~1-2 weeks) nitric acid formed in the gas phase is assumed to be lost to deposition. In contrast the lifetime of pernitric acid (τ_{HNO4}) is much shorter (hours) and highly dependent on temperature. At warmer temperatures (>245K) thermal decomposition of HO_2NO_2 becomes the largest loss term. Thermal decomposition of

pernitric acid reforms HO_2 and NO_2 radicals. At lower temperatures photolysis of HO_2NO_2 plays an increasingly important role in regenerating HO_x and NO_x radicals. Oxidation of pernitric acid will also become more important in determining the lifetime of pernitric acid at lower temperatures. Oxidation of HO_2NO_2 will regenerate NO_x, but serves as a HO_x termination step. At lower temperatures pernitric acid can also be a loss term for both families by uptake on a surface [*Li et al.,* 1996; *Diehl et al.,* 1995; *Abbatt,* 1997; *Zondlo et al.,* 1997].

In the last decade there has been a series of field campaigns that have explored photochemistry in the upper troposphere and lower stratosphere. At these altitudes it is cold enough that thermal decomposition does not dominate the lifetime of pernitric acid. Budget analysis of HO_x conducted by *Jaegle et al.,* [2001] suggests that formation of pernitric acid and nitric acid were large, if not dominant, loss terms. The magnitude of each was dependent on the NO_x mixing ratios. Briefly, at lower NO_x mixing ratios oxidation of HO_2NO_2 was expected to be the dominant HO_x loss term and formation of nitiric acid would assume a larger role with increasing NO_x. At the highest NO_x concentrations, formation of nitric acid was expected to become the dominant HO_x loss term. This was due to increased conversion of HO_2 to OH by high NO mixing ratios. There were, however, no measurements of HO_2NO_2 during any of the high altitude field campaigns to confirm this hypothesis. Furthermore, measured concentrations of HO_2 during the campaigns were much higher than predicted [*Faloona et al.,* 2000].

The ISCAT 2000 conducted at the South Pole was the only campaign where direct measurements of pernitric acid have been obtained [*Slusher et al.,* 2002]. Measured concentrations for pernitric acid ranged from <5-54 pptv (mean 25 pptv,

median 24 pptv) while nitric acid ranged from <5-68 pptv (mean and median 22pptv). Measurements were obtained during the month of December, during a period of continuous sunlight, with temperatures ranging from -31.5C to -23.6C. The mean NO and ozone mixing ratios were 115 pptv and 31 ppbv respectively over the measurement period. The data set obtained during ANTCI 2003 was collected at the same site for a longer time period and encompassed a wider range of temperatures and NO_x mixing ratios

5.2 Methods

Ambient measurements of pernitric acid, nitric acid, and sulfur dioxide were obtained using a CIMS instrument located 10 m above the snowpack in the Atmospheric Research Observatory during the ANTCI 2003 field campaign. The experimental set up is detailed in section 2.3 of chapter 2. The instrument was situated facing prevailing winds from the clean air sector.

5.2.1 Ancillary Measurements

Concurrent measurements of NO, O_3, CH_2O, H_2O_2, HONO, CH_4, CO, temperature, dew point, and actinic flux were obtained during the ANTCI 2003 field campaign. NO measurements were obtained at the ARO and by chemiluminescence [*Davis et al.,* 2004]. Ozone values were obtained by UV absorption [*Oltmans and Kohmyr*, 1976]. Formaldehyde and hydrogen peroxide were scrubbed from the atmosphere and measured by fluorescence spectrometry in the aqueous phase as described in *Hutterli et al.,* [1999]. Methane and CO data were obtained from flask

samples collected by NOAA CMDL at the ARO and from grab samples collected by UCI. Nitrous and nitric acid measurements were collected with a mist chamber coupled to an ion chromatograph as detailed in *Dibb et al.,* [1998]. Dewpoint and temperature were obtained from the meteorological station at the South Pole. Actinic Fluxes were obtained from an ultraviolet spectroradiometer located in the ARO and maintained by Biospherical Instruments, Inc.

5.2.2 Model

A highly constrained 0-D steady state photochemical model was employed to predict the concentrations of short lived species. The model was constrained to measured values of NO, O_3, CH_2O, H_2O_2, CH_4, CO, dew point, and temperature. A median deposition rate of $3x10^{-5}$ s^{-1} for HNO_3 was incorporated into the model. The deposition rate was derived from the measurements of HNO_3 and the calculated production rate of nitric acid. The estimated deposition rate for HO_2NO_2 was similar in magnitude to the nitric acid deposition rate. However, a bimodal distribution dependent on ΔTemp (see below) was incorporated to calculate pernitric concentrations.

5.3 Results

Measurements of nitric acid and pernitric acid were collected from November 30 to December 31 during the ANTCI 2003 field campaign. The median HNO_3 mixing ratio was 74 pptv (mean = 90 pptv) for the measurement period with a standard deviation of 75 pptv. The median HNO_4 mixing ratio over the measurement period was 41 pptv (mean = 40 pptv) with a standard deviation of 15 pptv. A time series of both measurements along with nitric oxide and ΔTemp is provided in figure 5.1.

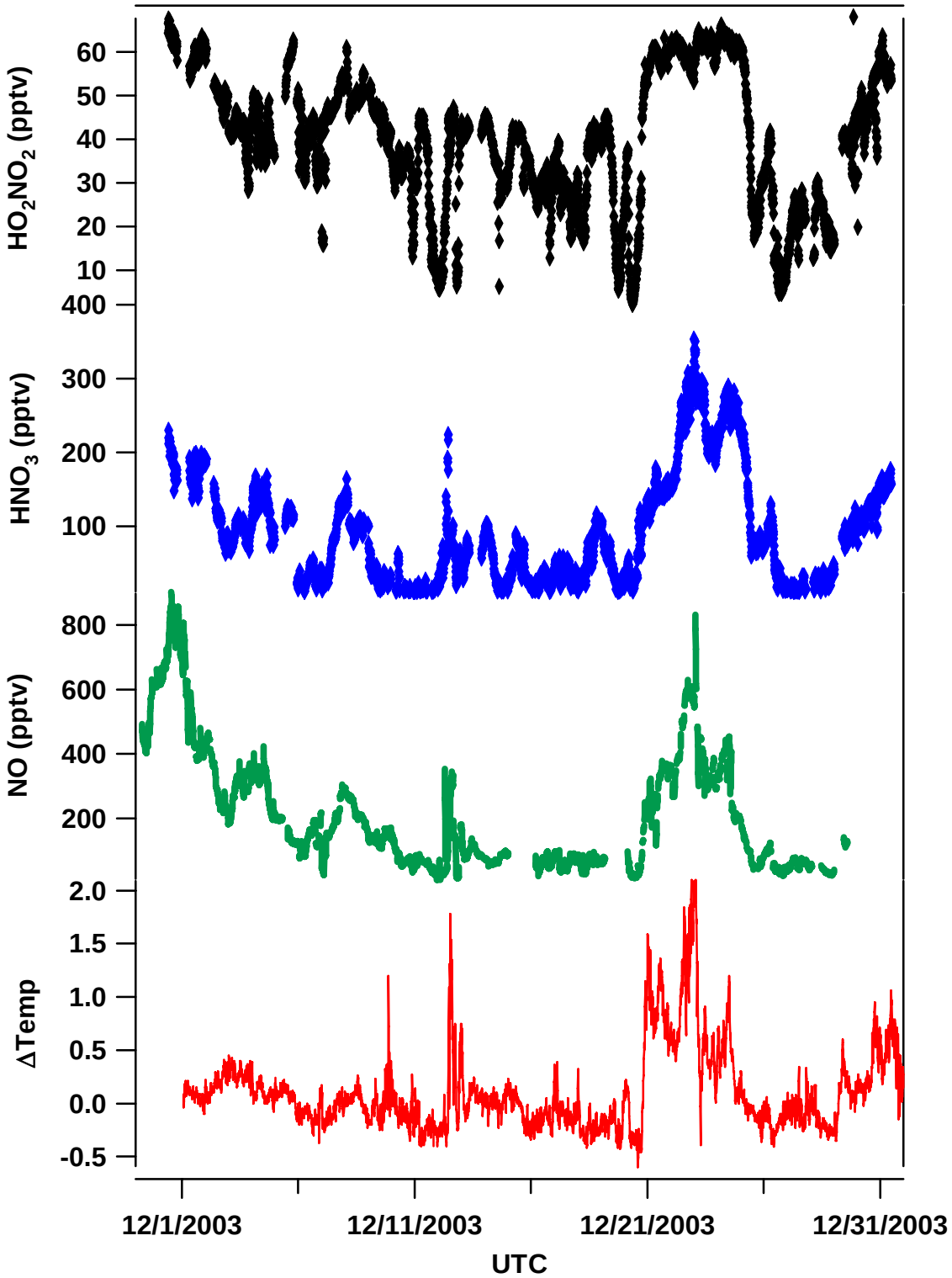

Figure 5.1 Time series for measurements of HNO_4 (black diamonds), HNO_3 (blue diamonds), NO (green line) and ΔTemp (red line) for the ANTCI 2003 campaign

ΔTemp is the difference between the temperature at 22 meters and at 2 meters. A positive value indicates a temperature inversion and infers an increased level of atmospheric stability. Table 5.1 shows that median values obtained for HNO_3 and HNO_4 during ANTCI 2003 were significantly higher than the median values collected during the ISCAT 2000 field campaign [*Huey et al.,* 2004; *Slusher et al.,* 2002]. The median mixing ratio of NO for ANTCI 2003 231 pptv (mean = 282 pptv) was also much higher than during the 2000 season when the median mixing ratio was 89 pptv [*Davis et al.,* 2004]. However, the NO concentrations from the ANTCI 2003 campaign are of similar magnitude to the median mixing ratio of 225 pptv observed during the ISCAT 1998 field campaign [*Davis et al.,* 2001].

Table 5.1 Comparison of median mixing ratios for HNO_3, HNO_4, and NO from ANTCI 2003 and ISCAT 2000

Species	ANTCI 2003	ISCAT 2000
HNO_3	74	22
HNO_4	41	24
NO	231	89

Predicted mixing ratios of NO_2 were calculated from observed NO, O_3, and predicted HO_2 and used to calculate production of HNO_3 and HO_2NO_2. Production of nitric acid was assumed to be from the reaction of OH and NO_2. HNO_3 production from hydrolysis of N_2O_5 was excluded as a loss term since NO_3 concentrations were expected to be negligible in the continuous sunlight encountered during the ANTCI 2003 campaign. Another loss term was required to bring model predictions into agreement with measured values. During the ISCAT 2000 the additional loss was attributed to deposition to the snow surface due since aerosol particle concentration was attenuated in this environment [*Huey et al.,* 2004]. The magnitude of deposition to the snow was

initially derived from the slope of the correlation between observed HNO_3 mixing ratios and the calculated hourly production of HNO_3. This led to a median observed lifetime of 9.3 hours (Figure 5.2).

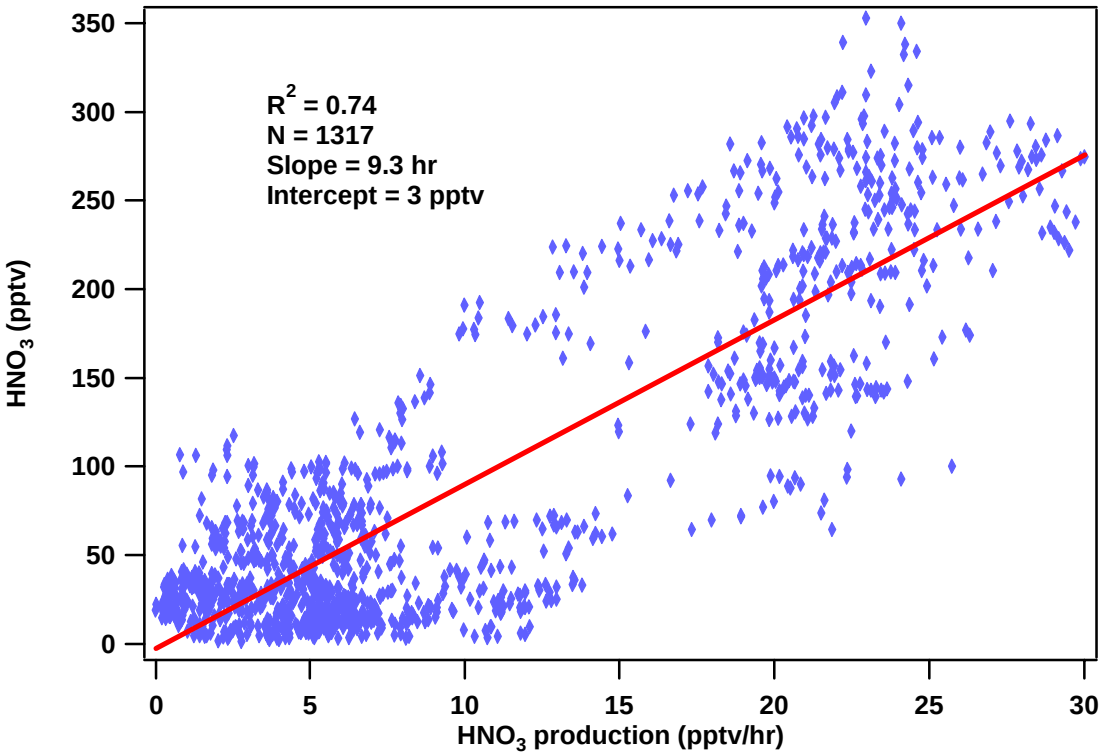

Figure 5.2 Comparison of HNO_3 measurements to hourly production

Deposition was also calculated from steady state and constrained to measured nitric acid values.

$$Deposition = \frac{k_{OH+NO_2}[OH][NO_2]}{[HNO_3]_{measured}} - k_{OH+HNO_3}[OH] - j_{HNO_3}$$

A temperature dependence for the deposition rate of pernitric acid was suggested in *Slusher et al.*, [2002] for the ISCAT 2000 data. This dependence was not observed in the ANTCI 2003 nitric acid data. However, there exists a bimodal distribution in nitric acid deposition when compared to ΔTemp. When ΔTemp was less than 0.2 C the median

deposition rate was $3.6x10^{-5}$ s^{-1}, whereas when ΔTemp is greater than 0.2C the median deposition rate was $1.8x10^{-5}$ s^{-1}. This suggests that the rate of deposition was attenuated during periods characterized by strong temperature inversions.

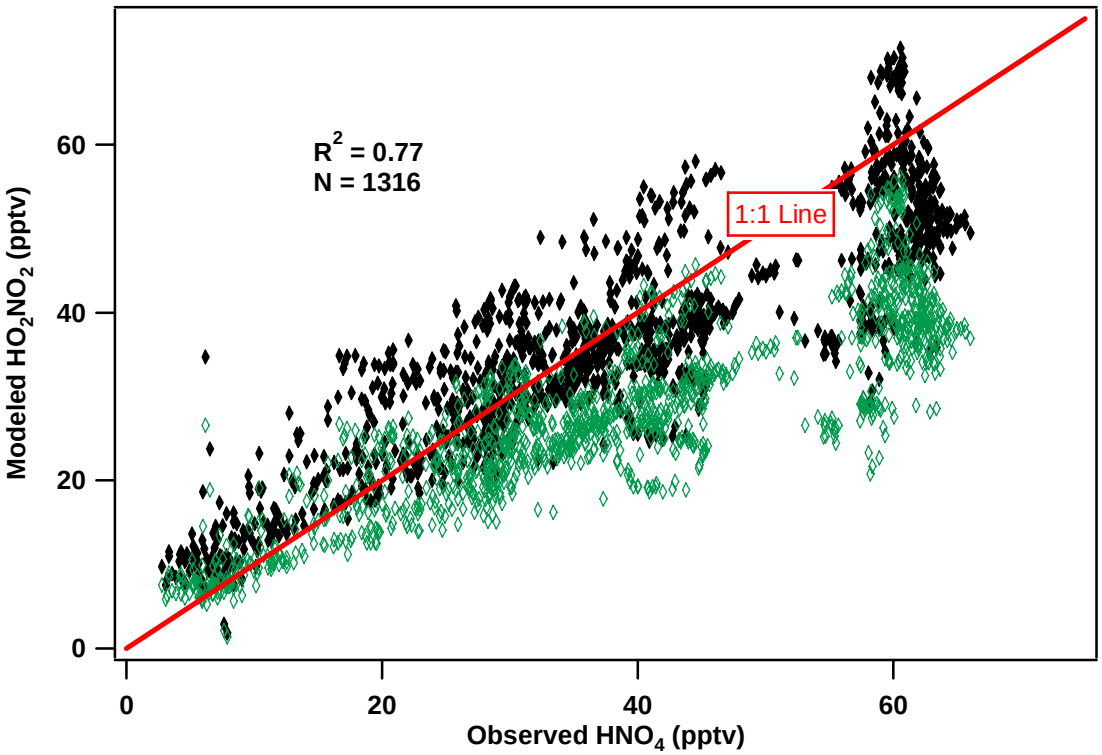

Figure 5.3 Scatter plot of predicted HNO_4 to measured HNO_4. The solid black diamonds are predicted values obtained using the thermal decomposition from *Gierczak et al,* [2005]. The open green diamonds are predicted values obtained from *Sander et al,* [2006].

Measurements of pernitric acid were also compared to predicted values. The deposition rates derived for nitric acid as a function of ΔTemp were included as loss terms for pernitric acid. A comparison was run with the model using two different thermal decomposition rates. The first was the recommended value from the JPL Chemical Kinetics and Photochemical Data for use in Atmospheric Studies [*Sander et al.,* 2006]. The other decomposition rate was obtained from *Gierczak et al.,* [2005]. The comparison was constrained to measured values obtained when temperatures were greater

than -28C. This was due to limited measurements of other chemical species required for model calculations. The model comparisons occur in the temperature range where thermal decomposition plays a significant role in determining the pernitric lifetime. The correlations between measured and observed pernitric values (Figure 5.3) for both model runs were nearly identical. The ratio of modeled (M) to observed (O) values were also compared for the two rates. The median M/O using *Sander et al.* [2006] was 0.73. The median M/O improved to 0.96 using the *Gierczak et al.* [2005] thermal decomposition rate. The *Gierczak at al.* [2005] decomposition rate was used for the time series comparing model predictions to observed values of pernitric acid (Figure 5.4).

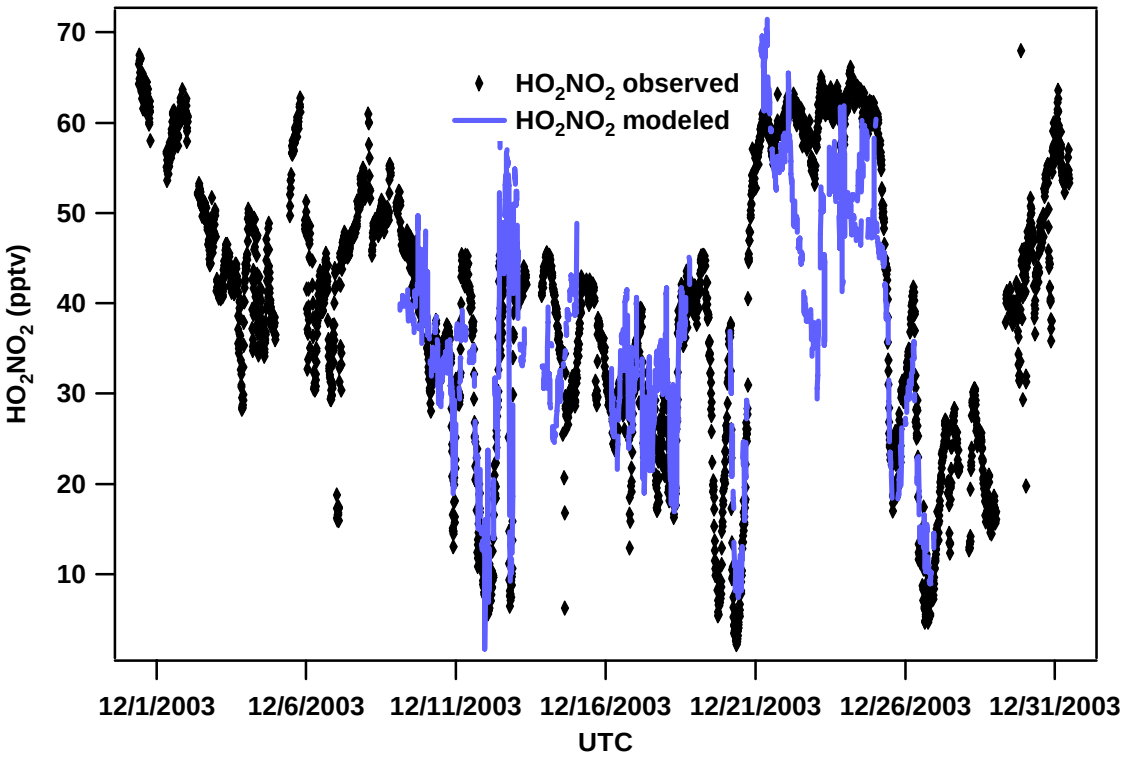

Figure 5.4 Time Series of modeled and observed HNO_4 mixing ratios

Measurements of sulfur dioxide were also collected during ANTCI 2003. The median and mean mixing ratios of SO_2 were 10 pptv with a standard deviation of 2.4 pptv. There was little temporal variation except on December 12 when mixing ratios spiked to 250 pptv. This high reading was accompanied by stagnant conditions and was attributed to pollution from the station generators. The SO_2 measurement was in good agreement with the median 16.5 pptv value collected during ISCAT 2000 [*Huey et al.,* 2004]. It should be noted that the median SO_2 mixing ratio obtained in 2000 was an upper limit since there was no background method available for the SO_2 measurement.

5.4 Discussion

The effect of NO_x on HO_x chemistry was evident in production of both HNO_3 and HO_2NO_2. In the lowest NO_x regime (less than 200 pptv) the rates of production for HNO_3 and HNO_4 rose linearly with increasing NO_x (Figure 5.5). The production rate of pernitric acid (Figure 5.5, lower panel) was twice that of nitric acid (Figure 5.5, upper panel) in the low NO_x regime. Production of HO_2NO_2 achieves a maximum around 300 pptv and then steadily decreases with increasing NO_x. Production of HNO_3 continued to increase linearly until NO_x levels were 400 pptv. Hourly production of HO_2NO_2 and HNO_3 were of similar magnitude when NO_x concentrations rose to 400 pptv. The change in both production rates was due to increased cycling of HO_2 to OH by NO. Nitric acid production continued to increase with NO_x levels above 400 pptv but the relationship became non linear. The change in HNO_3 production was due to decreasing hydroxyl radical concentrations at high NO_x mixing ratios.

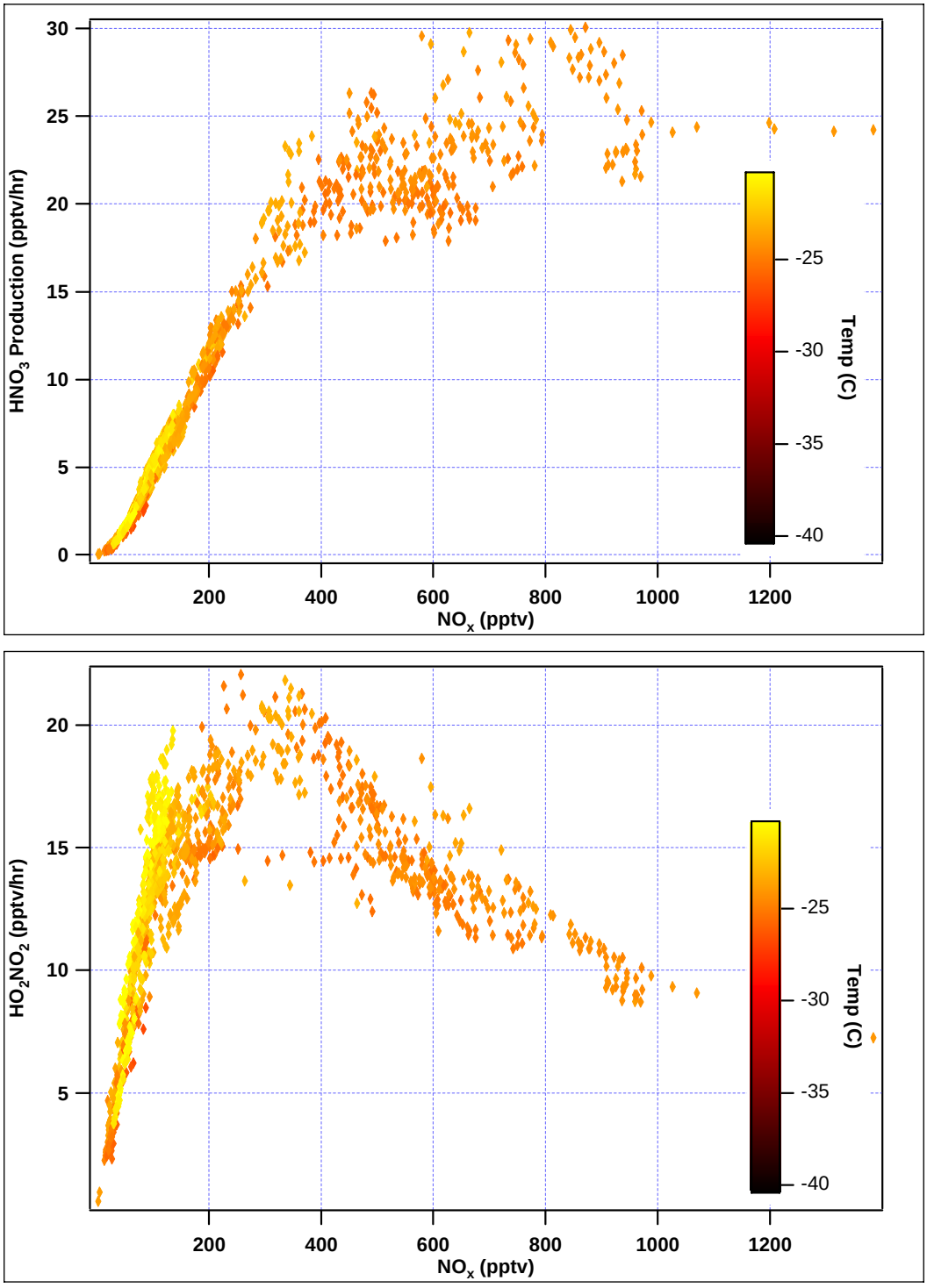

Figure 5.5 Production of HNO_3 (upper panel) and HNO_4 (lower panel) as a function of NO mixing ratios. Both graphs are color coded to temperature.

Overall the dependence of pernitric production with respect to NO_x was also evident in the measured values HO_2NO_2. In the lowest NO_x regime HO_2NO_2 measurements track pernitric acid production very well. The lowest NO_x mixing ratios generally occur at the warmest temperatures and shortest pernitric lifetimes. At the lower temperatures found at high NO_x mixing ratios, production of pernitric acid was expected to drop off due to lower concentrations of HO_2 radicals (Figure 5.6). However, the lifetime of pernitric acid increased due to attenuation of thermal decomposition. This helped to explain why measured HO_2NO_2 concentrations remain elevated at high NO_x mixing ratios even though production was reduced. The lhigh measured pernitric values also occurring at the highest NO_x conectrations also occurred during high ΔTemp.

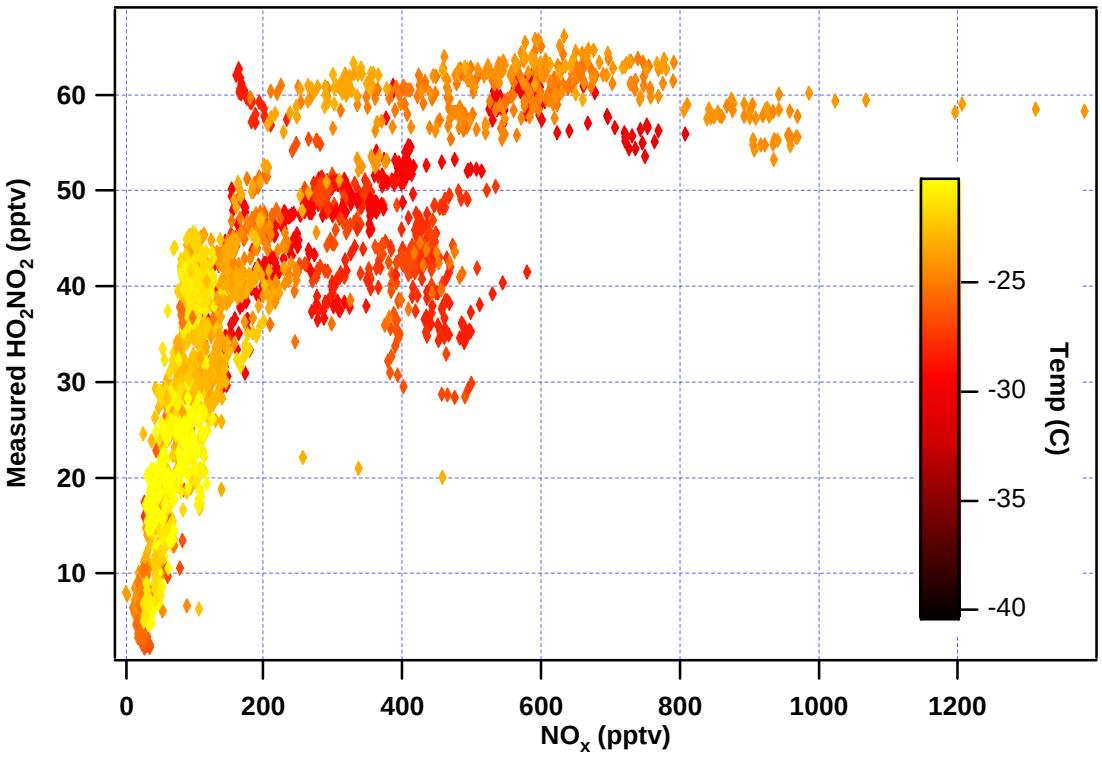

Figure 5.6 Measured HNO_4 as a function of NO mixing ratios. The plot is color coded to temperature

5.4.1 Partitioning of Reactive Nitrogen Species

The NO_x lifetime was determined by formation of nitric acid and deposition of pernitric acid. The NO_2 mixing ratio was calculated to determine the NO_x lifetime.

$$\tau_{NO_x} = \frac{1 + \frac{[NO]}{[NO_2]}}{k_{OH+NO_2}[OH] + k_{HO_2+NO_2}[HO_2]\left(\frac{k_{Deposition}}{k_{HO_2NO_2+M} + j_{HO_2NO_2} + k_{OH+HO_2NO_{24}}[OH] + k_{Deposition}}\right)}$$

The median NO_x lifetime at the South Pole was predicted to be13.5 hours (mean = 15.6 hours). If the NO_x, HO_x, HNO_3, and HO_2NO_2 concentrations can be determined then the speciation of reactive nitrogen species can be derived. HO_2 concentrations were not available and OH measurements were limited, so both were calculated from the 0-D steady state model. We have confidence in the predicted HO_x values used for the ANTCI 2003 field campaign since the agreement between the model and measured HO_x was excellent for the Summit field campaigns (Chapters 3 and 4). However, the deposition rate for HNO_3 and HO_2NO_2 has varied from between ISCAT 2000 (median = 3.1 hours) and ANTCI 2003 (median 9.1 hours). For the ANTCI 2003 field campaign the variable deposition rate based on ΔTemp was employed. Nitric acid and pernitric acid were responsible for ~60% and ~40% of the NO_x loss respectively (Figure 5.7)

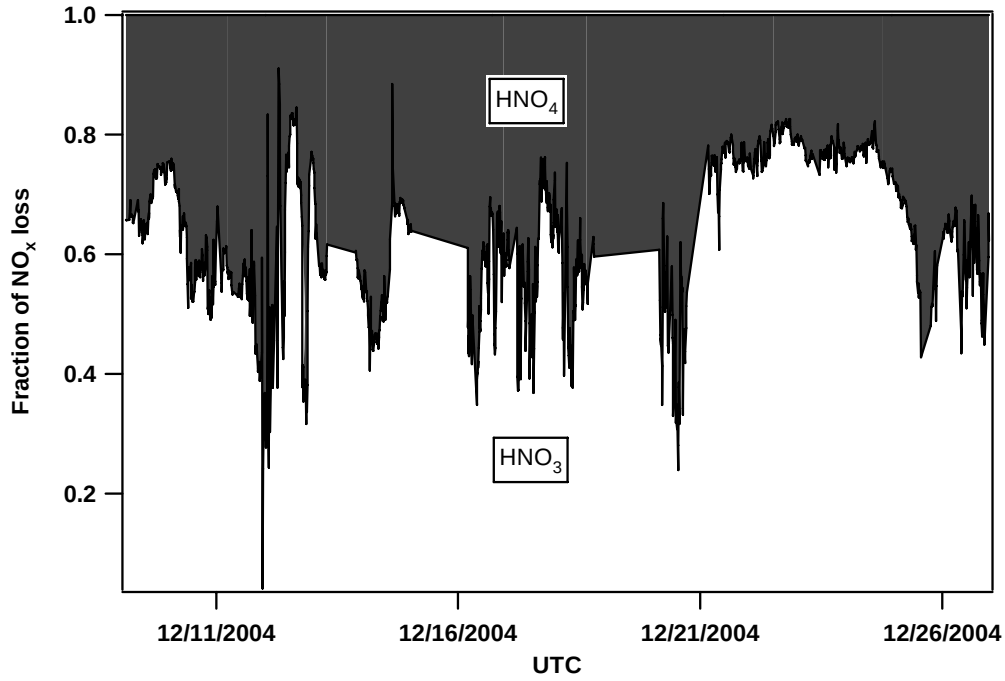

Figure 5.7 Fraction of NO_x loss due to HNO_3 and HNO_4 during ANTCI 2003

Reactive nitrogen partitioning can also be determined at other polar sites as well. Although there are no pernitric measurements at Summit the 0-D model has shown that it can reproduce observed HO_2NO_2 concentrations. In table 5.2 NO_x losses due to partitioning between reactive nitrogen species has been calculated for both Summit missions and the ANTCI 2003 field campaigns. Because there exists a wide range in deposition rates between ISCAT 2000 and ANTCI 2003, partitioning has been calculated with deposition lifetimes of 3 hours and 10 hours.

Table 5.2 Percent loss of NO_x due to Reactive Nitrogen partitioning

Species	Summit summer 2003	Summit spring 2004	ANTCI 2003
10 hour Deposition Rate			
HNO_3	56%	13%	65%
HO_2NO_2	46%	87%	35%
3 hour Deposition Rate			
HNO_3	32%	8%	44%
HO_2NO_2	68%	92%	56%

NO_x mixing ratios at the South Pole were much higher than at other high latitude sites (see Tables 1.1,1.2,1.3). For example at Summit, Greenland, the average NO_x mixing ratios ranged form 25-56 pptv. From NO_x mixing ratios obtained during the spring 2004 field campaign at Summit ~90% of the NO_x loss was attributed to deposition of pernitric acid. The NO_x loss during the summer 2003 Summit campaign was roughly split between nitric and pernitric acid.

Isotopic analysis of nitrate ions (NO_3^-) in the snowpack has been performed at Summit, Greenland, to determine their source [*Hastings et al.,* 2004]. Seasonal variations in the observed NO_3^- observations were attributed to the mechanism by which HNO_3 was formed (i.e. gas phase or heterogeneous). Since pernitric was expected to account for almost half of the NO_x in the summer and almost all of the NO_x loss in the spring, it help explain the seasonal variance of the isotopic profile in the nitrate found at the Summit and other coring sites.

5.5 Summary

Measurements of nitric and pernitric acid collected during ANTCI 2003 provide a test of the photochemistry in a cold environment over a wide range of NO mixing ratios. Comparison of nitric acid production indicates that the lifetime of nitric acid (9.3 hours) at the South Pole is dominated by deposition. This suggests that nitric acid observed at the South Pole was generated locally.

The deposition rate for nitric acid was assumed to be the similar for pernitric acid and incorporated into the photochemical model. Model predictions of pernitric acid are

in very good agreement with measured values ($R^2 = 0.77$). Model to observed ratios are also excellent (median M/O =0.96) if the thermal decomposition rate suggested by *Gierczak et al.* [2005] was employed.

During the ANTCI 2003 campaign 65% of the NO_x loss is due to formation of nitric acid and the remaining 35% is due to deposition of pernitric acid. Even in the high NO_x environment encountered at the South Pole, HO_2NO_2 was a substantial component of the reactive nitrogen budget. Pernitric acid was expected to be the dominant reactive nitrogen species at other high latitude sites where NO_x mixing ratios are much lower. Pernitric acid may very well have an impact on the isotopic ratio of NO_3^- in the snowpack and should be included in the interpretation of ice core records at Summit and other polar coring sites.

5.6 References

Abbatt, J. P. D. (1997), Interaction of HNO_3 with water-ice surfaces at temperatures of the free troposphere, *Geophysical Research Letters*, *24*, 1479-1482.

Chen, G., D. Davis, J. Crawford, L. M. Hutterli, L. G. Huey, D. Slusher, L. Mauldin, F. Eisele, D. Tanner, J. Dibb, M. Buhr, J. McConnell, B. Lefer, R. Shetter, D. Blake, C. H. Song, K. Lombardi, and J. Arnoldy (2004), A reassessment of HO_x South Pole chemistry based on observations recorded during ISCAT 2000, *Atmospheric Environment*, *38*, 5451-5461.

Davis, D., G. Chen, M. Buhr, J. Crawford, D. Lenschow, B. Lefer, R. Shetter, F. Eisele, L. Mauldin, and A. Hogan (2004), South Pole NO_x chemistry: an assessment of factors controlling variability and absolute levels, *Atmospheric Environment*, *38*, 5375-5388.

Davis, D., J. B. Nowak, G. Chen, M. Buhr, R. Arimoto, A. Hogan, F. Eisele, L. Mauldin, D. Tanner, R. Shetter, B. Lefer, and P. McMurry (2001), Unexpected high levels of NO observed at South Pole, *Geophysical Research Letters*, *28*, 3625-3628.

Dibb, J. E., R. W. Talbot, J. W. Munger, D. J. Jacob, and S. M. Fan (1998), Air-snow exchange of HNO_3 and NO_y at Summit, Greenland, *Journal of Geophysical Research-Atmospheres*, *103*, 3475-3486.

Diehl, K., S. K. Mitra, and H. R. Pruppacher (1995), A Laboratory Study of the Uptake of HNO_3 and HCl Vapor by Snow Crystals and Ice Spheres at Temperatures between 0-Degrees-C and -40-Degrees-C, *Atmospheric Environment*, *29*, 975-981.

Faloona, I., D. Tan, W. H. Brune, L. Jaegle, D. J. Jacob, Y. Kondo, M. Koike, R. Chatfield, R. Pueschel, G. Ferry, G. Sachse, S. Vay, B. Anderson, J. Hannon, and H. Fuelberg (2000), Observations of HO_x and its relationship with NO_x in the upper troposphere during SONEX, *Journal of Geophysical Research-Atmospheres*, *105*, 3771-3783.

Gierczak, T., E. Jimenez, V. Riffault, J. B. Burkholder, and A. R. Ravishankara (2005), Thermal decomposition of HO_2NO_2 (peroxynitric acid, PNA): Rate coefficient and determination of the enthalpy of formation, *Journal of Physical Chemistry A*, *109*, 586-596.

Hastings, M. G., E. J. Steig, and D. M. Sigman (2004), Seasonal variations in N and O isotopes of nitrate in snow at Summit, Greenland: Implications for the study of nitrate in snow and ice cores, *Journal of Geophysical Research-Atmospheres*, *109*, -.

Huey, L. G., D. J. Tanner, D. L. Slusher, J. E. Dibb, R. Arimoto, G. Chen, D. Davis, M. P. Buhr, J. B. Nowak, R. L. Mauldin, F. L. Eisele, and E. Kosciuch (2004), CIMS measurements of HNO_3 and SO_3 at the South Pole during ISCAT 2000, *Atmospheric Environment*, *38*, 5411-5421.

Hutterli, M. A., R. Rothlisberger, and R. C. Bales (1999), Atmosphere-to-snow-to-firn transfer studies of HCHO at Summit, Greenland, *Geophysical Research Letters*, *26*, 1691-1694.

Jaegle, L., D. J. Jacob, W. H. Brune, and P. O. Wennberg (2001), Chemistry of HO_x radicals in the upper troposphere, *Atmospheric Environment*, *35*, 469-489.

Jaegle, L., D. J. Jacob, Y. Wang, A. J. Weinheimer, B. A. Ridley, T. L. Campos, G. W. Sachse, and D. E. Hagen (1998), Sources and chemistry of NO_x in the upper troposphere over the United States, *Geophysical Research Letters*, *25*, 1705-1708.

Li, Z. J., R. R. Friedl, S. B. Moore, and S. P. Sander (1996), Interaction of peroxynitric acid with solid H_2O ice, *Journal of Geophysical Research-Atmospheres*, *101*, 6795-6802.

Oltmans, S., and W. Komhyr (1976), Surface Ozone in Antarctica, *Transactions-American Geophysical Union*, *57*, 603-603.

Sander, S.P., R.R. Friedl, A.R. Ravishankara, D.M. Goldem, C.E. Kolb, M.J. Kurylo, R.E. Huie, V.L. Orkin, M.J. Molina, G.K. Moortgat, B.J. Finlayson-Pitts, Chemical kinetics and photochemical data for use in atmospheric studies, *JPL Publication, 06-02,* 2006.

Slusher, D. L., L. G. Huey, D. J. Tanner, G. Chen, D. D. Davis, M. Buhr, J. B. Nowak, F. L. Eisele, E. Kosciuch, R. L. Mauldin, B. L. Lefer, R. E. Shetter, and J. E. Dibb (2002), Measurements of pernitric acid at the South Pole during ISCAT 2000, *Geophysical Research Letters*, *29*, -.

Slusher, D. L., S. J. Pitteri, B. J. Haman, D. J. Tanner, and L. G. Huey (2001), A chemical ionization technique for measurement of pernitric acid in the upper troposphere and the polar boundary layer, *Geophysical Research Letters*, *28*, 3875-3878.

Yang, J., R. E. Honrath, M. C. Peterson, J. E. Dibb, A. L. Sumner, P. B. Shepson, M. Frey, H. W. Jacobi, A. Swanson, and N. Blake (2002), Impacts of snowpack emissions on deduced levels of OH and peroxy radicals at Summit, Greenland, *Atmospheric Environment*, *36*, 2523-2534.

Zondlo, M. A., S. B. Barone, and M. A. Tolbert (1997), Uptake of HNO_3 on ice under upper tropospheric conditions, *Geophysical Research Letters*, *24*, 1391-1394.

CHAPTER 6

CONCLUSIONS

6.1 Photochemistry at High Latitudes

Recent high latitude field campaigns had indicated that photochemistry was much more involved than initially thought [*Dominé and Shepson,* 2002]. High levels of NO_x and HO_x precursors had led to predicted HO_x values at concentrations that were comparable to or greater than measured values in other remote regions (see Tables 1.1, 1.2, 1.3). OH measurements obtained during the ISCAT 1998, ISCAT 2000, and TOPSE field campaigns confirmed that photochemistry was indeed active in this environment (see section 1.3.5).

6.1.1 Comparison of Field Campaign Environments

The summer 2003 field campaign at Summit, Greenland, provided the first in situ measurements of hydroxyl and peroxy radicals in the Arctic boundary layer. The suite of chemical species measured allowed for a test of current understanding of photochemistry at this site. Although previous measurements were obtained at the South Pole there are several differences between the two sites. The South Pole is colder and drier than Summit, Greenland. The NO_x levels at the South Pole are higher, often by an order of magnitude than at other sites. At the South Pole NO_x chemistry was so large that formation of nitric and pernitric acid were the dominant HO_x loss terms in that environment [*Chen et al.,* 2004]. NO_x concentrations were also high enough to make

methane oxidation a significant HO_x source [*Chen et al.*, 2004]. Primary production from ozone was attenuated at the South Pole and the largest HO_x sources were emissions of HO_x precursors from the snowpack. TOPSE measurements were obtained at latitudes similar to Summit, Greenland in the northern hemisphere. However, these measurements were obtained at altitudes above the polar boundary layer. The TOPSE measurements were not expected to be impacted by emissions from the snowpack.

6.1.2 Summer 2003 Summit Field Campaign

In contrast to the South Pole, the environment at Summit had much higher dew points and ozone concentrations were larger (O_3 ~50 ppbv at Summit, O_3 ~ 30 ppbv at South Pole). Primary production from photolysis of ozone was the largest HO_x source at Summit during the 2003 campaign.

1. $O_3 + h\nu \rightarrow O(^1D)$
2. $O(^1D) + H_2O \rightarrow 2OH$

Photolysis of H_2O_2 and CH_2O also make significant contributions to the HO_x budget during the summer.

3. $H_2O_2 + h\nu \rightarrow 2OH$
4. $CH_2O + h\nu + 2O_2 \rightarrow 2HO_2 + CO$

However, model predictions indicate that gas phase photochemistry was responsible for half of the hydrogen peroxide observed (Reaction 5). Furthermore, almost two-thirds of the observed formaldehyde was due to methane oxidation (see section 1.2.3).

The primary HO_x sinks during the summer were reactions of HO_x radicals with themselves.

5. $HO_2 + HO_2 \rightarrow H_2O_2 + O_2$

6. $HO_2 + OH \rightarrow H_2O + O_2$

Methane oxidation was responsible for most of the remaining HO_x losses. In stark contrast to the South Pole, formation of nitric acid and deposition of pernitric acid played a small role.

Model predictions were in excellent agreement with measured values (R^2 = 0 .83, M\O = 1.06), which is an indication that we have a firm grasp on the HO_x sources and sinks at Summit. There were still some unresolved questions from the summer field campaign. The role of HONO was called into question during the ISCAT 2000 budget analysis [*Chen et al.,* 2004]. Incorporation of measured HONO values led to ~20 percent increase in the predicted HO_x concentrations. This was well within the estimated uncertainty (~35%) of the measurement. Therefore the role of HO_x production from photolysis of HONO remained unresolved, but we determined that HONO was not an overwhelming source at Summit during the summer.

7. $HONO + h\nu \rightarrow OH + NO$

The agreement between modeled and observed OH was not as robust. Measured hydroxyl concentrations were a factor of two or more higher than model predictions. Inclusion of HONO increased the predicted OH concentration by ~20%, but it was not enough to resolve the difference. This indicated that there may a HO_2/OH partitioning mechanism that is unaccounted for. Meteorology appeared to play a role in the elevated OH observations. During calm clear conditions found at the end of the measurement period measured OH concentrations and predicted values came into reasonable agreement if HONO photolysis was included. In contrast, the perturbation of HO_2/OH ratio was

greatest during high wind events. This led to speculation that halogens may be playing a role at Summit. Halogen chemistry has been well documented in ozone depletion events at coastal sites such as Alert, Nunavut, Canada (see section 1.3.2). Reactive halogen species may have been rapidly transported to Summit with marine air coming from a low pressure system located in the Irminger Sea during the high wind period. There was also evidence of halogen chemistry occurring within the firn, particularly ozone depletion. Ventilation of the firn during the high wind event might have also played a role. Unfortunately, there were no direct measurements of reactive halogen species (i.e., BrO, IO) at Summit. There were, however, ancillary measurements (i.e., soluble bromide, MeBr, EtBr, MeI, ozone) that suggest that reactive halogen species are present.

6.1.3 Spring 2004 Summit field campaign

The spring field campaign allowed us to look at photochemistry in an environment where conditions were closer to what was observed at the South Pole. In particular, primary production was expected to be limited due to lower dew points and reduced insolation. In early spring noontime measured HO_2+RO_2 concentrations were a factor of 7 lower than the summer values, and noontime OH measured values were a factor of 20 lower than observed summer values. The spring was a time of rapidly changing insolation and dew points. By the end of the spring noontime measured HO_2+RO_2 and OH values had increased to within 50% and 25% of the observed summer values respectively (see Table 4.1).

During the spring snow emission did indeed play a larger role in the HO_x budget. In early spring photolysis of ozone was responsible for less than a quarter of the HO_x

production; whereas photolysis of hydrogen peroxide and formaldehyde contributed ~35% and ~40% respectively. Furthermore, the majority of observed H_2O_2 (~80%) and CH_2O (`60%) could be attributed to snow sources. In early spring snowpack emission was responsible for over half of the observed HO_x. By late spring things were starting to look like summer and snowpack emission was estimated to be responsible for a third of the HO_x budget. The HONO measurement came into question during the spring. If measured HONO was incorporated into the model than production from HONO was estimated to account for ~70% of the budget. This led to model over predictions for both HO_2+RO_2 and OH by more than a factor of two. HONO measurements were excluded from the HO_x budget. We conclude that the soluble nitrite (NO_2^-) measurement does measure HONO exclusively, but may also contain other soluble nitrogen species such as pernitric acid.

The sinks for HO_x were different for Summit in the spring, particularly in the early period. HO_x radicals still play a large role at Summit (~45%) during the early spring but they are matched in magnitude by deposition of pernitric acid. This was due to the increased HO_2NO_2 lifetime at colder temperatures. The remainder of the HO_x was mostly attributed to methane oxidation (~8%) and nitric formation (>2%). OH levels were in better agreement with the observed spring values (M/O = 0.74) and close to the estimated uncertainty of the OH measurement (~25). This suggests that the suspected HO_2 to OH cycling mechanism (halogens?) was suppressed in the spring.

6.1.4 ANTCI 2003 Field Campaign

Reactive nitrogen partitioning was derived from the measurements of nitric and pernitric acid obtained at the South Pole during the ANTCI 2003 field campaign. Model agreement with measured HO_2NO_2 values were robust ($R^2 = 0.77$, N/O =0.98) if the thermal decomposition rate calculated from *Gierczak et al.* [2005] was employed. Although measured HO_2 values were absent and OH measurements were limited, we have confidence in the predicted values due to the model agreement with measured values obtained during the Summit field campaigns. Particularly the spring campaign where temperatures were closer to values found at the South Pole.

Reactive nitrogen speciation again was found to be strongly dependent on NO_x concentrations, which much higher than observed at Summit. This was in accord with the previous ISCAT 2000 mission at the South Pole [*Chen et al.*,2004; *Huey et al.,* 2004; *Slusher et al.,* 2002]. The predicted HO_2NO_2 concentration was dependent on a deposition lifetime (9.3 hours) obtained from the measured HNO_3 values. The deposition rate was found to have a dependence on ΔTemp, which was considered as a rough approximation for atmospheric stability. The partitioning of reactive nitrogen was determined from the formation of nitric acid and the deposition of pernitric acid. For the ANTCI 2003 campaign the reactive nitrogen partitioning was found to be 60% HNO_3 and 40% HO_2NO_2.

This partitioning of reactive nitrogen species is expected to occur at all polar sites. However, the South Pole is exceptional among high latitude measurement sites in the level of NO_x observed. Most others, such as Summit, have had NO_x mixing ratios an

order of magnitude lower than observed at the South Pole (see Tables 1.1, 1.2, 1.3). Therefore we have calculated reactive nitrogen concentrations for both Summit field campaigns. In summer at Summit the partitioning was split fairly evenly between HNO_3 and HO_2NO_2, while in the spring the majority (~90%) of reactive nitrogen was in the form of nitric acid. This may be of interest to the ice coring community who have noted a seasonal dependence on the nitrate ion (NO_3^-) found at Summit [*Hastings et al.*,2004].

6.2 Further research

Results from the summer 2003 field campaign suggest that there exists an unaccounted for mechanism that is enhancing hydroxyl concentrations. In situ measurements of reactive halogen species such as BrO and IO might help resolve the discrepancy between model predictions and observations. Measurements of oxygenated hydrocarbons have been obtained from grab samples, but are very limited and have not been published. Measurements of small aldehydes and ketones with the requisite time resolution and sensitivity could also prove to be beneficial.

Measurements of pernitric acid at Summit are also recommended. In particular flux measurements to determine the deposition rate would be quite useful. HO_2NO_2 flux measurements also would be helpful if conducted at the South Pole. A comparison between the soluble nitrite (HONO) measurement and the CIMS pernitric measurement may help to resolve lingering measurement issues. This was performed briefly during ISCAT 2000, but a much longer comparison period is warranted.

6.3 References

Chen, G., D. Davis, J. Crawford, L. M. Hutterli, L. G. Huey, D. Slusher, L. Mauldin, F. Eisele, D. Tanner, J. Dibb, M. Buhr, J. McConnell, B. Lefer, R. Shetter, D. Blake, C. H. Song, K. Lombardi, and J. Arnoldy (2004), A reassessment of HO_x South Pole chemistry based on observations recorded during ISCAT 2000, *Atmospheric Environment*, *38*, 5451-5461.

Domine, F., and P. B. Shepson (2002), Air-snow interactions and atmospheric chemistry, *Science*, *297*, 1506-1510.

Gierczak, T., E. Jimenez, V. Riffault, J. B. Burkholder, and A. R. Ravishankara (2005), Thermal decomposition of HO_2NO_2 (peroxynitric acid, PNA): Rate coefficient and determination of the enthalpy of formation, *Journal of Physical Chemistry A*, *109*, 586-596.

Huey, L. G., D. J. Tanner, D. L. Slusher, J. E. Dibb, R. Arimoto, G. Chen, D. Davis, M. P. Buhr, J. B. Nowak, R. L. Mauldin, F. L. Eisele, and E. Kosciuch (2004), CIMS measurements of HNO_3 and SO_2 at the South Pole during ISCAT 2000, *Atmospheric Environment*, *38*, 5411-5421.

Slusher, D. L., L. G. Huey, D. J. Tanner, G. Chen, D. D. Davis, M. Buhr, J. B. Nowak, F. L. Eisele, E. Kosciuch, R. L. Mauldin, B. L. Lefer, R. E. Shetter, and J. E. Dibb (2002), Measurements of pernitric acid at the South Pole during ISCAT 2000, *Geophysical Research Letters*, *29*, -.

APPENDIX A

REACTION MECHANISM AND IGOR CODE FOR STEADY STATE CALCULATIONS

Concentrations for OH, HO_2, CH_3O_2, HO_2NO_2, CH_3OOH, CH_3OONO_2, CH_3OH, and occasionally HONO were calculated using the steady state assumption. The model was constrained to measured values of temperature, pressure, dew point, CH_4, CO, O_3, NO, H_2O_2, CH_2O, *j*-values, and at times HONO. The model uses an initial guess for the concentrations for each predicted of the species and then iteratively solves for new concentrations until all the species are in steady state.

A.1 Inputs

Number densities for each measured species were calculated from temperature and pressure.

$$M = \frac{p}{RT} = \left(\frac{6.02e^{23} \frac{molecules}{mole}}{1000 \frac{cm^3}{L}} \right) \left(\frac{\left(\frac{pressue(mb)}{1013mb} \right)}{0.08206 \frac{Latm}{moleK} TempK} \right)$$

Water vapor (mb) was calculated from the dew point. The empirical fit was determined from the saturation vapor pressure over ice.

$$vapor(mb) = 6.11e10^{\frac{9.716(Dewpoint)}{(271.5+Dewpoint)}}$$

A.2 Rate Constants

A.2.1 Bimolecular Reactions

The rate constants were obtained from the Jet Propulsion Laboratory Evaluation of Chemical Kinetics and Photochemical Data for Use in Atmospheric Studies [*Sander et al.,* 2006]. Rate constants for each reaction were calculated as a function of the relevant observed parameters. Temperature dependent bimolecular reactions are listed in Table A.1. Bimolecular rate constants are presented in the Arrhenius form.

$$k(T) = A\exp\left(\frac{(-E/R)}{Temp}\right)$$

Table A.1 Bimolecular Reactions

Reaction	Rate Constant
$O(^1D) + O_2 \rightarrow O(^3P) + O_2$	k = 3.3e-11*exp(55/Temp)
$O(^1D) + N_2 \rightarrow O(^3P) + N_2$	k = 2.1e-11*exp(115/Temp)
$O(^1D) + H_2O \rightarrow 2OH$	k = 1.63e-10*exp(60/Temp)
$OH + CH_4 + O_2 \rightarrow CH_3O_2 + H_2O$	k = 2.45e-12*exp(-1775/Temp)
$CH_3O_2 + NO + O_2 \rightarrow HO_2 + NO_2 + CH_2O$	k = 2.8e-12*exp(300/Temp)
$CH_3O_2 + HO_2 \rightarrow CH_3OOH + O_2$	k = 4.1e-13*exp(750/Temp)
$HO_2 + NO \rightarrow OH + NO_2$	k = 3.5e-12*exp(250/Temp)
$OH + HO_2 \rightarrow H_2O + O_2$	k = 4.8e-11*exp(250/Temp)
$HO_2 + O_3 \rightarrow OH + 2O_2$	k = 1.0e-14*exp(-490/Temp)
$OH + O_3 \rightarrow HO_2 + O_2$	k = 1.7e-12*exp(-940/Temp)
$OH + HONO \rightarrow NO_2 + H_2O$	k = 1.8e-11*exp(-390/Temp)
$OH + H_2O_2 \rightarrow HO_2 + H_2O$	k = 1.8e-12*exp(0/Temp)
$OH + CH_2O + O_2 \rightarrow HO_2 + CO + H_2O$	k = 9.0e-12*exp(0/Temp)
$HO_2NO_2 + M \rightarrow HO_2 + NO_2 + M$	$k = 4.1e^{-5} cm^3$ molecules^{-1} s^{-1}
$OH + HO_2NO_2 \rightarrow NO_2 + H_2O + O_2$	k = 1.3e-12*exp(380/Temp)
$OH + CH_3OOH \rightarrow CH_3O_2 + H_2O$	k = 0.7* 3.8e-12*exp(200/Temp)
$OH + CH_3OOH \rightarrow OH + CH_2O + H_2O$	k = 0.3* 3.8e-12*exp(200/Temp)
$CH_3OONO_2 + M \rightarrow CH_3O_2 + NO_2 + M$	$k = 1.6e^{-3} cm^3$ molecules^{-1} s^{-1}
$OH + CH_3OH + O_2 \rightarrow HO_2 + CH_2O + H_2O$	k = 7.3e-12*exp(-620/Temp)

The self reaction of methyl peroxy radicals was also bimolecular but there exists a temperature dependent branching ratio for the products.

$$CH_3O_2 + CH_3O_2 \rightarrow CH_3OH + CH_2O + O_2$$

$$CH_3O_2 + CH_3O_2 + 2O_2 \rightarrow 2HO_2 + 2CH_2O + O_2$$

The bimolecular rate was k_b = 9.5e-14*exp(390/Temp) and the product branching ratio k_{br} = 26.2*exp(-1100/Temp). The reaction that led to formation of methanol and formaldehyde was calculated from $k_b/(1+k_{br})$ and the reaction that formed formaldehyde and HO_2 was calculated from $k_b(k_{br})$.

A.2.2 Termolecular (Association) Reactions

Pressure and temperature dependent termolecular reactions are listed in Table A.2. Rate constants for association reactions have been determined for low and high pressure limits.

$$L.P.Limit = k_0(T) = k_0\left(\frac{Temp}{300}\right)^{-n}$$

$$H.P.Limit = k_\infty(T) = k_\infty\left(\frac{Temp}{300}\right)^{-m}$$

Table A.2 Termolecular Rate Constants

Reaction	Low Pressure Limit	High Pressure Limit
$OH + NO + M \rightarrow HONO + M$	7.0e-31*(temp/300)^-2.6	3.6e-11*(temp/300)^-0.1
$OH + NO_2 + M \rightarrow HNO_3 + M$	2.0e-30*(temp/300)^-3.0	2.5e-11*(temp/300)^-0
$HO_2 + NO_2 + M \rightarrow HO_2NO_2 + M$	2.0e-31*(temp/300)^-3.4	2.9e-12*(temp/300)^-1.1
$CH_3O_2 + NO_2 + M \rightarrow CH_3OONO_2 + M$	1.5e-30*(temp/300)^-4.0	6.5e-12*(temp/300)^-2.0

To obtain the effective second-order rate constant for an association reaction the following equation was used [*Sander et al.*, 2006].

$$k_f([M],T) = \left(\frac{k_0(T)[M]}{1 + \frac{k_0(T)[M]}{k_\infty(T)}} \right) 0.6^{\left(1 + \left(\log_{10}\left(\frac{k_0(T)[M]}{k_\infty(T)} \right) \right)^2 \right)^{-1}}$$

A.2.3 Other reaction rates

The self reactions of HO_2 and OH were dependent on bimolecular and association rate constants.

$$OH + OH + M \rightarrow H_2O_2 + M$$

The bimolecular rate constant was k_b = 4.2e-12*exp(-240/temp) and the low and high pressure limits for the association reaction were k_0 = 6.9e-31*(temp/300)^-1.0 and k_∞ = 2.6e-11*(temp/300)^-0 respectively.

$$HO_2 + HO_2 + M \rightarrow H_2O_2 + O_2 + M$$

The bimolecular rate was k_b = 2.3e-13*exp(600/Temp) the association rate was k_t = 1.7e-33*[M]*exp(1000/Temp). There was only one association rate (low pressure limit) and it was dependent on the concentration of water f_w = 1+1.4e21*[H_2O]*exp(2200/Temp).

The reaction of hydroxyl radical with carbon monoxide has two intermediates.

$$OH + CO \rightarrow HOCO$$

$$OH + CO \rightarrow H + CO_2$$

Although the products were ultimately the same the pathways of chemical activation were dependent on temperature and pressure. The low and high pressure limits for the HOCO intermediate were k_0 = 5.9e-33*(temp/300)^-1.4 and k_∞ = 1.1e-12*(temp/300)^1.3 respectively. The corresponding low and high pressure limits for the

H radical and CO_2 were k_0 = 1.5e-13*(temp/300)^0.6 and k_∞ = 2.1e9*(temp/300)^6.1. The effective second-order reaction rate for chemical activation is provided below.

$$k_f^{ca}([M],T) = \left(\frac{k_0(T)}{1 + \frac{k_0(T)}{k_\infty(T)/[M]}} \right) 0.6^{\left(1 + \left(\log_{10}\left(\frac{k_0(T)}{k_\infty(T)/[M]} \right) \right)^2 \right)^{-1}}$$

The oxidation of nitric acid also has temperature and pressure dependence.

$$OH + HNO_3 \rightarrow H_2O + NO_3$$

This reaction been divided into a low (k_0 = 7.2e-15*exp(785/temp)) and high (k_2 = 4.1e-16*exp(1440/temp)) pressure limit along with a termolecular limit (k_3 = 1.9e-33*exp(725/temp)). The rate constant for incorporating all three limits is provided below.

$$k([M],T) = k_0 + \frac{k_3[M]}{1 + \frac{k_3[M]}{k_2}}$$

Equilibrium constants were also employed to calculate the thermal decomposition rates for CH_3OONO_2 and HO_2NO_2

Table A.3 Equilibrium Constants

Reaction	Rate Constant
$CH_3O_2 + NO_2 \leftrightarrow CH_3OONO_2$	k =1.3e-28*exp(11200/Temp)
$HO_2 + NO_2 \leftrightarrow HO_2NO_2$	k =2.1e-27*exp(10900/Temp)
$HO_2 + NO_2 \leftrightarrow HO_2NO_2$ (Gierczak et al, 2005)	k = temp*1.363e-22*exp((24/(1.987e-3*temp))-20.634)

The thermal decomposition rates were obtained by dividing the forward reaction rate by the equilibrium constants.

A.3 IGOR Code

```
#pragma rtGlobals=1          // Use modern global access method.

Macro PredictOH()
KillWaves/A/Z

//Concentrations
DetermineKelvin()
DetermineDDPerNitric()
DetermineH2Ovapor()
DetermineNumDen()
DetermineNumDenH2O()
DetermineNumDenN2()
DetermineNumDenO2()
DetermineNumDenO3()
DetermineNumDenNO()
NumDenHONO()
NumDenCH4()
NumDenCO()
NumDenCH2O()
NumDenH2O2()
NumDenHNO3()

//rates
 RateConstantkk1()
 RateConstantkk2()
 RateConstantkk3()
 RateConstantkk4()
 RateConstantkk5()
 RateConstantkk6()
 RateConstantkk7()
 RateConstantkk8()
 RateConstantkk9()
 RateConstantkk10()
 RateConstantkk11()
 RateConstantkk12()
 RateConstantkk13()
 RateConstantkk14()
 RateConstantkk15()
 RateConstantkk16()
 RateConstantkk17()
 RateConstantkkt18()
```

```
 RateConstantkk19()
 RateConstantkk20()
 RateConstantkk21()
 RateConstantkk22()
 RateConstantkk23()
 RateConstantkk24()
 RateConstantkk25()
 RateConstantkk26()
 RateConstantkk27()
 RateConstantkk28()
 RateConstantkk29()
 RateConstantkk30()

 //Fraction of O(1D)+H2O
 DetermineFractionO_H2O()
 //Predict HOx
 PredictHOx()
 //Tables
 //Check_water_vapor()
 HOx_Table()
 OH_Table()
 HO2_Table()
 CH3O2_Table()
 NO2_Table()
 HNO4_Table()
 CH3OOH_Table()
 CH3OH_CH3OONO20()
  HONO_Table()
 //Predict_Table()
 //Predicted_Values()
// Converge_Table()
 //Converge_Graph()
 Radicals_vs_NO()
endMacro

//Determine Temp in Kelvin
Function DetermineKelvin()
        wave temp1
        Duplicate/o temp1 temp
        temp +=273.15
end

//Determine Dry Depostion Rate for (Per)Nitric
Function DetermineDDPerNitric()
        wave temp1
        Duplicate/o temp1 DDPN
```

```
	DDPN = 9.26e-5
end

//Determine the amount of water vapor as a function of Dew Point
Function DetermineH2Ovapor()
	wave Dewpt
duplicate/o Dewpt vap
	 if (DewPt >= 0)
		vap = 6.11*10^(7.567*DewPt/(239.7+DewPt))

	else
		vap= 6.11*10^(9.716*DewPt/(271.5+DewPt))

	endif
end

//Determine Number Density as a function of Pressure
Function DetermineNumDen()
	wave temp, pressure
	Duplicate/o temp1 M
	M = ((Pressure/1013)*6.02e23)/(0.08206*Temp*1000)
end

//Determine Number Density of H2O
Function DetermineNumDenH2O()
	wave vap, M, Pressure
	duplicate/o vap H2Oc
	H2Oc = (vap/Pressure)*M
end

//Determine Number Density of Nitrogen
Function DetermineNumDenN2()
	wave M
	duplicate/o M N2c
	N2c = 0.78*M
end

//Determine Number Density of Oxygen
Function DetermineNumDenO2()
	wave  M
	duplicate/o M O2c
	O2c = 0.21*M
end

//Determine Number Density of Ozone
Function DetermineNumDenO3()
```

```
	wave O3, M
	duplicate/o O3 O3c
	O3c = (O3*1e-9)*M
end

	//Determine Number Density of NO
Function DetermineNumDenNO()
	wave NO, M
	duplicate/o NO NOc
	NOc = (NO*1e-12)*M
end

	//Determine Number Density of HONO
Function NumDenHONO()
	wave HONO, M
	duplicate/o HONO HONOc
	HONOc = (HONO*1e-12)*M
end

	//Determine Number Density of Methane
Function NumDenCH4()
	wave CH4, M
	duplicate/o CH4 CH4c
	CH4c = (CH4*1e-6)*M
end

	//Determine Number Density of CO
Function NumDenCO()
	wave CO, M
	duplicate/o CO COc
	COc = (CO*1e-9)*M
end

	//Determine Number Density of HNO3
Function NumDenHNO3()
	wave HNO3, M
	duplicate/o HNO3 HNO3c
	HNO3c = (HNO3*1e-12)*M
end

	//Determine Number Density of CH2O
Function NumDenCH2O()
	wave CH2O, M
	duplicate/o CH2O CH2Oc
	CH2Oc = (CH2O*1e-9)*M
end
```

```
	//Determine Number Density of H2O2
Function NumDenH2O2()
	wave H2O2, M
	duplicate/o H2O2 H2O2c
	H2O2c = (H2O2*1e-9)*M
end

	//Determine rate constant O(D) + O2
Function RateConstantkk1()
	wave temp
	duplicate/o temp kk1
	kk1 = 3.3e-11*exp(55/Temp)
end

	//Determine rate constant O(D) + N2
Function RateConstantkk2()
	wave temp
	duplicate/o temp kk2
	kk2 = 2.1e-11*exp(115/Temp)
end

	//Determine rate constant O(D) + H2O
Function RateConstantkk3()
	wave Temp
	duplicate/o temp kk3
	kk3 = 1.63e-10*exp(60/Temp)
end

	//Determine rate constant OH + CO
Function RateConstantkk4()
	wave temp, M
	Duplicate/o  temp kHOCOhigh kHOCOlow kHCO2high kHCO2low kk4

	kHOCOlow = 5.9e-33*(temp/300)^-1.4
	kHOCOhigh  = 1.1e-12*(temp/300)^1.3
	kHCO2low = 1.5e-13*(temp/300)^0.6
	kHCO2high  = 2.1e9*(temp/300)^6.1
	kk4
=((kHOCOlow*M/(1+kHOCOlow*M/kHOCOhigh))*0.6^(1+(log(kHOCOlow*M/kHO
COhigh))^2)^-
1)+((kHCO2low/(1+kHCO2low/(kHCO2high/M)))*0.6^(1+(log(kHCO2low/(kHCO2hig
h/M)))^2)^-1)
end

	//Determine rate constant OH + CH4
```

```
Function RateConstantkk5()
	wave temp
	duplicate/o temp kk5
	kk5 = 2.45e-12*exp(-1775/Temp)
end

	//Determine rate constant CH3O2 + NO
Function RateConstantkk6()
	wave temp
	duplicate/o temp kk6
	kk6 = 2.8e-12*exp(300/Temp)
end


	//Determine rate constant CH3O2 + HO2
Function RateConstantkk7()
	wave temp
	duplicate/o temp kk7
	kk7 = 4.1e-13*exp(750/Temp)
end

	//Determine rate constant HO2 + NO
Function RateConstantkk8()
	wave temp
	duplicate/o temp kk8
	kk8 = 3.5e-12*exp(250/Temp)
end

	//Determine rate constant OH + HO2
Function RateConstantkk9()
	wave temp
	duplicate/o temp kk9
	kk9 = 4.8e-11*exp(250/Temp)
end

	//Determine rate constant HO2 + HO2
Function RateConstantkk10()
	wave temp, M,H2Oc
	duplicate/o temp kk10 fw
	fw = (1+1.4e-21*H2Oc*exp(2200/Temp))
	kk10 =(( 2.3e-13*exp(600/Temp))+(1.7e-33*M*exp(1000/Temp)))*fw
end

	//Determine rate constant NO + O3
Function RateConstantkk11()
	wave temp
```

```
	duplicate/o temp kk11
	kk11 = 3.0e-12*exp(-1500/Temp)
end
	// Determine rate constant OH + NO
Function RateConstantkk12()
	wave temp, M
	Duplicate/o  temp khonohigh khonolow kk12

	khonolow = 7.0e-31*(temp/300)^-2.6
	khonohigh  = 3.6e-11*(temp/300)^-0.1
	kk12 =
(khonolow*M/(1+khonolow*M/khonohigh))*0.6^(1+(log(khonolow*M/khonohigh))^2)^
-1
end

	//Determine rate constant HO2 + O3
Function RateConstantkk13()
	wave temp
	duplicate/o temp kk13
	kk13 = 1.0e-14*exp(-490/Temp)
end

	//Determine rate constant OH + O3
Function RateConstantkk14()
	wave temp
	duplicate/o temp kk14
	kk14 = 1.7e-12*exp(-940/Temp)
end

	//Determine rate constant OH + HONO
Function RateConstantkk15()
	wave temp
	duplicate/o temp kk15
	kk15 = 1.8e-11*exp(-390/Temp)
end

	//Determine rate constant OH + NO2
Function RateConstantkk16()
	wave temp, M
	Duplicate/o  temp khno3high khno3low kk16

	khno3low = 2.0e-30*(temp/300)^-3.0
	khno3high  = 2.5e-11*(temp/300)^-0
	kk16 =
(khno3low*M/(1+khno3low*M/khno3high))*0.6^(1+(log(khno3low*M/khno3high))^2)^
-1
```

```
end

	//Determine rate constant OH +HNO3
Function RateConstantkk17()
	wave temp, M
	Duplicate/o  temp1 kNO30 kNO32 kNO33 kk17

	kNO30 = 7.2e-15*exp(785/temp)
	kNO32  = 4.1e-16*exp(1440/temp)
	kNO33 = 1.9e-33*exp(725/temp)
	kk17 = kNO30+(kNO33*M/(1+(kNO33*M/kNO32)))
end

	//Determine rate constant OH + OH
Function RateConstantkkt18()
	wave temp, M
	Duplicate/o  temp kh2o2high kh2o2low kk18
	kh2o2low = 6.9e-31*(temp/300)^-1.0
	kh2o2high  = 2.6e-11*(temp/300)^-0
	kk18
=((kh2o2low*M/(1+kh2o2low*M/kh2o2high))*0.6^(1+(log(kh2o2low*M/kh2o2high))^
2)^-1)+4.2e-12*exp(-240/temp)
end

	//Determine rate constant OH + H2O2
Function RateConstantkk19()
	wave temp
	duplicate/o temp kk19
	kk19 = 1.8e-12*exp(0/Temp)
end

	//Determine rate constant OH + CH2O
Function RateConstantkk20()
	wave temp
	duplicate/o temp kk20
	kk20 = 9.0e-12*exp(0/Temp)
end

	//Determine Rate constant HO2 + NO2
Function RateConstantkk21()
	wave temp, M
	Duplicate/o  temp khno4high khno4low kk21
	khno4low = 2.0e-31*(temp/300)^-3.4
	khno4high  = 2.9e-12*(temp/300)^-1.1
```

```
        kk21 =
(khno4low*M/(1+khno4low*M/khno4high))*0.6^(1+(log(khno4low*M/khno4high))^2)^
-1
end

        //Thermal Decomposition of HNO4
Function RateConstantkk22()
        wave temp, kk21
        Duplicate/o  temp  kHNO4eq kk22
        kHNO4eq = temp*1.363e-22*exp((24/(1.987e-3*temp))-20.634)
        kk22 = kk21/KHNO4eq
end

        //Determine rate constant OH + HNO4
Function RateConstantkk23()
        wave temp
        duplicate/o temp kk23
        kk23 = 1.3e-12*exp(380/Temp)
end

        //Determine rate constant CH3O2 + CH3O2 => CH3OH+CH2O+O2
Function RateConstantkk24()
        wave temp
        duplicate/o temp kk24 fr1
        fr1 = 26.2*exp(-1100/Temp)
        kk24 = 9.5e-14*exp(390/Temp)/(1+fr1)
end

//Determine rate constant CH3O2 + CH3O2 =>  2CH2O+2HO2+O2
Function RateConstantkk25()
        wave temp, kk24
        duplicate/o temp kk25 fr1
        fr1 = 26.2*exp(-1100/Temp)
        kk25 = fr1*kk24
end

        //Determine rate constant OH+CH3OOH =>  CH3O2+H2O
Function RateConstantkk26()
        wave temp
        duplicate/o temp kk26
        kk26 =0.7* 3.8e-12*exp(200/Temp)
end

        //Determine rate constant OH+CH3OOH =>  CH2O+OH+H2O
Function RateConstantkk27()
        wave temp
```

```
	duplicate/o temp kk27
	kk27 =0.3* 3.8e-12*exp(200/Temp)
end

	//Determine Rate constant CH3O2+ NO2
Function RateConstantkk28()
	wave temp, M
	Duplicate/o  temp kch3no4high kch3no4low kk28
	kch3no4low = 1.5e-30*(temp/300)^-4.0
	kch3no4high  = 6.5e-12*(temp/300)^-2.0
	kk28 =
(kch3no4low*M/(1+kch3no4low*M/kch3no4high))*0.6^(1+(log(kch3no4low*M/kch3no
4high))^2)^-1
end

	//Thermal Decomposition of CH3OONO2
Function RateConstantkk29()
	wave temp, kk28
	Duplicate/o  temp  kCH3NO4eq kk29
	kCH3NO4eq = 1.3e-28*exp(11200/temp)
	kk29 = kk28/KCH3NO4eq
end

	//Determine rate constant OH+CH3OH
Function RateConstantkk30()
	wave temp
	duplicate/o temp kk30
	kk30 = 7.3e-12*exp(-620/Temp)
end


	// Fraction of O(D) reacting with H2O
Function DetermineFractionO_H2O()
	wave vap,kk1,kk2,kk3,H2Oc,N2c,O2c
	duplicate/o vap Fract
	Fract = (kk3*H2Oc)/(kk1*O2c+kk2*N2c+kk3*H2Oc)
end

Function PredictHOx()
	wave
DDPN,kk1,kk2,kk3,kk4,kk5,kk6,kk7,kk8,kk9,kk10,kk11,kk12,kk13,kk14,kk15,kk16,kk1
7,kk18,kk19,kk20,kk21,kk22,kk23,kk24,kk25,kk26,kk27,kk28,kk29,kk30,Fract,NOc,O3
c,CH4c,COc,HNO3c,H2O2c, CH2Oc, J_O3 ,J_NO2 , J_HNO2, J_H2O2, J_CH2O,
J_HNO3,J_HNO4, J_CH3OOH,M

	variable i,j
```

```
i = 0


Make/N=1000/D/O/R OHsource OHsink HO2source HO2sink NO2source
NO2sink OHint HO2int CH3O2int NO2int HNO4int CH3OOHint CH3OONO2int
CH3OHint HONOint
OHint=Nan
HO2int=Nan
CH3O2int=Nan
NO2int=Nan
HNO4int=Nan
CH3OONO2int=Nan
CH3OHint=Nan
HONOint=Nan


duplicate/o kk1 OHpred  HO2pred CH3O2pred NO2pred HNO4pred
CH3OOHpred CH3OONO2pred CH3OHpred HONOpred
duplicate/o kk1 Total_Source_OH jO3_Source NO_source_OH jHONO_Source
O3_source_OH  jH2O2_source jHNO3_source J_CH3OOH_source
CH3OOH_source_OH
duplicate/o kk1 Total_loss_OH CO_loss_OH CH4_loss_OH HO2_loss_OH
O3_loss_OH H2O2_loss_OH CH2O_loss_OH NO_loss_OH HONO_loss_OH
NO2_loss_OH HNO3_loss_OH OH_loss_OH HNO4_loss_OH CH3OOH_loss_OH
CH3OH_loss_OH
duplicate/o kk1 Total_Source_HO2 CO_source_HO2 JCH2O_source
CH3O2_Source_HO2 O3_source_HO2 CH2O_source_HO2 H2O2_source_HO2
HNO4_source_HO2 JHNO4_source CH3O2_sq_source CH3OH_source_HO2
duplicate/o kk1 Total_loss_HO2 CH3O2_loss_HO2 NO_loss_HO2
OH_loss_HO2 HO2_loss_HO2 O3_loss_HO2 NO2_loss_HO2
duplicate/o kk1 Total_source_CH3O2 CH4_source_CH3O2
CH3OOH_source_CH3O2 CH3OONO2_source_CH3O2 Total_loss_CH3O2
NO_loss_CH3O2 HO2_loss_CH3O2 CH3O2_loss_CH3O2 NO2_loss_CH3O2
duplicate/o kk1 Total_source_NO2 CH3O2_source_NO2 HO2_source_NO2
O3_source_NO2 HONO_source_NO2  JHNO3_source_NO2 HNO3_source_NO2
HNO4_source_NO2 JHNO4_source_NO2 OH_source_NO2 CH3OONO2_source_NO2
duplicate/o kk1 Total_loss_NO2 JNO2_loss OH_loss_NO2
CH3OONO2_loss_NO2 NO_O3_prod
duplicate/o kk1 Total_source_CH3OOH Snow_source_CH3OOH
OH_loss_CH3OOH J_CH3OOH_loss Total_loss_CH3OOH
duplicate/o kk1 Total_source_CH3OONO2 Total_loss_CH3OONO2
Total_source_CH3OH Total_loss_CH3OH
duplicate/o kk1 Total_source_HONO Total_loss_HONO JHONO_loss
OH_loss_HONO
duplicate/o kk1 Total_Source_HOx HONO_source_HOx H2O2_source_HOx
HNO3_source_HOx CH2O_source_HOx HNO4_source_HOx
```

```
	duplicate/o kk1 Total_loss_HOx HO2_OH_loss_HOx HO2_HO2_loss_HOx
OH_OH_loss_HOx CH4_loss_HOx CH3O2_source_HOx CH3O2_loss_HOx
CH3OOH_source_HOx CH3OOH_loss_HOx Total_CH4_loss_HOx  HNO4_loss_HOx
Net_Source_Sink_HOx HNO3_loss_HOx
	duplicate/o kk1 Rad_Rad_loss_HOx H2O2_loss_HOx HONO_loss_HOx
	duplicate/o kk1 Total_Source_HNO4 HNO4_loss_NO2 Total_loss_HNO4
Decomp_HNO4 JHNO4_loss Dry_Dep_HNO4 OH_loss_HNO4 O3_diff
	do



		j=0
			do
			OHint[0] = 1e6
			HO2int[0] = 1e8
			CH3O2int[0] = 1e7
			NO2int[0] = 0 //1e8
			HNO4int[0] = 1e8
			CH3OOHint[0] = 1e9
			CH3OONO2int[0] = 1e6
			CH3OHint[0]= 1e7
			HONOint[0] = 1e6

			OHsource[j] =
(2*J_O3[i]*O3c[i]*Fract[i]+kk8[i]*HO2int[j]*NOc[i]+J_HNO2[i]*HONOint[j]+2*J_H2
O2[i]*H2O2c[i]+J_HNO3[i]*HNO3c[i]+
kk13[i]*O3c[i]*HO2int[j]+J_CH3OOH[i]*CH3OOHint[j])
			OHsink[j] =
(kk4[i]*COc[i]+kk5[i]*CH4c[i]+kk9[i]*HO2int[j]+kk12[i]*NOc[i]+kk14[i]*O3c[i]+kk1
5[i]*HONOint[j]+kk16[i]*NO2int[j]+kk17[i]*HNO3c[i]+2*kk18[i]*OHint[j]+kk19[i]*
H2O2c[i]+kk20[i]*CH2Oc[i]+kk23[i]*HNO4int[j]+kk26[i]*CH3OOHint[j]+kk30[i]*CH
3OHint[j])
			OHint[j+1] = OHsource[j]/OHsink[j]
			HO2source[j] =
(kk4[i]*OHint[j]*COc[i]+kk6[i]*CH3O2int[j]*NOc[i]+kk14[i]*OHint[j]*O3c[i]+2*J_C
H2O[i]*CH2Oc[i]+kk20[i]*CH2Oc[i]*OHint[j]+
kk19[i]*H2O2c[i]*OHint[j]+kk22[i]*HNO4int[j]+J_HNO4[i]*HNO4int[j]+2*kk25[i]*C
H3O2int[j]*CH3O2int[j]+J_CH3OOH[i]*CH3OOHint[j]+kk30[i]*CH3OHint[j]*OHint[
j])
			HO2sink[j] =
(kk7[i]*CH3O2int[j]+kk8[i]*NOc[i]+kk9[i]*OHint[j]+2*kk10[i]*HO2int[j]+kk13[i]*O3
c[i]+kk21[i]*NO2int[j])
			HO2int[j+1] = HO2source[j]/HO2sink[j]
			CH3O2int[j+1] =
(kk5[i]*OHint[j]*CH4c[i]+kk26[i]*CH3OOHint[j]*OHint[j]+kk29[i]*CH3OONO2int[j]
```

```
)/(kk6[i]*NOc[i]+kk7[i]*HO2int[j]+2*kk24[i]*CH3O2int[j]+2*kk25[i]*CH3O2int[j]+kk
28[i]*NO2int[j])
                        CH3OONO2int[j+1] = (kk28[i]*CH3O2int[j]*NO2int[j])/(kk29[i])
                        CH3OOHint[j+1] =
(kk7[i]*CH3O2int[j]*HO2int[j])/(kk26[i]*OHint[j]+kk27[i]*OHint[j]+J_CH3OOH[i])
                        CH3OHint[j+1] =
(kk24[i]*CH3O2int[j]*CH3O2int[j])/(kk30[i]*OHint[j])
                        NO2source[j] =
(kk6[i]*CH3O2int[j]*NOc[i]+kk8[i]*HO2int[j]*NOc[i]+kk11[i]*NOc[i]*O3c[i]+kk15[i]
*OHint[j]*HONOint[j]+J_HNO3[i]*HNO3c[i]+kk17[i]*OHint[j]*HNO3c[i]+kk22[i]*H
NO4int[j]+kk23[i]*HNO4int[j]*OHint[j]+J_HNO4[i]*HNO4int[j]+kk29[i]*CH3OONO
2int[j])

                        NO2sink[j] =
(J_NO2[i]+kk16[i]*OHint[j]+kk21[i]*HO2int[j]+kk28[i]*CH3O2int[j])
                        NO2int[j+1] = NO2source[j]/NO2sink[j]
                        HNO4int[j+1] =
(kk21[i]*HO2int[j]*NO2int[j])/(kk22[i]+J_HNO4[i]+DDPN[i]+kk23[i]*OHint[j])
                        HONOint[j+1] =
(kk12[i]*OHint[j]*NOc[i])/(J_HNO2[i]+kk15[i]*OHint[j])
                        j+=1

                        while (j<=numpnts(OHint)-1)                    // as long as
expression is true
                OHpred[i]=OHint[j]
                HO2pred[i]=HO2int[j]
                CH3O2pred[i]=CH3O2int[j]
                NO2pred[i]=NO2int[j]
                HNO4pred[i]=HNO4int[j]
                CH3OOHpred[i] = CH3OOHint[j]
                CH3OONO2pred[i] = CH3OONO2int[j]
                CH3OHpred[i] = CH3OHint[j]
                HONOpred[i] = HONOint[j]

                //OH source
                JO3_source[i] = 2*J_O3[i]*O3c[i]*Fract[i]
                NO_source_OH[i] = kk8[i]*HO2pred[i]*NOc[i]
                jHONO_source[i] = J_HNO2[i]*HONOpred[i]
                jH2O2_source[i] = 2*J_H2O2[i]*H2O2c[i]
                jHNO3_source[i] = J_HNO3[i]*HNO3c[i]
                O3_source_OH[i] = kk13[i]*O3c[i]*HO2pred[i]
                J_CH3OOH_source[i] = J_CH3OOH[i]*CH3OOHpred[i]

        Total_Source_OH[i]=JO3_source[i]+NO_source_OH[i]+jHONO_source[i]+jH2
O2_source[i]+jHNO3_source[i]+O3_source_OH[i]+J_CH3OOH_source[i]
                //OH sink
```

```
CO_loss_OH[i]= kk4[i]*COc[i]*OHpred[i]
CH4_loss_OH[i]=kk5[i]*CH4c[i]*OHpred[i]
HO2_loss_OH[i]=kk9[i]*HO2pred[i]*OHpred[i]
NO_loss_OH[i]=kk12[i]*NOc[i]*OHpred[i]
O3_loss_OH[i] = kk14[i]*O3c[i]*OHpred[i]
HONO_loss_OH[i] = kk15[i]*HONOpred[i]*OHpred[i]
NO2_loss_OH[i] = kk16[i]*NO2pred[i]*OHpred[i]
HNO3_loss_OH[i] = kk17[i]*HNO3c[i]*OHpred[i]
OH_loss_OH[i] = 2*kk18[i]*OHpred[i]*OHpred[i]
H2O2_loss_OH[i] = kk19[i]*H2O2c[i]*OHpred[i]
CH2O_loss_OH[i] = kk20[i]*CH2Oc[i]*OHpred[i]
HNO4_loss_OH[i] = kk23[i]*HNO4pred[i]*OHpred[i]
CH3OOH_loss_OH[i] = kk26[i]*CH3OOHpred[i]*OHpred[i]
CH3OH_loss_OH[i] = kk30[i]*CH3OHpred[i]*OHpred[i]

Total_loss_OH[i]=CO_loss_OH[i]+CH4_loss_OH[i]+HO2_loss_OH[i]+NO_loss
_OH[i]+O3_loss_OH[i]+HONO_loss_OH[i]+NO2_loss_OH[i]+HNO3_loss_OH[i]+OH
_loss_OH[i]+H2O2_loss_OH[i]+CH2O_loss_OH[i]+HNO4_loss_OH[i]+CH3OOH_loss
_OH[i]+CH3OH_loss_OH[i]

//HO2 source
CO_source_HO2[i] = kk4[i]*OHpred[i]*COc[i]
CH3O2_Source_HO2[i] = kk6[i]*CH3O2pred[i]*NOc[i]
O3_source_HO2[i] = kk14[i]*OHpred[i]*O3c[i]
JCH2O_source[i] = 2*J_CH2O[i]*CH2Oc[i]
CH2O_source_HO2[i] = kk20[i]*CH2Oc[i]*OHpred[i]
H2O2_source_HO2[i] = kk19[i]*H2O2c[i]*OHpred[i]
HNO4_source_HO2[i] = kk22[i]*HNO4pred[i]
JHNO4_source[i] = J_HNO4[i]*HNO4pred[i]
CH3O2_sq_source[i]= 2*kk25[i]*CH3O2pred[i]*CH3O2pred[i]
J_CH3OOH_source[i] = J_CH3OOH[i]*CH3OOHpred[i]
CH3OH_source_HO2[i] = kk30[i]*CH3OHpred[i]*OHpred[i]
Total_Source_HO2[i] =
CO_source_HO2[i]+CH3O2_Source_HO2[i]+O3_source_HO2[i]+JCH2O_source[i]+C
H2O_source_HO2[i]+H2O2_source_HO2[i]+HNO4_source_HO2[i]+JHNO4_source[i]+
CH3O2_sq_source[i]+J_CH3OOH_source[i]+CH3OH_source_HO2[i]
//HO2 sink
CH3O2_loss_HO2[i] = kk7[i]*CH3O2pred[i]*HO2pred[i]
NO_loss_HO2[i] = kk8[i]*NOc[i]*HO2pred[i]
OH_loss_HO2[i] = kk9[i]*OHpred[i]*HO2pred[i]
HO2_loss_HO2[i] =2*kk10[i]*HO2pred[i]*HO2pred[i]
O3_loss_HO2[i] = kk13[i]*O3c[i]*HO2pred[i]
NO2_loss_HO2[i] = kk21[i]*NO2pred[i]*HO2pred[i]
Total_loss_HO2[i] =
CH3O2_loss_HO2[i]+NO_loss_HO2[i]+OH_loss_HO2[i]+HO2_loss_HO2[i]+O3_loss_
HO2[i]+NO2_loss_HO2[i]
```

```
//CH3O2 source
CH4_source_CH3O2[i] = kk5[i]*OHpred[i]*CH4c[i]
CH3OOH_source_CH3O2[i] = kk26[i]*CH3OOHpred[i]*OHpred[i]
CH3OONO2_source_CH3O2[i] = kk29[i]*CH3OONO2pred[i]

Total_source_CH3O2[i]=CH4_source_CH3O2[i]+CH3OOH_source_CH3O2[i]+
CH3OONO2_source_CH3O2[i]
//CH3O2 sink
NO_loss_CH3O2[i]=kk6[i]*NOc[i]*CH3O2pred[i]
HO2_loss_CH3O2[i]=kk7[i]*HO2pred[i]*CH3O2pred[i]
CH3O2_loss_CH3O2[i]
=2*kk24[i]*CH3O2pred[i]*CH3O2pred[i]+2*kk25[i]*CH3O2pred[i]*CH3O2pred[i]
NO2_loss_CH3O2[i] = kk28[i]*CH3O2pred[i]*NO2pred[i]

Total_loss_CH3O2[i]=NO_loss_CH3O2[i]+HO2_loss_CH3O2[i]+CH3O2_loss_
CH3O2[i]+NO2_loss_CH3O2[i]

//NO2 source
CH3O2_source_NO2[i]=kk6[i]*CH3O2pred[i]*NOc[i]
HO2_source_NO2[i]=kk8[i]*HO2pred[i]*NOc[i]
O3_source_NO2[i]=kk11[i]*NOc[i]*O3c[i]
HONO_source_NO2[i] = kk15[i]*OHpred[i]*HONOpred[i]
JHNO3_source_NO2[i] = J_HNO3[i]*HNO3c[i]
HNO3_source_NO2[i] = kk17[i]*OHpred[i]*HNO3c[i]
HNO4_source_NO2[i] = kk22[i]*HNO4pred[i]
JHNO4_source_NO2[i] = J_HNO4[i]*HNO4pred[i]
OH_source_NO2[i] = kk23[i]*HNO4pred[i]*OHpred[i]
CH3OONO2_source_NO2[i] = kk29[i]*CH3OONO2pred[i]

Total_source_NO2[i]=CH3O2_source_NO2[i]+HO2_source_NO2[i]+O3_source
_NO2[i]+HONO_source_NO2[i]+JHNO3_source_NO2[i]+HNO3_source_NO2[i]+HNO
4_source_NO2[i]+JHNO4_source_NO2[i]+OH_source_NO2[i]+CH3OONO2_source_N
O2[i]
//NO2 sink
JNO2_loss[i]=J_NO2[i]*NO2pred[i]
OH_loss_NO2[i]=kk16[i]*OHpred[i]*NO2pred[i]
HNO4_loss_NO2[i] = kk21[i]*HO2pred[i]*NO2pred[i]
CH3OONO2_loss_NO2[i] = kk28[i]*CH3O2pred[i]*NO2pred[i]

Total_loss_NO2[i]=JNO2_loss[i]+OH_loss_NO2[i]+HNO4_loss_NO2[i]+CH3O
ONO2_loss_NO2[i]

//HNO4 source & sink
Total_Source_HNO4[i] = kk21[i]*HO2pred[i]*NO2pred[i]
Decomp_HNO4[i] = kk22[i]*HNO4pred[i]
```

```
JHNO4_loss[i] = J_HNO4[i]*HNO4pred[i]
Dry_Dep_HNO4[i] = DDPN[i]*HNO4pred[i]
OH_loss_HNO4[i] = kk23[i]*HNO4pred[i]*OHpred[i]
Total_loss_HNO4[i] =
Decomp_HNO4[i]+JHNO4_loss[i]+Dry_Dep_HNO4[i]+OH_loss_HNO4[i]

//HONO source & sink
Total_Source_HONO[i] = kk12[i]*OHpred[i]*NOc[i]
Total_loss_HONO[i] =
J_HNO2[i]*HONOpred[i]+kk15[i]*OHpred[i]*HONOpred[i]
JHONO_loss[i] = J_HNO2[i]*HONOpred[i]
OH_loss_HONO[i] = kk15[i]*OHpred[i]*HONOpred[i]

//CH3OOH source & sink
Total_source_CH3OOH[i] = kk7[i]*CH3O2pred[i]*HO2pred[i]
OH_loss_CH3OOH[i] =
kk26[i]*CH3OOHpred[i]*OHpred[i]+kk27[i]*CH3OOHpred[i]*OHpred[i]
J_CH3OOH_loss[i] = J_CH3OOH[i]*CH3OOHpred[i]
Total_loss_CH3OOH[i] = OH_loss_CH3OOH[i]+J_CH3OOH_loss[i]

//CH3OONO2 source & sink
Total_source_CH3OONO2[i] = kk28[i]*CH3O2pred[i]*NO2pred[i]
Total_loss_CH3OONO2[i] = kk29[i]*CH3OONO2pred[i]

//CH3OH source & sink
Total_source_CH3OH[i] = kk24*CH3O2pred[i]*CH3O2pred[i]
Total_loss_CH3OH[i] = kk30[i]*CH3OHpred[i]*OHpred[i]

//HOx Production
H2O2_source_HOx[i] = jH2O2_source[i]
CH2O_source_HOx[i] = JCH2O_source[i]
HNO3_source_HOx[i] = jHNO3_source[i]
Total_Source_HOx[i] =
JO3_source[i]+H2O2_source_HOx[i]+CH2O_source_HOx[i]+HNO3_source_HOx[i]

//HOx Loss
HO2_OH_loss_HOx[i] = 2*kk9[i]*HO2pred[i]*OHpred[i]
HO2_HO2_loss_HOx[i] = 2*kk10[i]*HO2pred[i]*HO2pred[i]
OH_OH_loss_HOx[i] = 2*kk18[i]*OHpred[i]*OHpred[i]
Rad_Rad_loss_HOx[i] = HO2_OH_loss_HOx[i]
H2O2_loss_HOx[i] = HO2_HO2_loss_HOx[i]+OH_OH_loss_HOx[i]
//Methane
CH4_loss_HOx[i] = kk5[i]*CH4c[i]*OHpred[i]
CH3O2_source_HOx[i] =
kk6*CH3O2pred[i]*NOc[i]+2*kk25[i]*CH3O2pred[i]*CH3O2pred[i]
CH3O2_loss_HOx[i] = kk7[i]*HO2pred[i]*CH3O2pred[i]
```

```
		CH3OOH_source_HOx[i] = 2*J_CH3OOH[i]*CH3OOHpred[i]
		CH3OOH_loss_HOx[i] = kk26[i]*CH3OOHpred[i]*OHpred[i]
		Total_CH4_loss_HOx[i] = CH4_loss_HOx[i]-
CH3O2_source_HOx[i]+CH3O2_loss_HOx[i]-
CH3OOH_source_HOx[i]+CH3OOH_loss_HOx[i]

		HNO3_loss_HOx[i] =
kk16[i]*OHpred[i]*NO2pred[i]+kk17[i]*OHpred[i]*HNO3c[i]
		HNO4_loss_HOx[i] = kk21[i]*HO2pred[i]*NO2pred[i]-
(kk22[i]*HNO4pred[i]+J_HNO4[i]*HNO4pred[i])+kk23[i]*HNO4pred[i]*OHpred[i]+D
DPN[i]*HNO4pred[i]
		HONO_loss_HOx[i] =
kk15[i]*HONOpred[i]*OHpred[i]+kk12[i]*OHpred[i]*NOc[i]-jHONO_source[i]

		Total_loss_HOx[i] =
Rad_Rad_loss_HOx[i]+H2O2_loss_HOx[i]+HNO4_loss_HOx[i]+Total_CH4_loss_HOx
[i]+HNO3_loss_HOx[i]+HONO_loss_HOx[i]
		Net_Source_Sink_HOx[i] = Total_Source_HOx[i]-Total_loss_HOx[i]
		O3_diff[i] =
((J_NO2[i]*NO2pred[i])/(J_O3[i]*Fract[i]+kk11[i]*NOc[i]+kk13[i]*HO2pred[i]+kk14[i
]*OHpred[i])*(1e9/M[i]))-(O3c[i]*1e9/M[i])
	i+=1
                                                                    // execute the loop
body
	while (i<=numpnts(kk2)-1)                          // as long as expression is true

end

Window Check_water_vapor() : Table
	PauseUpdate; Silent 1		// building window...
	Edit/W=(5.25,42.5,510,218) Dewpt,Temp,vap,M,kk1,kk2,kk3,Fract,O3c
EndMacro

Window HOx_Table() : Table
	PauseUpdate; Silent 1		// building window...
	Edit/W=(5.4,42.8,740.4,217.4)
Total_Source_HOx,jO3_Source,H2O2_source_HOx,CH2O_source_HOx
	AppendToTable
HNO3_source_HOx,Total_loss_HOx,Rad_Rad_loss_HOx,H2O2_loss_HOx,Total_CH4_
loss_HOx
	AppendToTable
HNO4_loss_HOx,HNO3_loss_HOx,HONO_loss_HOx,Net_Source_Sink_HOx,O3_diff
EndMacro

Window OH_Table() : Table
	PauseUpdate; Silent 1		// building window...
```

```
	Edit/W=(5.25,42.5,861.75,217.25)
OHpred,Total_Source_OH,jO3_Source,NO_source_OH,jHONO_Source,jH2O2_source
	AppendToTable jHNO3_source,O3_source_OH,J_CH3OOH_source,
Total_loss_OH,CH4_loss_OH,CO_loss_OH
	AppendToTable
HO2_loss_OH,NO_loss_OH,O3_loss_OH,HONO_loss_OH,NO2_loss_OH,HNO3_loss_
OH
	AppendToTable
OH_loss_OH,H2O2_loss_OH,CH2O_loss_OH,HNO4_loss_OH,CH3OOH_loss_OH,CH
3OH_loss_OH
EndMacro

Window HO2_Table() : Table
	PauseUpdate; Silent 1		// building window...
	Edit/W=(5.25,42.5,935.25,217.25)
HO2pred,Total_Source_HO2,CO_source_HO2,CH3O2_Source_HO2
	AppendToTable
O3_source_HO2,JCH2O_source,CH2O_source_HO2,H2O2_source_HO2,HNO4_source
_HO2
	AppendToTable
JHNO4_source,CH3O2_sq_source,J_CH3OOH_source,CH3OH_source_HO2,Total_loss
_HO2,CH3O2_loss_HO2,NO_loss_HO2
	AppendToTable OH_loss_HO2,HO2_loss_HO2,O3_loss_HO2,NO2_loss_HO2
EndMacro

Window CH3O2_Table() : Table
	PauseUpdate; Silent 1		// building window...
	Edit/W=(5.25,42.5,590.25,217.25)
CH3O2pred,CH3OONO2_source_CH3O2,Total_source_CH3O2,Total_loss_CH3O2,NO
_loss_CH3O2
	AppendToTable HO2_loss_CH3O2,CH3O2_loss_CH3O2,NO2_loss_CH3O2
EndMacro

Window NO2_Table() : Table
	PauseUpdate; Silent 1		// building window...
	Edit/W=(5.25,42.5,947.25,217.25)
NO2pred,Total_source_NO2,O3_source_NO2,CH3O2_source_NO2
	AppendToTable
HO2_source_NO2,HONO_source_NO2,jHNO3_source,HNO3_source_NO2,HNO4_sou
rce_NO2
	AppendToTable
JHNO4_source_NO2,OH_source_NO2,CH3OONO2_source_NO2,Total_loss_NO2
	AppendToTable
JNO2_loss,OH_loss_NO2,HNO4_loss_NO2,CH3OONO2_loss_NO2
EndMacro
```

```
Window HNO4_Table() : Table
	PauseUpdate; Silent 1		// building window...
	Edit/W=(37.5,91.25,542.25,266)
HNO4pred,Total_Source_HNO4,Total_loss_HNO4,Decomp_HNO4
	AppendToTable JHNO4_loss,Dry_Dep_HNO4,OH_loss_HNO4
EndMacro

Window CH3OOH_Table() : Table
	PauseUpdate; Silent 1		// building window...
	Edit/W=(5.25,42.5,510,218)
Total_source_CH3OOH,Total_loss_CH3OOH,J_CH3OOH_loss,OH_loss_CH3OOH
	ModifyTable width(Total_source_CH3OOH)=102
EndMacro

Window CH3OH_CH3OONO20() : Table
	PauseUpdate; Silent 1		// building window...
	Edit/W=(5.25,42.5,557.25,218)
Total_source_CH3OONO2,Total_loss_CH3OONO2,Total_source_CH3OH
	AppendToTable Total_loss_CH3OH
	ModifyTable
width(Total_source_CH3OONO2)=120,width(Total_loss_CH3OONO2)=113,width(Tota
l_source_CH3OH)=102
	ModifyTable width(Total_loss_CH3OH)=107
EndMacro

Window HONO_Table() : Table
	PauseUpdate; Silent 1		// building window...
	Edit/W=(4.8,42.2,510,202.4)
Total_source_HONO,Total_loss_HONO,JHONO_loss,OH_loss_HONO
	AppendToTable HONOpred
	ModifyTable width(Total_source_HONO)=100
EndMacro

Window Converge_Table() : Table
	PauseUpdate; Silent 1		// building window...
	Edit/W=(5.25,42.5,533.25,218)
HNO4int,NO2int,CH3O2int,HO2int,OHint,CH3OOHint,CH3OONO2int
EndMacro

Window Predict_Table() : Table
	PauseUpdate; Silent 1		// building window...
	Edit/W=(254.25,300.5,759,476)
NO,HO2pred,OHpred,CH3O2pred,CH3OOHpred,NO2pred,HNO4pred
	AppendToTable CH3OONO2pred
EndMacro
```

```
Window Converge_Graph() : Graph
	PauseUpdate; Silent 1		// building window...
	Display /W=(171,324.5,565.5,533) CH3O2int,HNO4int vs testwave
	AppendToGraph HO2int vs testwave
	AppendToGraph NO2int vs testwave
	AppendToGraph OHint vs testwave
	AppendToGraph CH3OOHint vs testwave
	ModifyGraph mode(OHint)=4
	ModifyGraph marker(OHint)=26
	ModifyGraph
lSize(CH3O2int)=2,lSize(HNO4int)=2,lSize(HO2int)=2,lSize(NO2int)=2,lSize(CH3OO
Hint)=2
	ModifyGraph
rgb(CH3O2int)=(65280,0,52224),rgb(HNO4int)=(0,52224,26368),rgb(HO2int)=(0,0,0)
	ModifyGraph
rgb(NO2int)=(16384,16384,65280),rgb(CH3OOHint)=(13056,4352,0)
	SetAxis left 0,10000000000
	SetAxis bottom 1.70226244343891,99.7167420814479
	Legend/N=text0/J/A=MC/X=-15.29/Y=31.00 "\\s(CH3O2int)
CH3O2int\r\\s(HNO4int) HNO4int\r\\s(HO2int) HO2int\r\\s(NO2int) NO2int\r\\s(OHint)
OHint\r\\s(CH3OOHint) CH3OOHint"
EndMacro

Window Predicted_Values() : Graph
	PauseUpdate; Silent 1		// building window...
	Display /W=(5.25,42.5,399.75,251)
CH3OOHpred,HNO4pred,NO2pred,CH3O2pred,HO2pred vs Point
	AppendToGraph OHpred vs Point
	ModifyGraph mode=4
	ModifyGraph
marker(CH3OOHpred)=26,marker(HNO4pred)=26,marker(NO2pred)=29,marker(CH3O
2pred)=26
	ModifyGraph marker(HO2pred)=26,marker(OHpred)=29
	ModifyGraph
rgb(HNO4pred)=(0,0,0),rgb(NO2pred)=(65280,0,52224),rgb(CH3O2pred)=(0,52224,263
68)
	ModifyGraph rgb(HO2pred)=(0,0,65280),rgb(OHpred)=(39168,39168,39168)
	Cursor/P A NO2pred 8;Cursor/P B NO2pred 8
	ShowInfo
EndMacro

Window Radicals_vs_NO() : Graph
	PauseUpdate; Silent 1		// building window...
```

```
	Display /W=(24.75,157.25,419.25,365.75) HO2pred,CH3O2pred,OHpred vs NO
	ModifyGraph mode=3
	ModifyGraph lSize=2
	ModifyGraph rgb(CH3O2pred)=(0,52224,26368),rgb(OHpred)=(0,0,52224)
	ModifyGraph log(left)=1
	SetAxis bottom 0,100
	Legend/N=text0/J/A=MC/X=36.26/Y=-21.74 "\\s(HO2pred)
HO2pred\r\\s(CH3O2pred) CH3O2pred\r\\s(OHpred) OHpred"
EndMacro
```